

NORTHWESTERN UNIVERSITY

**Pulse Propagation in Nonlinear Optical Fibers
using Phase-Sensitive Amplifiers**

A DISSERTATION

SUBMITTED TO THE GRADUATE SCHOOL
IN PARTIAL FULFILLMENT OF THE REQUIREMENTS

for the degree of
DOCTOR OF PHILOSOPHY
Field of Applied Mathematics

By
Jose Nathan Kutz

EVANSTON, ILLINOIS

December 1994

19980115 176

REPORT DOCUMENTATION PAGE

Form Approved
OMB No. 0704-0188

Public reporting burden for this collection of information is estimated to average 1 hour per response, including the time for reviewing instructions, searching existing data sources, gathering and maintaining the data needed, and completing and reviewing the collection of information. Send comments regarding this burden estimate or any other aspect of this collection of information, including suggestions for reducing this burden, to Washington Headquarters Services, Directorate for Information Operations and Reports, 1215 Jefferson Davis Highway, Suite 1204, Arlington, VA 22202-4302, and to the Office of Management and Budget, Paperwork Reduction Project (0704-0188) Washington, DC 20503.

1. AGENCY USE ONLY (Leave Blank)	2. REPORT DATE December 1994	3. REPORT TYPE AND DATES COVERED Final	
4. TITLE AND SUBTITLE Pulse Propagation in Nonlinear Optical Fibers using Phase-Sensitive Amplifiers		5. FUNDING NUMBERS	
6. AUTHORS Jose Nathan Kutz			
7. PERFORMING ORGANIZATION NAME(S) AND ADDRESS(ES) Northwestern University			
8. SPONSORING/MONITORING AGENCY NAME(S) AND ADDRESS(ES) AFOSR/NI 110 Duncan Avenue, Room B-115 Bolling Air Force Base, DC 20332-8080			
11. SUPPLEMENTARY NOTES			
12a. DISTRIBUTION AVAILABILITY STATEMENT Approved for Public Release		12b. DISTRIBUTION CODE	
13. ABSTRACT (Maximum 200 words) See attached.			
14. SUBJECT TERMS		15. NUMBER OF PAGES	
		16. PRICE CODE	
17. SECURITY CLASSIFICATION OF REPORT Unclassified	18. SECURITY CLASSIFICATION OF THIS PAGE Unclassified	19. SECURITY CLASSIFICATION OF ABSTRACT Unclassified	20. LIMITATION OF ABSTRACT UL

0029

AGENCY REPORT NUMBER

DTIC QUALITY IMPROVED 2

©Copyright by Jose Nathan Kutz 1994
All Rights Reserved

For Mom and Dad.

ABSTRACT

Pulse Propagation in Nonlinear Optical Fibers using Phase-Sensitive Amplifiers

Jose Nathan Kutz

A mathematical model for pulse propagation in a nonlinear fiber-optic communications line is presented where linear loss in the fiber is balanced by a chain of periodically-spaced, phase-sensitive amplifiers (PSAs). A multiple scale analysis is employed to average over the strong, rapidly-varying and periodic perturbations to the governing nonlinear Schrödinger equation (NLS). The analysis indicates that the averaged evolution is governed by a fourth-order nonlinear diffusion equation which evolves on a length scale much greater than that of the typical soliton period.

In a particular limit, stable steady-state hyperbolic secant solutions of the averaged equation are analytically found to exist provided a minimum amount of over-amplification is supplied. Further, arbitrary initial conditions within a wide stability region exponentially decay onto the steady-state. Outside of this analytic regime, extensive numerical simulations indicate that soliton-like steady-states exist and act as exponential attractors for a wide region of parameter space. These simulations also show that the averaged evolution is quite accurate in modeling the full NLS with loss and phase-sensitive gain.

The bifurcation structure of the fourth-order equation is explored. A sub-critical bifurcation from the trivial solution is found to occur for a specific overamplification value. Further, a limit point, or fold, is also found which connects the stable branch of solutions with the unstable branch from the subcritical bifurcation. The bifurcation structure can be further explored in parameter space with the use of AUTO which is capable of tracking steady-state solutions for a wide range of parameters.

For larger amplifier spacings, a small dispersive radiation field is generated from the periodic forcing of the loss and gain. The NLS with variably-spaced PSAs is then considered in an effort to reduce the radiation field. Numerical results indicate that the dispersive field is effectively attenuated depending upon the variability and distribution of the amplifiers.

Acknowledgments

In ending my four year stay at Northwestern University, it is appropriate and fitting that I thank those who have contributed to the successful submission of this dissertation. I would like to especially thank my advisor Bill Kath. Bill has been both a friend and a mentor through the happiness and frustration of graduate school. More importantly, Bill has provided me with a model of a person who pursues their work with a passion while maintaining a strong sense of family. I hope one day to follow his example of being both an exceptional professional and family man. I would also like to thank Prem Kumar. Prem has been like a second advisor and an invaluable help in my dissertation work. Moreover, he has helped me develop the background necessary to survive in a difficult academic job market. Thanks also to Andy Bernoff for the helpful suggestions and insights into this dissertation. Collectively, I would like to thank Bill, Prem and Andy for educating me in the issues of clarity and conciseness. I hope the lesson is not lost on me. It is appreciated.

I am also very grateful to the Southern Center for Electrical Engineering Education for sponsoring me through the National Defense Science and Engineering Graduate Fellowship Program. Their contribution was invaluable in the successful completion of this research.

I also extend a thank you to the remaining faculty members of the applied mathematics department. From Bernie Matkowsky's bifurcation theory lectures to Alvin Bayliss's numerical methods, it seems that each in their own way have contributed greatly to my education.

To Judy, Edla and Eleanor – a big hug! Thanks so much for getting me through the administrative Northwestern zoo. Judy, I'll send you postcards of my exotic trips. I don't believe Minnesota counts, but I'll keep you posted.

Now I would like to thank those who have had the most significant effect on my stay at Northwestern. This is a big thanks to my fellow graduate students who endured along side me. Thanks to Burt, Gavin, Ed and Dawn for the rap sessions which seemed so often times necessary for sanity. Thanks also to Tom and Jen for the lunch breaks away from the world of mathematics and a little closer to home. And a special thanks to the air-lock crew of Dan (& Nancy & Allen), Cheryl (& Steve) and Joe. I treasure these friendships and will miss them greatly as I move on. I will particularly miss the talks which had nothing to do with math and everything to do with life. Thanks you three, you made a huge difference. To those whose turn is coming – Anne, Dave, Tim, Mike – you know I'm pulling for you. Can't say I want to stick around however.

And now family and friends. I want to thank Mom and Dad, Dav, Dan, Fred, Judy, Jee Young, Jee Sook and Gary. Thanks for always believing in my dreams. I especially thank Kristy (soon to be a Kutz) for being such a support, strength and joy in my life. Thanks also to Bob and Tonya, Doug and Megan, PYGS, First Presbyterian and Ultimate. Senna – you will be missed greatly.

I thank God for making this dream possible.

Contents

List of Figures	ix	
1	Introduction	1
1.1	Historical Perspective	1
1.2	Recent Issues	4
2	The Phase-Sensitive Amplifier	7
2.1	Introduction	7
2.2	Maxwell's Equations	9
2.3	Degenerate Optical Parametric Amplifier	18
2.4	Jump Conditions	22
2.5	Phase-Mismatch and Bandwidth Considerations in a Fiber PSA . . .	24
2.6	Summary	27
3	Averaged Pulse Propagation using Phase-Sensitive Amplifiers	31
3.1	Introduction	31
3.2	Formulation	34
3.3	Quadrature Decomposition	36
3.4	Multiple-Scale Averaging	37
3.5	Summary	44
4	Existence and Stability of Pulse Solutions	47
4.1	Introduction	47
4.2	Pulse Stability for Small Amplifier Spacing	49
4.2.1	Zero Modes of the Linearized Operator and Their Stability .	52

4.2.2	Spectral Estimates for the Linearized Operator when Excluding the Zero Modes	55
4.3	Pulse Stability for Amplifier Spacing of $O(1)$	62
4.4	Summary	76
5	Bifurcation Analysis	78
5.1	Introduction	78
5.2	Bifurcation from the Trivial Solution	79
5.3	Bifurcation Structure via AUTO	84
5.4	Summary	92
6	Variable Amplifier Spacing	95
6.1	Introduction	95
6.2	Sideband Frequency Generation	97
6.3	Two Distinct Amplifier Spacings	100
6.4	Random Amplifier Spacing	113
6.5	Summary	115
References		120

List of Figures

2.1	Photon description of the interaction of three fields at frequencies ω_1 , ω_2 and ω_3 . In (a) the process of parametric amplification is depicted, i.e., two photons are created at ω_1 and ω_2 with the annihilation of a single photon at ω_3 . In (b) the reverse is shown, the two photons at ω_1 and ω_2 are simultaneously annihilated to create a photon at ω_3 . This is known as sum-frequency generation.	8
2.2	Qualitative behavior of the signal, idler, and pump fields. In (a) and (b) the signal and idler fields are depicted. The initial signal field is a hyperbolic secant while the initial idler field was zero. In (c), the combined signal and idler fields are depicted. This represents the effective ‘signal’ field output of the PSAs. The pump field in (d) is shown to be essentially undepleted with a slight group-velocity drift. .	21
2.3	Contour plots of the pump and signal-idler fields. The pump field in (a) is shown to exhibit a drift in the group velocity. In (b), the signal-idler fields have a much smaller drift since the pump field is assumed to be much wider in duration than the signal field.	22
2.4	In (a) and (b), the effective gain, i.e., $\text{Re}\{g\}$, is plotted as a function of the frequency for $ \alpha z_a = 1$ ($e^{ \alpha z_a} = 2.72$) and $ \alpha z_a = 1.609$ ($e^{ \alpha z_a} = 5.0$) respectively given $k'' = -17, -20$ and $-22 \text{ ps}^2/\text{km}$	28
2.5	Qualitative comparison of the bandwidth of a fiber-PSA ($k'' = -17 \text{ ps}^2/\text{km}$) with a normalized 50 ps (11.4 GHz) pulse. In (a), the pulse spectrum is seen to be extremely narrow in comparison to the PSA bandwidth. In (b), a blown up version depicts the normalized pulse spectrum more clearly.	29

2.6	A physically realizable PSA employing a degenerate optical parametric amplifier for use in an optical communications line	30
3.1	Schematic of a nonlinear optical fiber transmission line in which loss is balanced by a chain of periodically-spaced, phase-sensitive amplifiers (PSAs).	35
3.2	Qualitative behavior of the rapid fluctuations which occur in the phase-locked quadrature A on the ζ length scale. Note the balance between the loss and gain over each successive fiber/amplifier segment.	41
4.1	Plot of the maximum amplitude for the two solution branches $U = A_{\pm} \operatorname{sech} A_{\pm} \tau$ where $A_{\pm} = (1 \pm 2(\Delta\alpha)^{1/2})^{1/2}$. Region 1 is the asymptotic regime explored in the next section while region 2 is an asymptotic regime explored in the next chapter.	48
4.2	Evolution of initial hyperbolic-secant pulses $U(\tau, 0) = \operatorname{sech} \tau$, (a), and $U(\tau, 0) = 1.8 \operatorname{sech} \tau$, (b), showing exponential decay onto the stable pulse solution. The parameters are: $\Gamma l = 1$ (corresponding to an amplifier spacing of 36 km), $\kappa = 1$, and $\Delta\alpha = 0.1$. The computations were run to $\bar{\xi} = 10$ which explicitly shows the stability of the pulses. .	64
4.3	Asymptotic approach onto the final steady-state solution from initial conditions $U(\tau, 0) = A \operatorname{sech} 1.5\tau$, where $A = 1.9, 1.6, 1.3$ and 1.2 respectively. Note that the transient response to the initial amplitude is attenuated after a very short distance of the nondimensional distance $\bar{\xi}$. Further, the steady-state is an attractor for a wide range of initial amplitudes. The parameter values used are identical with those of the previous figure.	65
4.4	Initial pulse amplitudes A and widths T_0 which give stable pulse solutions for $\Gamma l = 1$, $\kappa = 1$, and $\Delta\alpha = 0.1$. The initial conditions $U(T, 0) = A \operatorname{sech}(T/T_0)$, with different values of A and T_0 , were used.	65

4.5	Final steady-state pulse profiles for different values of the overamplification parameter, $\Delta\alpha = 0.05, 0.10$, and 0.20 . Note the small wings in the pulse's profile which develop for the larger values of $\Delta\alpha$.	66
4.6	Comparison of the solutions of the averaged envelope equation and the full nonlinear Schrödinger equation with loss and periodic phase-sensitive amplification, showing the in-phase quadrature, (a), and the difference, (b), between the two solutions. The parameters are $\Gamma l = 1.0$, corresponding to an amplifier spacing of 36 km, $\kappa = 1$, and $\Delta\alpha = 0.1$. The solutions are plotted after a total propagation distance of 10,000 km or 275 amplifiers.	68
4.7	Spectral evolution over 10,000 km for an amplifier spacing of 100 km and $\Delta\alpha = 0.1$. Note that only certain frequencies, which are strongly dependent on the amplifier spacing, pass through the chain of amplifiers with unity gain. All other frequencies are attenuated.	69
4.8	Comparison of the solutions of the averaged envelope equation and the full nonlinear Schrödinger equation with loss and periodic phase-sensitive amplification, showing the out-of-phase quadrature, (a), and the difference, (b), between the two solutions. The parameters are the same as in Fig. 4.6.	71
4.9	Midpoint value of the out-of-phase quadrature plotted as a function of distance, showing the evolution between the amplifiers (calculated using the full nonlinear Schrödinger equation with loss and periodic phase-sensitive amplification). The exponential decay due to loss between the amplifiers has been factored out. The magnitude grows after an amplifier, but upon reaching the next one it is sharply attenuated. Here the amplifier spacing is 50 km, and the distance is in terms of dispersion lengths ($z = 1$ corresponds to 500 km).	72

- 4.10 Midpoint value of the in-phase quadrature just after an amplifier plotted as a function of distance (dispersion lengths). Results from both the averaged equation (dashed curve), Eq. (3.28), and the full NLS equation with loss and periodic phase-sensitive amplification (solid curve) are plotted. The two are virtually indistinguishable. The parameters are $\Gamma l = 1.0$, $\kappa = 1$, and $\Delta\alpha = 0.1$. A total propagation distance of 100,000 km or 2750 is shown. Note that an approximate steady-state is not reached until after the pulse has propagated roughly 50,000 km. 73
- 4.11 Comparison of the solutions of the averaged envelope equation (dotted lines) and the full nonlinear Schrödinger equation with loss and periodic phase-sensitive amplification (solid lines), for both the in-phase, (a), and out-of-phase, (b), quadratures. The parameters are $\Gamma l = 2.76$, corresponding to an amplifier spacing of 100 km, $\kappa = 1$, and $\Delta\alpha = 0.05$. The solutions are plotted after a total propagation distance of 10,000 km or 100 amplifiers. 74
- 4.12 Qualitative comparison of pulse solutions showing the amount of dispersive radiation shed by the soliton-based communication systems employing erbium amplifiers, (a), and PSAs, (b). In both cases the initial pulse amplitude was taken to be 10% higher than the optimum (for a fixed width). The system employing PSAs, (b), generates considerably less linear dispersive radiation with such an initial condition. For these simulations, the dispersion length was taken to be 411 km, the amplifier spacing was 50 km, and the gain of the amplifiers was set to exactly cancel the fiber loss between the amplifiers. [18] 75
- 5.1 Plot of the neutral stability curve ($\sigma = 0$) in the wavenumber k versus overamplification $\Delta\alpha$ plane. Note that the most unstable wavenumber, $k = 0$, corresponds to a value of $\Delta\alpha = 1/4$ 80
- 5.2 Qualitative depiction of the scalings associated with the neutral stability curve ($\sigma = 0$) in the k^2 versus $\Delta\alpha$ plane. Note the quadratic relation between the squared wavenumber and overamplification. 81

5.3	Characteristic behavior of the subcritical bifurcation emanating from $(U, \Delta\alpha) = (0, 1/4)$. Note that S (solid line) corresponds to the stable branch of solutions and U (dashed line) to the unstable branch.	83
5.4	Depiction of the maximum amplitude U as a function of the parameter Γl for the values of $\Delta\alpha = 0.1$ and $\Delta\alpha = 0.2$	88
5.5	Comparison of steady-states computed via AUTO versus full numerical simulations of the averaged evolution. Three pulse profiles are depicted corresponding to the AUTO solution and the averaged evolution for values of $\bar{\xi} = 20$ and $\bar{\xi} = 50$. In (a) $\tau \in [0, 12]$. (b) contains the interval $\tau \in [2, 6]$ which further depicts the difference in the three solutions. Note that as $\bar{\xi}$ gets large, the averaged solution approaches the steady-state solution generated via AUTO.	89
5.6	Bifurcation diagrams associated with the averaged envelope equation. The solid lines correspond to stable solutions while the dashed line corresponds to the unstable. In each case, the $U = 0$ solution is stable (unstable) for $\Delta\alpha < (>)1/4$. (a),(b),(c) and (d) depict the subcritical bifurcation from $\Delta\alpha = 1/4$ and the location of the limit point for the values of $\Delta\alpha = .02, 1, 2, 100$ respectively. Note that as Γl is increased from near zero to infinity, the limit point moves from $\Delta\alpha \sim 0$ to $\Delta\alpha \sim 0.088$	91
5.7	Solution curves in the amplitude versus Γl plane. The solution curves correspond to differing values of the overamplification parameter $\Delta\alpha$. Note the isola which exists for values of $\Delta\alpha < 0.088$. As the overamplification becomes larger however, the solution branches separate into an upper and lower branch corresponding to stable and unstable branch solutions of the pulse propagation.	92
5.8	Qualitative structure of the bifurcation diagram associated with the averaged evolution. This is essentially a combination of the previous two figures which depict the amplitude versus. $\Delta\alpha$ and amplitude versus. Γl planes respectively.	93

6.1	Depiction of the frequency windows which allow the propagating pulse to experience unity gain. Note that for these windows, the fiber-PSA line becomes effectively ‘transparent’.	99
6.2	Qualitative depiction of the periodic structure associated with the two amplifier spacing case	101
6.3	Depiction of the phase-locked quadrature dynamics for the two amplifier case. Note the periodic structure associated with the two amplifier spacing case.	106
6.4	Pulse evolution in the Fourier domain over 9,000 km for the case when two distinct amplifier spacings are considered, namely 80 km and 100 km. The alternating amplifier spacings help reduce the sideband generation, i.e., compare this with the spectral evolution given by Fig. 4.6 in Chapter 4.	107
6.5	Numerical simulations of the averaged equation for two distinct amplifier spacings. As with the previous results of Chapter 4, note that the pulse asymptotically approaches the final steady-state as it propagates in ξ . In (a) and (b) the initial conditions used were $U(0, \tau) = 0.9 \operatorname{sech} \tau$ and $U(0, \tau) = 1.4 \operatorname{sech} \tau$ respectively. Further, in both cases $\Delta\alpha = 0.1$, and the two amplifier lengths considered were 80 km and 100 km. . .	108
6.6	Spectral composition of a pulse after 18,000 km for a single amplifier spacing of 90 km (a) and the two amplifier spacing case with 80 km and 100 km (b). Note that the sharp sideband frequencies in (a) are reduced through the alternating spacings of (b).	109
6.7	Comparison of the dispersive radiation field generated over 18,000 km using a single amplifier spacing of 90 km (large oscillations) versus the two amplifier spacing case for 80 km and 100 km (smaller oscillations). Note that the two amplifier case attenuates the radiation by nearly an order of magnitude.	110

6.8 Bifurcation diagrams for the averaged evolution equation with two distinct amplifier spacings. In particular, (a) represents the bifurcation diagram when the amplifier spacings of 80 km and 100 km are used, i.e $\Gamma l_1 \sim 2.21$ and $\Gamma l_2 \sim 2.76$ respectively. In (b), the amplifier spacings of 36 km and 72 km (corresponding to $\Gamma l_1 = 1$ and $\Gamma l_2 = 2$) are considered. Note that these bifurcation diagrams are similar to those found in Chapter 5 and suggest the existence of a wide range of parameters which support stable pulse propagation.	111
6.9 Comparison of the dispersive radiation field generated over 18,000 km using the two amplifier spacings of 70 - 110 km (smaller oscillations) and 80 - 100 km (larger oscillations) respectively. In this case the 70 - 110 km spacing is significantly smaller than the 80 - 100 km case which was nearly an order of magnitude smaller than its single amplifier counterpart.	112
6.10 Behavior of the phase-locked quadrature amplitude which propagates through a chain of randomly spaced phase-sensitive amplifiers	114
6.11 Comparison of the spectral components after 200 amplifiers of three distinct amplification schemes which utilize PSAs. In (a), periodically-spaced PSAs are considered with an amplifier spacing of 80 km. An alternating spacing of 70 km and 90 km is considered in (b) while uniformly distributed amplifiers between 70 and 90 km are considered in (c).	116
6.12 Dispersive radiation field generated from the sideband frequencies of the three amplification schemes considered in the previous figure. The two smaller dispersive fields correspond to the random and two amplifier spacings. The important thing to note is that the two amplifier spacing and the random spacing greatly reduce the amount of background radiation generated.	117

6.13 Comparison of the the primary sideband frequency for randomly spaced amplifiers for differing values of the distribution. In particular, the uniform distributions for amplifiers between 60-100 km, 70-90 km and 75-85 km are considered.	117
6.14 Investigation of the background radiation fields generated from the sideband frequencies of the previous figure. In (a), a comparison is made between the 75-85 km distribution (larger oscillations) and the 70-90 km distribution (smaller oscillations). This is followed in (b) by a comparison of the dispersive fields for the 70-90 km distribution (larger oscillations) and the 60-100 km distribution (smaller oscillations). Note that the dispersive radiation fields are approximately of $O(10^{-4})$, $O(10^{-5})$ and $O(10^{-6})$ for the uniform distributions between 75-85 km, 70-90 km and 60-100 km respectively.	118

Chapter 1

Introduction

1.1 Historical Perspective

The 1960's witnessed the development of a technological advancement which proceeded to infiltrate and change an enormous cross section of the engineering and physical sciences. This invention continues today to be a central focus of modern day research and development. This remarkable technological breakthrough is known as the laser. The laser provided for the first time an intense, coherent light source which could finally exploit the nonlinear nature of many optical materials. In particular, Franken *et al.* discovered in 1961 the first nonlinear effect in an optical crystal, namely second-harmonic generation [1]. This discovery came one year after the first successful demonstration of a working laser by Maiman [1]. The doors were now open for a wide range of physical phenomena to be investigated with the use of the laser, and many fundamental results were achieved and continue to be achieved to the present day.

Of particular interest to this dissertation is the history and development of optical fiber technology [2–4] which was made possible through the use of the laser. In 1966, optical fibers were suggested to be a good candidate for supporting optical transmission. This fact was a consequence of the guiding characteristics which the fiber possessed due to the well known principle of total internal reflection. However, propagation distances at the time were severely limited due to the power loss rates which were of the order of 10^3 dB/km. This situation changed drastically in 1970 when power loss rates were brought down to 20 dB/km. Further progress in fabrication technology proceeded to lower the loss rates even further. Specifically, a power loss

rate of 0.2 dB/km in 1979 was achieved. This remarkably low loss rate was demonstrated to be wavelength dependent and was limited primarily by the fundamental process of Rayleigh scattering. The availability of such low-loss fibers revolutionized the field of optical fiber communications and placed optical communications at the forefront of future thinking in transcontinental and transoceanic communication links.

Paralleling these landmark developments in optical fiber technology was an interesting and fundamental new area in mathematics, namely soliton theory and the inverse scattering transform for nonlinear partial differential equations. The term 'soliton' was first introduced in 1964 by Kruskal and Zabusky [5]. Their work involved numerical simulations of the Korteweg-deVries (KdV) equation with periodic boundary conditions in order to model the one-dimensional nonlinear oscillations of a lattice. They discovered the formation of solitary waves which passed through each other without deformations due to the collisions and nonlinear interactions. Consequently, these solitary waves were called solitons in view of their particle like behavior. Two years following the discovery of solitons, Gardner, Greene, Kruskal and Miura [6] succeeded in giving a mathematical interpretation to these solitary wave solutions. Using inverse scattering techniques, which were originally developed for quantum mechanics, it was found that the KdV equation could be solved exactly for a localized initial condition. In particular, the inverse scattering technique was a method by which one used an appropriate localized initial condition as the form of the potential for which a wave was to be scattered. One could then determine the scattering data and eventually the form of the pulse evolution from the localized initial condition. From this analysis, it was found that the soliton solutions corresponded to the bound states of the Schrödinger operator. Further, the particle picture of the solitary waves was made complete.

In 1973, Hasegawa and Tappert [7] were the first to suggest and show theoretically that an optical pulse propagating in a dielectric fiber was governed by the so-called nonlinear Schrödinger equation (NLS). This equation, which will be discussed further in the following chapters, incorporated the nonlinear, cubic response of the silica fiber upon the pulse intensity. At the time of its derivation, neither a fiber with low enough loss (recall that it was 1979 when the power loss rate dropped to 0.2

dB/km) or a laser which emitted light at the appropriate wavelength. Therefore, the nonlinear Schrödinger equation as a proposed model governing the pulse propagation could not be experimentally verified at the time. However, in 1980, when both an appropriate laser and low-loss fiber were available, Mollenauer *et al.* [8] demonstrated the first successful propagation of an optical soliton in a fiber.

Interestingly enough, in 1972, the year prior to Hasegawa's and Tappert's derivation of the NLS for optical solitons, Zakharov and Shabat [9] showed that the NLS could be solved using the inverse scattering method in a similar manner to that of the KdV. Here however, the inverse scattering was described by the complex eigenvalues of a 2×2 Dirac-type equation whose potential corresponded to the initial localized envelope of the NLS. The inverse scattering transform was made more rigorous and general in 1974 by the AKNS scheme developed by Ablowitz, Kaup, Newell and Segur [10]. The AKNS scheme gave a general method for which to solve a wide variety of exactly integrable nonlinear partial differential equations which included the KdV, NLS and sine-Gordon equations. This provided the basic framework and understanding behind modern day soliton theory [11]. In particular, the single soliton, two-soliton and N-soliton solutions were well understood at that time. NLS perturbation theory was then developed in an attempt to ascertain the effects of differing perturbations upon the leading-order soliton behavior [12–15]. It was found that the perturbations could have two distinct effects [16], namely perturbations could cause shifts in the characteristic soliton parameters such as the amplitude, width and frequency and perturbations could generate a background dispersive radiation field. Apart from this, the soliton solutions of the NLS were found to be remarkably robust to a wide range of perturbations.

Armed with the analytical understanding of soliton theory and its associated pulse dynamics, physically realizable communications systems based upon soliton transmission were being developed. In fact, by the end of the 1980's, the bit rate-distance product was increased by several orders of magnitude. These experimental results, which are largely due to Mollenauer, reaffirmed the importance and potential of optical communications systems. Currently, Mollenauer and Nakazawa lead the continued experimental effort to achieve higher bit-rate distance products with min-

imal error over large, transoceanic distances. Moreover, it is apparent at this point that nonlinear optical fibers are the future in high-speed, long-distance communications systems which is hoped will eventually link the world in some kind of global network.

1.2 Recent Issues

Although much progress has been made in the development of soliton-based communications systems, there are many issues which arise in physical systems which must be addressed from both an experimental and theoretical standpoint. Of particular interest in this dissertation are some of the theoretical issues which are involved in understanding the pulse dynamics through fiber segments which contain periodically-spaced amplifiers.

Specifically, when considering a physically realizable long-distance communications system [17, 18], it becomes necessary to compensate for the attenuation experienced by a propagating pulse due to the Rayleigh scattering mentioned in the last section. Typically, a long-distance fiber optic communications link consists of segments of fiber with amplifiers placed periodically along the link to balance the loss associated with each segment of the fiber [19]. Therefore, the amplitude of the propagating pulse experiences $O(1)$ changes in its amplitude as it propagates over long distances. It then becomes necessary to understand how these amplitude changes modify the effective pulse evolution over long-distances.

Often in cases of physical interest, the amplifier spacing can be assumed to be much smaller than the typical dispersion length of the fiber. This assumption implies that the periodic effect of the gain and loss can be thought of as rapid fluctuations when considered from the viewpoint of the length scale of the soliton period. Therefore, the gain-loss forcings of the governing NLS can be averaged over in order to derive some effective evolution of the pulse propagation. Recently, Hasegawa and Kodama [18] have considered pulse propagation in optical fibers where the loss is balanced by a chain of periodically spaced erbium-doped amplifiers. Upon performing the averaging via a Lie transform method, the effective pulse evolution is shown to be

governed to leading order by the NLS equation. Therefore, when considering these phase-insensitive amplifiers, i.e., the erbium-doped amplifiers, the leading order evolution remains Hamiltonian in nature. Further, this loss-gain NLS system is robust to a wide variety of perturbations. Hasegawa and Kodama refer to the solution of the averaged pulse propagation as the guiding-center soliton. These results provide further evidence for the existence and stability of soliton solutions in a physically realizable communications system.

Experimentally, the use of periodically spaced phase-insensitive amplifiers has indeed been shown to be an effective method for compensating for the attenuation experienced in the fiber. However, the erbium-doped fiber amplifiers work based upon a population inversion. Therefore, there is a small amount of spontaneous emission noise which is incorporated into the propagating pulse through the amplifiers. This noise, along with acoustic noise [20], is responsible for the so-called Gordon-Haus timing jitter [21], i.e., the random walk of solitons caused by the spontaneous emission noise present in the erbium-doped amplifier or by the acoustic noise. This timing jitter imposes a fundamental limit upon the bit rate-distance product. And although several filtering schemes [22] have been developed to help reduce this effect, it still remains a significant restriction in a fiber line which incorporates periodically-spaced erbium-doped amplifiers.

As an alternative, the use of periodically spaced phase-sensitive amplifiers (PSAs) has been proposed as a method for compensating for the loss experienced by a propagating pulse. Because PSAs are free of spontaneous emission noise [23,24] (they are ideal quantum-limited amplifiers with a 0 dB noise figure), they do not contribute to the Gordon-Haus jitter of the propagating solitons and therefore lead to a possible increase in the maximum allowable bit rate-distance product. In contrast with the phase-insensitive amplifiers, PSAs naturally filter in the phase of the propagating pulse. Therefore, the PSAs exhibit a preferred direction of amplification which will be discussed more fully in the body of this dissertation.

Just as with its phase-insensitive counterpart, the rapid fluctuations due to the loss and phase-sensitive gain can again be averaged over in order to determine the effective pulse evolution [25]. This analysis is at the center of the following chapters

and constitutes the body of this dissertation. The questions which must be addressed are those same questions which were addressed for the phase-insensitive amplifiers, namely, does the use of periodically spaced phase-sensitive amplifiers support stable soliton-like pulse propagation, and how robust are the localized solutions to perturbations? In the following chapters, the analysis will strongly suggest that a fiber-PSA line will be capable of supporting robust soliton-like pulse propagation over distances which are much longer than the typical soliton period.

Chapter 2

The Phase-Sensitive Amplifier

2.1 Introduction

The aim of this chapter is to systematically derive, using an asymptotic reduction, the governing set of equations which describe the dynamics of a physically realizable phase-sensitive amplifier (PSA). In particular, the PSA considered will be that corresponding to a degenerate optical parametric amplifier. An optical parametric amplifier is essentially a description of the interaction of three electromagnetic fields in a quadratic $\chi^{(2)}$ medium [1, 26]. In this process, a weak signal field at frequency ω_1 is amplified by a much stronger pump field at frequency ω_3 . This interaction in the quadratic medium generates a third field, known as the idler, at frequency ω_2 such that

$$\omega_3 = \omega_1 + \omega_2. \quad (2.1)$$

From a quantum mechanical viewpoint, this process of three wave interaction can be thought of as the annihilation of one photon at ω_3 creating simultaneously two photons at ω_1 and ω_2 and vice-versa. This behavior is depicted in Fig. 2.1. Since the pump field is considered to be much stronger than either the signal or idler fields, most of the interaction will serve to convert pump photons into signal and idler photons. And although the reverse is possible, very few idler and signal photons will be converted into pump photons due to their weak field strengths.

Starting from Maxwell's equations, a set of three coupled amplitude equations will be derived for the signal, idler and pump fields. In the asymptotic reduction carried out to derive the respective amplitude equations, several major assumptions

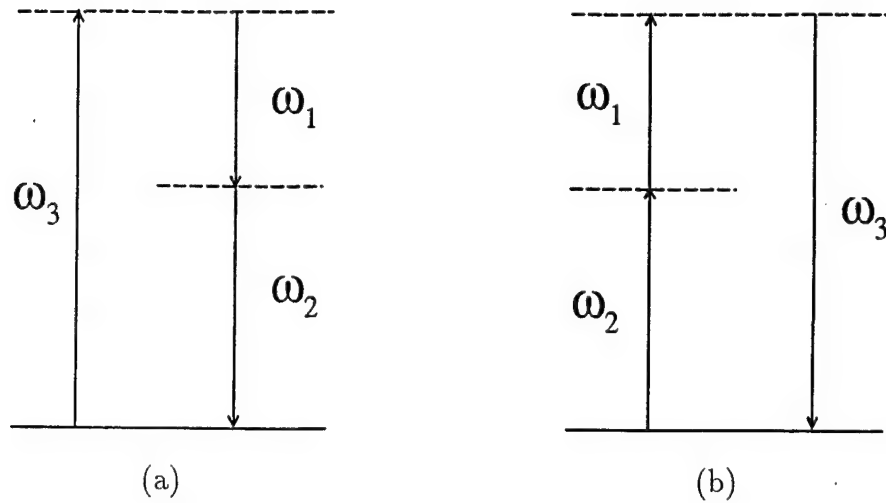


Figure 2.1: Photon description of the interaction of three fields at frequencies ω_1 , ω_2 and ω_3 . In (a) the process of parametric amplification is depicted, i.e., two photons are created at ω_1 and ω_2 with the annihilation of a single photon at ω_3 . In (b) the reverse is shown, the two photons at ω_1 and ω_2 are simultaneously annihilated to create a photon at ω_3 . This is known as sum-frequency generation.

and simplifications will be made. These include the assumption of high-frequency (large-wavenumber) quasi-monochromatic pulses with slowly varying envelopes and the paraxial waveguide approximation [1, 26]. The high-frequency asymptotics to be carried out is reminiscent of a WKB geometrical-optics approach for rapidly-oscillating carrier waves. Once the amplitude equations have been derived, they will be normalized on the characteristic scalings of a physically realizable system which will then determine the leading order behavior associated with this particular phase-sensitive amplifier. In general, differing types of PSAs can be considered. However, it can be shown that they have the same qualitative leading order behavior. Therefore, the degenerate, parametric amplifier will serve as a standard example of a phase-sensitive amplifier.

2.2 Maxwell's Equations

As with all electromagnetic phenomena, the propagation of an optical field in a given medium is governed by Maxwell's equations. These equations are given by the following

$$\nabla \times \mathbf{E} = -\frac{\partial \mathbf{B}}{\partial t}, \quad (2.2a)$$

$$\nabla \times \mathbf{H} = \mathbf{J}_f + \frac{\partial \mathbf{D}}{\partial t}, \quad (2.2b)$$

$$\nabla \cdot \mathbf{D} = \rho_f, \quad (2.2c)$$

$$\nabla \cdot \mathbf{B} = 0. \quad (2.2d)$$

Here the electromagnetic field is denoted by $\mathbf{E} = \vec{E}(z, \vec{x}_T, t)$ where $\vec{x}_T \equiv (x, y)$ is the vector transverse to the direction of propagation and the magnetic field is denoted by the vector \mathbf{H} in a similar way. The \mathbf{D} and \mathbf{B} fields represent the corresponding electric and magnetic flux densities. In the absence of free charges, which is the case of interest, the current density and free charge density are both identically zero, i.e., $\mathbf{J}_f = 0$ and $\rho_f = 0$.

The flux densities \mathbf{D} and \mathbf{B} arise due to the electric and magnetics fields which propagate within a given medium. Therefore, they reflect the constitutive laws of any given material and are related to the electric and magnetics fields in the following way

$$\mathbf{D} = \epsilon_0 \mathbf{E} + \mathbf{P} = \epsilon \mathbf{E} \quad (2.3a)$$

$$\mathbf{B} = \mu_0 \mathbf{H} + \mathbf{M}, \quad (2.3b)$$

where ϵ_0 and μ_0 are the free space permittivity and free space permeability respectively, and \mathbf{P} and \mathbf{M} are the induced electric and magnetic polarizations. At optical frequencies, which is the case of interest, $\mathbf{M} = 0$. In Eq. (2.3a), the \mathbf{D} field can also be expressed as $\epsilon \mathbf{E}$ where ϵ captures any nonlocal, linear and nonlinear response of the medium to the applied electric field.

In what follows, interest will be given solely to the electric field and the induced polarization. The magnetic field, which is related to its electric field counterpart through the Maxwell's equations, can be effectively ignored. As a consequence, it becomes advantageous to express Maxwell's equations in terms of the \mathbf{E} and \mathbf{P} fields alone. Upon taking the curl of Eq. (2.2a) and making use of Eqs. (2.2b), (2.3a) and (2.3b), the full-vector Maxwell's equations for the electric field can be given by

$$\nabla^2\mathbf{E} - \nabla(\nabla \cdot \mathbf{E}) - \frac{1}{c^2} \frac{\partial^2 \mathbf{E}}{\partial t^2} = \mu_0 \frac{\partial^2 \mathbf{P}(\mathbf{E})}{\partial t^2}, \quad (2.4)$$

where $c = 1/\sqrt{\epsilon_0 \mu_0}$ is the speed of light in vacuo and use has been made of the vector identity $\nabla \times \nabla \times \mathbf{E} = \nabla(\nabla \cdot \mathbf{E}) - \nabla^2\mathbf{E}$. Here the polarization vector $\mathbf{P}(\mathbf{E})$ depends upon the electric field and the constitutive relations for the material in which the field is propagating. Therefore, $\mathbf{P}(\mathbf{E})$ must be modeled in such a way as to account for both the linear and nonlinear responses of the medium to the applied electromagnetic field.

In order to give a realistic description of the constitutive laws associated with the material of interest, the polarization field $\mathbf{P}(\mathbf{E})$ is modeled as follows

$$\begin{aligned} \frac{\mathbf{P}}{\epsilon_0} = & \int_{-\infty}^t dt_1 \chi^{(1)}(t-t_1) \cdot \mathbf{E}(t_1) + \int \int_{-\infty}^t dt_1 dt_2 \chi^{(2)}(t-t_1, t-t_2) : \mathbf{E}(t_1) \mathbf{E}(t_2) \\ & + \int \int \int_{-\infty}^t dt_1 dt_2 dt_3 \chi^{(3)}(t-t_1, t-t_2, t-t_3) : \mathbf{E}(t_1) \mathbf{E}(t_2) \mathbf{E}(t_3). \end{aligned} \quad (2.5)$$

In the above expression, note that $\chi^{(n)}$ denotes an $(n+1)$ rank tensor which is contracted with the given electric field vectors. The linear response is represented by the first term in the expression, whereas the quadratic and cubic responses are given by the following two terms respectively. Eq. (2.5) represents a general, nonlinear response of the medium to an applied electric field. It is interesting to note that the medium response is not instantaneous. Rather, the response is temporally retarded due in part to the collective inertia of the electrons as they adjust to the applied electric field. Mathematically, this relaxation process is what accounts for the integral convolutions, which represent the electric field history, over the appropriate time-decaying response kernels $\chi^{(1)}$, $\chi^{(2)}$ and $\chi^{(3)}$. However, it should be understood that the dominant behavior of each kernel corresponds to an impulse response to the

applied electric field. Note that the integrals in Eq. (2.5) are evaluated only up to time t due to causality constraints imposed on the physical system, i.e the future electric field does not contribute to the present medium response. Also, note that the response kernels are dependent on the time differences alone. This is a consequence of the time invariance of the medium response. In other words, the medium response should be identical if the electric field is applied at either time T or time $T + T_0$.

In order to simplify the governing equations, i.e., Eq. (2.4) and Eq. (2.5), it is convenient to assume the electric field to be polarized along one direction in the medium of propagation, i.e., assume $\mathbf{E} = E(z, t)\hat{\mathbf{k}}$. This is consistent with the paraxial waveguide approximation which is used to neglect the dependence of the electric field upon the transverse structure. This simplification modifies the spatial operators of Eq. (2.4) in the following manner; the Laplacian operator becomes a function of the z scale alone, i.e., $\nabla^2 = \frac{\partial^2}{\partial z^2} + \nabla_T^2 \rightarrow \frac{\partial^2}{\partial z^2}$. Further, note that $\nabla \cdot \mathbf{D} = 0$ implies $\nabla \epsilon \cdot \mathbf{E} + \epsilon \nabla \cdot \mathbf{E} = 0$. Upon assuming ϵ depends only on the space coordinate through its dependence on \mathbf{E} , it is found that $\nabla \epsilon \cdot \mathbf{E} = 0$ which in turn implies $\nabla \cdot \mathbf{E} = 0$. Therefore the gradient of the dot product ($\nabla \cdot \mathbf{E}$) can be neglected. As a final simplification, the polarization given in Eq. (2.5) can be simply rewritten as the sum of a linear and nonlinear part. In particular, $\mathbf{P} = \mathbf{P}^L + \mathbf{P}^{NL}$ where \mathbf{P}^L includes the convolution of the electric field over $\chi^{(1)}$ and \mathbf{P}^{NL} represents the convolutions over the nonlinear quadratic and cubic terms. With these simplifications and assumptions in mind, Eqs. (2.4) and (2.5) reduce to the following one dimensional wave formulation of Maxwell's equations

$$\frac{\partial^2 E}{\partial z^2} - \frac{1}{c^2} \frac{\partial^2}{\partial t^2} (\epsilon * E) = \mu_0 \frac{\partial^2 P^{NL}}{\partial t^2} \quad (2.6)$$

where

$$\epsilon * E = E(t) + \int_{-\infty}^t dt_1 \chi^{(1)}(t - t_1) E(t_1) \quad (2.7)$$

and

$$\begin{aligned} \frac{P^{NL}}{\epsilon_0} = & \int \int_{-\infty}^t dt_1 dt_2 \chi^{(2)}(t - t_1, t - t_2) E(t_1) E(t_2) + \\ & \int \int \int_{-\infty}^t dt_1 dt_2 dt_3 \chi^{(3)}(t - t_1, t - t_2, t - t_3) E(t_1) E(t_2) E(t_3). \end{aligned} \quad (2.8)$$

Here, it is further assumed that all field frequencies are far from any resonances of the nonlinear material, and therefore, Kleinman symmetry holds. This allows the quadratic medium response to be expressed in terms of the d -coefficient associated with the $\chi^{(2)}$ nonlinearity. It is within the framework of this formulation that the amplitude equations for the signal, idler and pump fields will be derived.

Thus far, the only assumptions made on the electric field dynamics are that of the paraxial waveguide approximation and a single direction of polarization. In order to simplify Eq. (2.6) given the relations in Eqs. (2.7) and (2.8), further approximations involving the three wave interaction will be considered. In particular, two major assumptions will be made concerning the electric field. The first of these assumptions utilizes the fact that the signal, idler and pump fields correspond to the frequencies ω_1, ω_2 and ω_3 respectively. In particular, assume the electric field to be of the form

$$E(z, t) = \mathcal{E}_1(z, t)e^{i(k_1 z - \omega_1 t)} + \mathcal{E}_2(z, t)e^{i(k_2 z - \omega_2 t)} + \mathcal{E}_3(z, t)e^{i(k_3 z - \omega_3 t)} + \text{c.c.}, \quad (2.9)$$

where the $\mathcal{E}_1, \mathcal{E}_2$ and \mathcal{E}_3 represent slowly varying envelopes in both time and space and c.c. represents the complex conjugate. This assumption, known as the quasi-monochromatic pulse approximation, allows the governing equations to be separated into appropriate frequency components. One further aspect of this approximation, which was touched on earlier, lies within the high-frequency/large-wavenumber regime. In particular, for high-frequencies, Eq. (2.9) can be thought of as rapidly-oscillating WKB-type waves. Since it is well known that the WKB method is essentially the background theory for optical rays, the form of solution given in Eq. (2.9) is consistent with the idea of guided modes confined by the transverse inhomogeneity of the index of refraction of the medium of propagation. A reductive perturbation scheme can now be carried out utilizing the assumptions concerning the high-frequency, quasi-monochromatic waves with slowly varying envelopes.

Before proceeding further, a final assumption is made which concerns the nonlinear polarization terms P^{NL} . In order to make tractable the convolutions over the nonlinear terms, the response to the electric field is assumed to be instantaneous. Although this approximation ignores the time-delayed response of the medium, the

approximation captures the dominant effects associated with the nonlinearities and allows for a relatively simple and analytically tractable analysis. This assumption on P^{NL} is a good approximation provided the pulse widths of interest are much greater in duration than the relaxation times of the medium of interest. Formally, this assumption is modeled by assuming the convolution kernels to be of the following form

$$\chi^{(2)}(t - t_1, t - t_2) = \chi^{(2)}\delta(t - t_1)\delta(t - t_2) \quad (2.10a)$$

$$\chi^{(3)}(t - t_1, t - t_2, t - t_3) = \chi^{(3)}\delta(t - t_1)\delta(t - t_2)\delta(t - t_3), \quad (2.10b)$$

where $\chi^{(2)}$ and $\chi^{(3)}$ are now scalars which measure the strength of the nonlinear response of the medium in question. It will later be assumed that in the materials of physical interest, the quadratic term dominates the cubic nonlinearity and therefore, the cubic nonlinearity can be neglected. For the present, however, the dominant effect associated with the cubic nonlinearity will be kept in the analysis. The evaluation of the nonlinear convolutions now becomes a trivial matter and the reductive perturbation scheme is continued.

Upon inserting Eq. (2.9) into Eq. (2.6) and using Eq. (2.10) above, the following expression can be derived for the terms which are proportional to $\exp(i(k_1 z - \omega_1 t))$,

$$\begin{aligned} & e^{i(k_1 z - \omega_1 t)} \left[\frac{\partial^2 \mathcal{E}_1}{\partial z^2} + 2ik_1 \frac{\partial \mathcal{E}_1}{\partial z} - k_1^2 \mathcal{E}_1 \right] \\ & - \frac{1}{c^2} \frac{\partial^2}{\partial t^2} \left[e^{i(k_1 z - \omega_1 t)} \left(\mathcal{E}_1(z, t) + \int_{-\infty}^t dt_1 \chi^{(1)}(t - t_1) \mathcal{E}_1(z, t_1) e^{i\omega_1(t-t_1)} \right) \right] \\ & = \mu_0 \epsilon_0 \frac{\partial^2}{\partial t^2} \left[e^{i(k_1 z - \omega_1 t)} (\chi^{(2)} \mathcal{E}_2^* \mathcal{E}_3 e^{i\Delta kz} + \chi^{(3)} |\mathcal{E}_3|^2 \mathcal{E}_1) \right], \end{aligned} \quad (2.11)$$

Here \mathcal{E}_1 represents the slowly-varying amplitude of the signal field, $\Delta k = k_3 - k_1 - k_2$ represents the wavenumber mismatch and the pump field has been assumed to be much larger than either that of the signal or idler fields, i.e., $\|\mathcal{E}_1\|, \|\mathcal{E}_2\| \ll \|\mathcal{E}_3\|$. Only those terms proportional to $\exp(i(k_1 z - \omega_1 t))$ are kept due to their resonance behavior, i.e., higher harmonics are neglected in the present analysis. Similar expressions can be obtained for those terms which are proportional to $\exp(i(k_2 z - \omega_2 t))$ and $\exp(i(k_3 z - \omega_3 t))$.

$\omega_3 t$). These then would correspond to the amplitude equations associated with the idler and pump fields respectively.

The linear convolution of the electric field can be evaluated using the appropriate change of variables $\xi = t - t_1$. It then follows that

$$\int_{-\infty}^t dt_1 \chi^{(1)}(t - t_1) \mathcal{E}_1(z, t_1) e^{i\omega_1(t-t_1)} = \int_0^\infty d\xi \chi^{(1)}(\xi) \mathcal{E}_1(z, t - \xi) e^{i\omega_1 \xi}. \quad (2.12)$$

Since the function $\chi^{(1)}$ is primarily considered an impulse (instantaneous) response to the applied electric field, it can be argued that \mathcal{E}_1 is slowly-varying in time and space in comparison with this dominant impulse response, i.e., \mathcal{E}_1 is slowly-varying in comparison to the response time of $\chi^{(1)}$. Therefore, the \mathcal{E}_1 can be expanded in a Taylor series as follows,

$$\mathcal{E}_1(z, t - \xi) = \mathcal{E}_1(z, t) - \xi \frac{\partial \mathcal{E}_1(z, t)}{\partial t} + \frac{1}{2} \xi^2 \frac{\partial^2 \mathcal{E}_1(z, t)}{\partial t^2} + \dots \quad (2.13)$$

Introducing this expansion into the Eq. (2.12) and noting the following

$$\begin{aligned} \hat{\chi} &= \int_0^\infty \chi^{(1)}(\xi) e^{i\omega_1 \xi} d\xi \\ -i \frac{\partial \hat{\chi}}{\partial \omega_1} &= \int_0^\infty \chi^{(1)}(\xi) e^{i\omega_1 \xi} \xi d\xi \\ - \frac{\partial^2 \hat{\chi}}{\partial \omega_1^2} &= \int_0^\infty \chi^{(1)}(\xi) e^{i\omega_1 \xi} \xi^2 d\xi, \end{aligned}$$

it can be found that

$$\int_{-\infty}^t dt_1 \chi^{(1)}(t - t_1) \mathcal{E}_1(z, t_1) e^{i\omega_1(t-t_1)} = \hat{\chi} \mathcal{E}_1 - i \hat{\chi}_{\omega_1} \frac{\partial \mathcal{E}_1}{\partial t} - \hat{\chi}_{\omega_1 \omega_1} \frac{\partial^2 \mathcal{E}_1}{\partial t^2}, \quad (2.14)$$

where the subscripts on $\hat{\chi}$ now denote differentiation with respect to ω_1 , i.e., $\hat{\chi}_{\omega_1} = \partial \hat{\chi} / \partial \omega_1$ and $\hat{\chi}_{\omega_1 \omega_1} = \partial^2 \hat{\chi} / \partial \omega_1^2$. In order to make use of Eq. (2.14), it must be multiplied by a factor of $\exp(i(k_1 z - \omega_1 t))$ and differentiated twice with respect to time. This will then give the appropriate linear response of the medium to the applied electric field.

In considering the nonlinear response of the medium to an applied electric field, the primary interest is upon the dominant behavior described by the foregoing model of Eqs. (2.8) and (2.10). Therefore, upon differentiating the right hand side

of Eq. (2.11), only the leading order terms are kept for both the cubic and quadratic nonlinearities. It is important to remember that the envelope amplitude is slowly-varying in time and space. Therefore, each spatial or time derivative lowers the term in question by an order of magnitude. These small effects may be investigated, but they are not of interest in what will follow.

Upon combining the preceding results, noting that the envelope is slowly-varying in time and space, and simplifying, it is found that the signal field envelope is governed by

$$\frac{\partial^2 \mathcal{E}_1}{\partial z^2} + 2ik_1 \frac{\partial \mathcal{E}_1}{\partial z} - k_1^2 \mathcal{E}_1 + \frac{1}{c^2} \left[\omega_1^2 (1 + \hat{\chi}) \mathcal{E}_1 + i[(\omega_1^2 \hat{\chi})_{\omega_1} + 2\omega_1] \frac{\partial \mathcal{E}_1}{\partial t} \right. \\ \left. - \frac{1}{2} [(\omega_1^2 \hat{\chi})_{\omega_1 \omega_1} + 2] \frac{\partial^2 \mathcal{E}_1}{\partial t^2} + \dots \right] = -\frac{\omega_1^2}{c^2} [\chi^{(2)} \mathcal{E}_2^* \mathcal{E}_3 e^{i\Delta kz} + \chi^{(3)} |\mathcal{E}_3|^2 \mathcal{E}_1 + \dots], \quad (2.15)$$

where the dots represent the higher order terms, both linear and nonlinear, associated with the material response. The aim is to now make use of the reductive perturbation scheme in order to balance at subsequent orders those effects which are of the same order of magnitude. In considering Eq. (2.15), it must be kept in mind that derivatives with respect to time and space become smaller. Further, it must also be recalled that the high-frequency/large-wavenumber limit is being considered. Therefore, the leading order balance gives

$$k_1^2 = \frac{\omega_1^2}{c^2} (1 + \hat{\chi}_R), \quad (2.16)$$

where $\hat{\chi}_R$ represents the real part of $\hat{\chi}$. This then determines the dispersion relation $\omega_1(k_1)$ or $k_1(\omega_1)$. Since the phase velocity is given by $c_p = \omega_1/k_1 = c/\sqrt{1 + \hat{\chi}_R(\omega_1)}$, the index of refraction can then be expressed as a function of the linear response, i.e., $n(\omega_1) = \sqrt{1 + \hat{\chi}_R(\omega_1)}$. This is the index of refraction attributed solely to the linear response. The nonlinear terms can act to modify this index of refraction depending upon the magnitude of the interacting fields.

From Eq. (2.16), it is easy to show that the following relations now hold

$$2k_1 k_1' = \frac{1}{c^2} [(\omega_1^2 \hat{\chi}_R)_{\omega_1} + 2\omega_1] \\ k_1 k_1'' + (k_1')^2 = \frac{1}{2c^2} [(\omega_1^2 \hat{\chi}_R)_{\omega_1 \omega_1} + 2],$$

where the prime now denotes differentiation with respect to ω_1 . These expressions are used in conjunction with Eq. (2.15) in order to show the following

$$\begin{aligned} 2ik_1 \left(\frac{\partial \mathcal{E}_1}{\partial z} + k'_1 \frac{\partial \mathcal{E}_1}{\partial t} \right) + \frac{\partial^2 \mathcal{E}_1}{\partial z^2} - [k_1 k''_1 + (k'_1)^2] \frac{\partial^2 \mathcal{E}_1}{\partial t^2} \\ = -\frac{\omega_1^2}{c^2} [\chi^{(2)} \mathcal{E}_2^* \mathcal{E}_3 e^{i\Delta kz} + \chi^{(3)} |\mathcal{E}_3|^2 \mathcal{E}_1]. \end{aligned} \quad (2.17)$$

Thus, the reductive perturbation method along with the various assumptions and approximations have reduced the governing Maxwell's equations to the amplitude equation (2.17).

A coordinate change can further simplify the form of Eq. (2.17). From an optics viewpoint, it is preferred that the pulse be viewed from a fixed position as a function of time. The transformation into this moving coordinate system is easily carried out by introducing the following change of variables

$$\begin{aligned} \eta &= t - \frac{1}{v_{1g}} z \\ \zeta &= z, \end{aligned}$$

where $v_{1g} = 1/k'_1$ is the group velocity of the signal field. This change of variables will modify both the spatial and temporal derivatives in Eq. (2.17). Performing the change of variables into the 'center-of-mass' frame of the signal field and keeping only the leading order terms, it is found that

$$\frac{\partial \mathcal{E}_1}{\partial \zeta} + \frac{\omega_1^2 \chi_I}{2k_1 c^2} \mathcal{E}_1 = -i \frac{k''_1}{2} \frac{\partial^2 \mathcal{E}_1}{\partial \eta^2} + i \frac{\omega_1^2}{2k_1 c^2} (\chi^{(2)} \mathcal{E}_2^* \mathcal{E}_3 e^{i\Delta kz} + \chi^{(3)} |\mathcal{E}_3|^2 \mathcal{E}_1). \quad (2.18)$$

Here, the second term on the left, which is proportional to the constant χ_I , accounts for any attenuation or absorption in the medium. The term denoted by χ_I represents the imaginary part of $\hat{\chi}$. This can be more clearly understood upon assuming that $\hat{\chi}$ has a small imaginary part, i.e., $\hat{\chi} \rightarrow \hat{\chi}_R + i\chi_I$ where $\chi_I \ll \hat{\chi}$. This can further be explored from the viewpoint of the Kramers-Kronig relations which describe the relationship between the real and imaginary parts of the index of refraction when the integral over the kernel $\chi^{(1)}$ is formulated correctly. The Kramers-Kronig relations

also imply that a medium which has an instantaneous linear response to an applied electric field is dispersionless and lossless. This is not the case of interest here. As noted above, the real part will account for the index of refraction, while the imaginary part models the loss/absorption mechanism in the medium. Therefore, the leading order behavior of the amplitude equation accounts for linear dispersion, intrinsic loss/absorption, and nonlinear coupling to the pump and idler fields.

It was noted earlier that the terms proportional to $\exp(i(k_2 z - \omega_2 t))$ and $\exp(i(k_3 z - \omega_3 t))$ could also be investigated. A procedure similar to the foregoing can be easily carried out for the amplitude equations of both the idler and pump fields. The change of variables of the idler and pump fields is made now into the signal's moving coordinate system. There will then be additional terms in both the idler and pump field equations due to the group velocity difference of the signal with that of the idler and pump. In total then, there will be three partial differential equations [27,28] which are coupled through the nonlinearities, namely,

$$\frac{\partial \mathcal{E}_1}{\partial z} + \delta_1 \mathcal{E}_1 = -ig_1 \frac{\partial^2 \mathcal{E}_1}{\partial \eta^2} + i\sigma_1(\chi^{(2)} \mathcal{E}_2^* \mathcal{E}_3 e^{i\Delta k z} + \chi^{(3)} |\mathcal{E}_3|^2 \mathcal{E}_1) \quad (2.19a)$$

$$\frac{\partial \mathcal{E}_2}{\partial z} + \delta_2 \mathcal{E}_2 = -ig_2 \frac{\partial^2 \mathcal{E}_2}{\partial \eta^2} + i\sigma_2(\chi^{(2)} \mathcal{E}_1^* \mathcal{E}_3 e^{i\Delta k z} + \chi^{(3)} |\mathcal{E}_3|^2 \mathcal{E}_2) - \nu_{21} \frac{\partial \mathcal{E}_2}{\partial \eta} \quad (2.19b)$$

$$\frac{\partial \mathcal{E}_3}{\partial z} + \delta_3 \mathcal{E}_3 = -ig_3 \frac{\partial^2 \mathcal{E}_3}{\partial \eta^2} + i\sigma_3(\chi^{(2)} \mathcal{E}_1 \mathcal{E}_2 e^{-i\Delta k z} + \chi^{(3)} |\mathcal{E}_3|^2 \mathcal{E}_3) - \nu_{31} \frac{\partial \mathcal{E}_3}{\partial \eta}, \quad (2.19c)$$

where the following constants have been defined for $i = 1, 2, 3$

$$\delta_i = \frac{\omega_i^2 \chi_I}{2k_i c^2} \quad (2.20a)$$

$$\sigma_i = \frac{\omega_i^2}{2k_i c^2} \quad (2.20b)$$

$$g_i = \frac{1}{2} \frac{\partial^2 k_i}{\partial \omega_i^2} \quad (2.20c)$$

$$\nu_{21} = \frac{1}{v_{2g}} - \frac{1}{v_{1g}} \quad (2.20d)$$

$$\nu_{31} = \frac{1}{v_{3g}} - \frac{1}{v_{1g}} \quad (2.20e)$$

$$\Delta k = k_3 - k_1 - k_2. \quad (2.20f)$$

In general, solving for the signal, idler and pump fields is a difficult task left primarily to numerical simulations. In the next section, it will be shown that much of the dominant behavior can be largely understood from simplified versions of Eqs. (2.19). However, the present model represents qualitatively all the major physical phenomena of the three wave interaction in a nonlinear medium; these include dispersion, attenuation/absorption, group-velocity mismatch, phase-mismatch and nonlinear coupling.

2.3 Degenerate Optical Parametric Amplifier

As indicated in the previous section, the full equations governing the three wave field interactions in a nonlinear medium are rendered analytically intractable in Eqs. (2.19). In what follows, a physically realizable PSA will be considered whose characteristic scalings simplify considerably the governing equations. Specifically, a degenerate parametric amplifier is considered. It is degenerate in the sense that the frequency associated with the pump field is exactly twice that of the incoming signal field. Therefore, the idler field which is created as a consequence of the signal-pump interaction is at the same frequency as that of the signal field itself, i.e., $\omega_1 = \omega_2$. The signal and idler fields can then be combined and thought of as a single ‘signal’ field. In the analysis that follows, the pump field has been assumed to be much larger in amplitude and much longer in duration than either the signal or idler fields. In particular, the pump can be assumed to be undepleted by the nonlinear interaction and can be then taken to be essentially constant. This will be made more clear from the characteristic scalings which will be introduced shortly.

Attention is now given to simplifications and approximations which are consistent with retaining the leading order behavior of the three wave interaction. In most cases of interest, i.e., materials for which parametric amplification is carried out, the quadratic nonlinearity dominates the cubic nonlinearity which allows the cubic term to be neglected in the analysis, i.e., $\chi^{(2)} \ll \chi^{(3)}$. Further, over the length scale of interest, the nonlinear medium can be considered essentially lossless. These assumptions, along with the assumption that the phase-mismatch Δk is identically zero, i.e., perfect phase-matching is achieved, simplifies significantly the equations

governing the three wave interaction.

In order to clarify these statements made concerning the pump, signal and idler fields, it becomes necessary to nondimensionalize the Eqs. (2.19) on the characteristic scales of the problem. Therefore, define the following set of nondimensional variables

$$Z = \zeta/\zeta_0 \quad (2.21a)$$

$$\xi = \eta/\eta_0 \quad (2.21b)$$

$$S = \mathcal{E}_1/\mathcal{E}_s \quad (2.21c)$$

$$I = \mathcal{E}_2/\mathcal{E}_s \quad (2.21d)$$

$$P = \mathcal{E}_3/\mathcal{E}_p, \quad (2.21e)$$

where ζ_0 corresponds to the characteristic length of the nonlinear medium, η_0 defines a characteristic pulse width of the signal field, and \mathcal{E}_s and \mathcal{E}_p define the characteristic amplitudes of the signal and pump fields respectively. Recall it has been assumed that $\Delta k = 0$, $\delta = 0$ and $\chi^{(3)} = 0$. Further, since the PSA is degenerate, $\omega_1 = \omega_2$ and the sum of the signal and idler fields becomes the effective ‘signal’ field. Eqs. (2.19) then reduce to the following

$$\frac{\partial S}{\partial Z} = -i \left(\frac{\zeta_0 g_1}{\eta_0^2} \right) \frac{\partial^2 S}{\partial \xi^2} + i(\sigma_1 \chi^{(2)} \mathcal{E}_p \zeta_0) I^* P \quad (2.22a)$$

$$\frac{\partial I}{\partial Z} = -i \left(\frac{\zeta_0 g_2}{\eta_0^2} \right) \frac{\partial^2 I}{\partial \xi^2} + i(\sigma_2 \chi^{(2)} \mathcal{E}_p \zeta_0) S^* P - \left(\frac{\nu_{21} \zeta_0}{\eta_0} \right) \frac{\partial I}{\partial \xi} \quad (2.22b)$$

$$\frac{\partial P}{\partial Z} = -i \left(\frac{\zeta_0 g_3}{\eta_0^2} \right) \frac{\partial^2 P}{\partial \xi^2} + i \left(\frac{\sigma_3 \chi^{(2)} \mathcal{E}_s^2 \zeta_0}{\mathcal{E}_p} \right) S^2 - \left(\frac{\nu_{31} \zeta_0}{\eta_0} \right) \frac{\partial P}{\partial \xi}, \quad (2.22c)$$

where use has been made of Eqs. (2.21) and (2.20).

It is convenient to establish the appropriate orders of magnitude of the various terms of Eq. (2.22). In what follows, the nonlinear medium will be assumed to be a KTP crystal (KTiOPO_4 , Potassium Titanyl Phosphate) [29]. In particular, the following characteristic measures are considered

$$\zeta_0 \sim 5 \text{ mm} \quad (2.23a)$$

$$\eta_0 \sim 50 \text{ ps} \quad (2.23\text{b})$$

$$\mathcal{E}_p/\mathcal{E}_s \sim 20 \quad (2.23\text{c})$$

$$\chi^{(2)} = 2d^{(2)} \sim 6 \times 10^{-12} \text{ m/V} \quad (2.23\text{d})$$

$$\mathcal{E}_p \sim 48 \times 10^6 \text{ V/m.} \quad (2.23\text{e})$$

The wavelength of interest, which corresponds to soliton based communications systems, is $\lambda = 1.55$ microns. Numerical simulations of the Eqs. (2.22) using Eqs. (2.23) are shown in Figs. 2.2. The initial signal and pump pulses are assumed to be hyperbolic secants while the idler field is initially zero. Note the amplification and gain associated with the signal and idler fields through a small section of KTP crystal. Moreover, note that the pump field remains largely unaffected through the interaction.

It is clear from these figures that the nonlinear interaction is the dominant effect. More precisely, it can be found that the coefficients associated with the dispersion are of $O(10^{-5})$. Note that if the dispersion can be ignored in Eqs. (2.23), then the coupled set of equations for the three wave interaction can be solved exactly via the inverse scattering transform [30]. The coefficients of nonlinear coupling for the signal and idler fields are $O(1)$ while that for the pump is of $O(10^{-2})$. The remaining terms are associated with the group-velocity mismatch and can be found to be of $O(10^{-3})$. Figures 2.3a and 2.3b represent contour plots of the pump field and the combined signal and idler fields respectively. Recall that the pump pulse was moved into the coordinate system traveling with the group velocity of the signal pulse. Therefore, the pump field drifts noticeably as seen in Fig 2.3a. However, because the pump pulse has been assumed to be wider in duration than the signal pulse, the combined signal-idler field is essentially unaffected as seen in Fig 2.3b.

Through this physical example, it has been found that the effects of the dispersion, group-velocity mismatch and nonlinear coupling of the pump field to the signal and idler can all be considered higher order effects. Therefore by considering

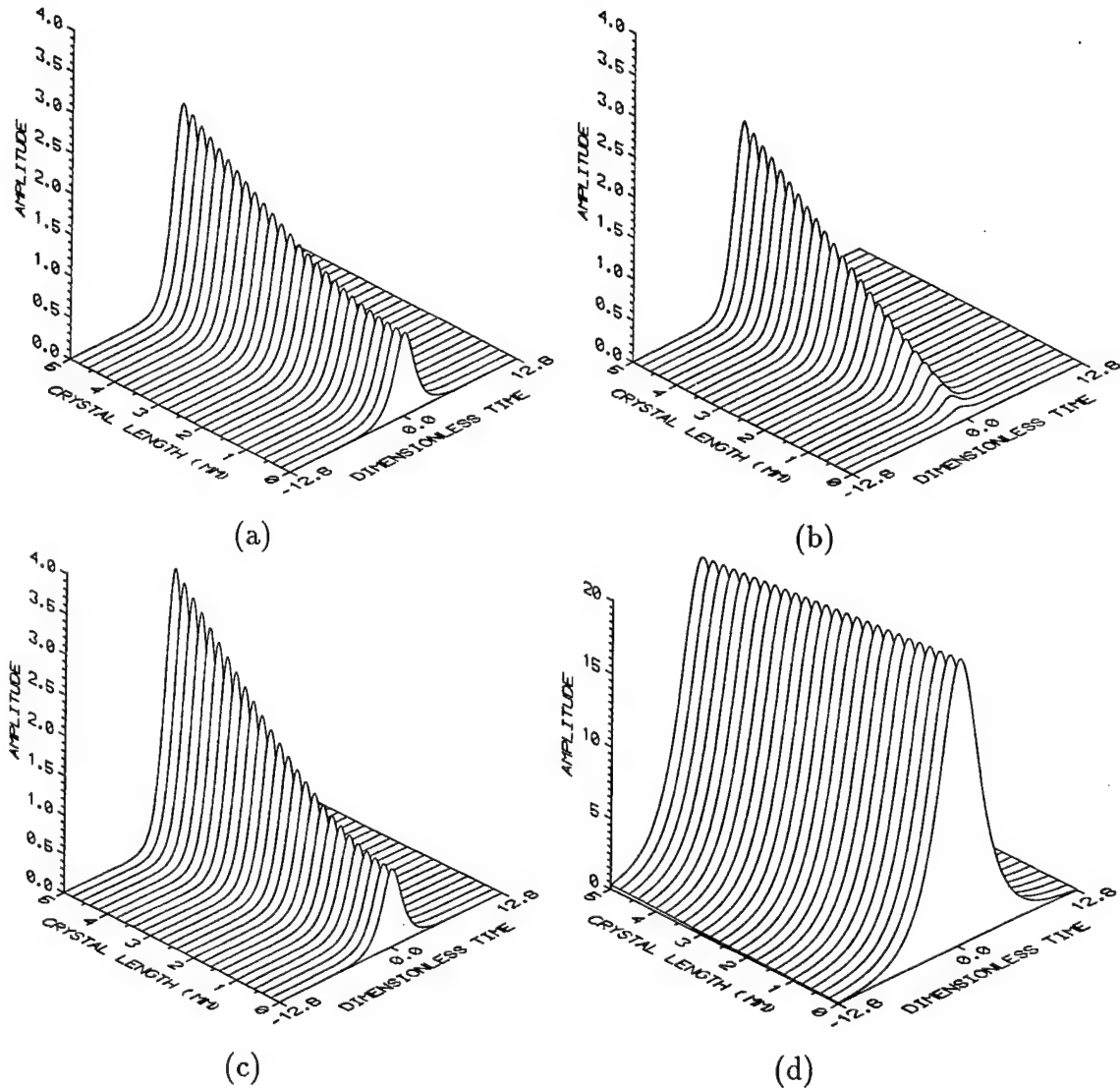


Figure 2.2: Qualitative behavior of the signal, idler, and pump fields. In (a) and (b) the signal and idler fields are depicted. The initial signal field is a hyperbolic secant while the initial idler field was zero. In (c), the combined signal and idler fields are depicted. This represents the effective ‘signal’ field output of the PSAs. The pump field in (d) is shown to be essentially undepleted with a slight group-velocity drift.

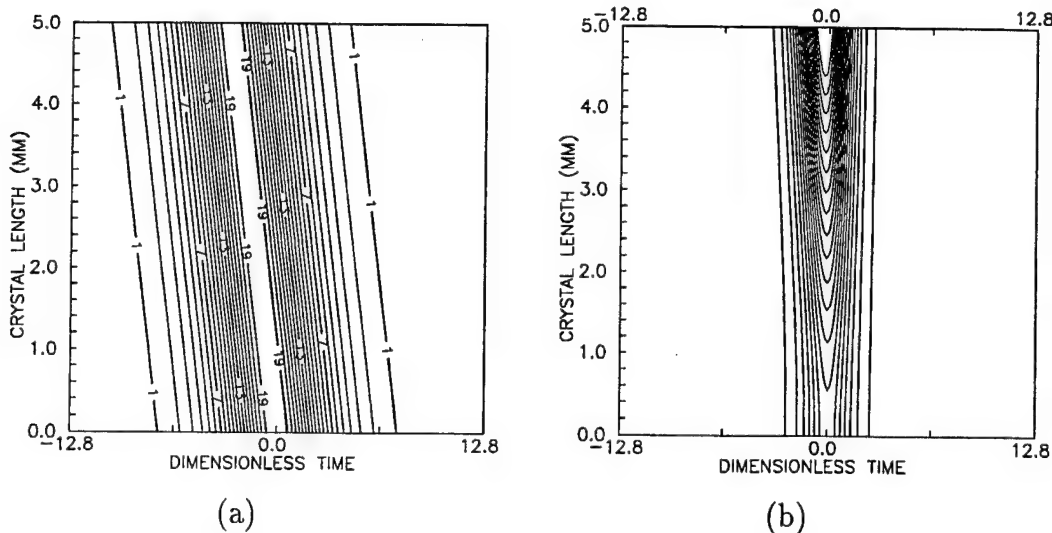


Figure 2.3: Contour plots of the pump and signal-idler fields. The pump field in (a) is shown to exhibit a drift in the group velocity. In (b), the signal-idler fields have a much smaller drift since the pump field is assumed to be much wider in duration than the signal field.

only the dominant terms of the three wave interaction, it is found that

$$\frac{\partial S}{\partial Z} = iBPI^* \quad (2.24a)$$

$$\frac{\partial I}{\partial Z} = iBPS^* \quad (2.24b)$$

$$\frac{\partial P}{\partial Z} = 0, \quad (2.24c)$$

where $B = (\sigma_1 \chi^{(2)} \mathcal{E}_p \zeta_0)$. Eq. (2.24c) explicitly demonstrates the fact that to leading order, the pump field can be considered constant and undepleted. Therefore, the three wave interaction is reduced to solving the coupled set of equations, Eq. (2.24a) and Eq. (2.24b), for the signal and idler fields.

2.4 Jump Conditions

In this section, the solutions of Eq. (2.24a) and (2.24b) are considered. This leading order behavior of the signal and idler fields corresponds to the qualitative

features of a general phase-sensitive amplifier, i.e., the quadratic coupling of the signal (idler) to the complex conjugate of the idler (signal). The solutions for the signal and idler fields can be easily obtained by differentiating Eq. (2.24a) with respect to Z and using Eq. (2.24b) to eliminate the $\partial I^*/\partial Z$ term. In particular, it is found that

$$S(Z, \xi) = S(0, \xi) \cosh \beta Z \quad (2.25a)$$

$$I(Z, \xi) = i(P/|P|)S(0, \xi)^* \sinh \beta Z, \quad (2.25b)$$

where $\beta = B|P|$ is the gain associated with the PSA and it has been assumed that the idler field is initially zero, i.e., $I(0, \xi) = 0$. The assumption concerning the initial amplitude of the idler field clearly stems from the fact that the initial interaction is solely due to the signal and pump fields. The idler field is, in a sense, an artifact of this initial interaction. As mentioned in the previous section, the idler frequency is commensurate with that of the signal field. Therefore, the idler can be considered part of the outgoing signal field at frequency ω_1 . Denoting the total outgoing field at frequency ω_1 by $Q(Z, \xi) = S(Z, \xi) + I(Z, \xi)$, it then becomes apparent upon using Eq. (2.25) that

$$Q(Z, \xi) = Q(0, \xi) \cosh \beta Z + e^{i\phi(Z)} Q^*(0, \xi) \sinh \beta Z, \quad (2.26)$$

where $e^{i\phi(Z)} = iP/|P|$ corresponds to the phase of the pump pulse P . The combined signal-idler field $Q(Z, \xi)$ represents the total gain of the incoming signal field through a section of quadratic $\chi^{(2)}$ material. Eq. (2.26) then can be understood to represent the transfer function or ‘jump’ condition associated with a degenerate optical parametric amplifier. This behavior, which couples the output to the initial amplitude and its complex conjugate, represents the qualitative behavior associated with a phase-sensitive amplifier.

It can be noted at this point that a convenient quadrature decomposition exists which decomposes the effective ‘signal’ pulse into gain and loss components. In particular, the quadrature decomposition

$$Q = [A + i B]e^{i\phi/2} \quad (2.27)$$

will separate the signal pulse into phase-locked A and anti-phase-locked B quadratures which experience exponential gain and exponential attenuation respectively. Note that B in this case is not that given in Eq. (2.24). More will be said about this in upcoming chapters.

2.5 Phase-Mismatch and Bandwidth Considerations in a Fiber PSA

This section is concerned with understanding the bandwidth limitations imposed on the pulse propagation when the effect of phase-mismatch is considered. In essence, the frequency dependence of $\Delta k = \Delta k(\omega)$ is investigated. This is important in understanding whether or not a more physically realizable model for the pulse propagation with PSAs is required in order to understand the qualitative structure given in the preceding section. As was shown in the last two sections, the assumption of perfect phase-matching, i.e., $\Delta k = 0$, considerably simplified the leading order behavior of the phase-sensitive amplifiers. The idea now is to phase-match the center frequency of the propagating pulse with the PSAs. The hope is that the spectral bandwidth of the pulse is much smaller in comparison with the bandwidth of the PSAs so that the phase-mismatch can be neglected.

In particular, phase-matching in a fiber PSA is considered. Briefly, a fiber PSA exploits the fiber nonlinearity in order to provide phase-sensitive gain to a propagating pulse. The fiber amplifier configuration is based upon a Sagnac interferometer [31]. It can be shown that this method behaves to leading order in the same manner as a type I phase-matched $\chi^{(2)}$ PSA where, of course, the appropriate constant associated with the gain is now dependent upon the $\chi^{(3)}$ material. The basic model governing this process is simply [32, 33]

$$\frac{\partial q}{\partial Z} = iD|q|^2q, \quad (2.28)$$

where q represents total field, $D = 3\chi^{(3)}\omega_0/8cnA_{eff}$, A_{eff} is the effective core area of the fiber, and the dispersion and loss are negligible for the length of fiber being

considered. Equation (2.28) has the solution $q(Z) = q(0) \exp(iD|q(0)|^2 Z)$. Upon assuming that the field amplitude is a sum of the pump and signal fields, it can be found that the fiber amplifier acts to leading order in a similar manner to a $\chi^{(2)}$ amplifier. In particular, the effective gain coefficient of the fiber PSA is given by $D_{eff} = \ln(2Dz_a|P|^2)/z_a$ where z_a is the amplifier length. This holds provided the pump field is much larger than the signal field being amplified. Therefore, for the case of phase-matching, the fiber PSA equations once again give the jump condition of Eq. (2.26) where the effective gain coefficient βZ is now given by D_{eff} . Details of this amplifier can be found in Reference [32, 33].

The phase-mismatch for a fiber PSA is given by

$$\Delta k = 2k_3 - k_2 - k_1. \quad (2.29)$$

Consider then the case for which the center-frequency of the propagating pulse is ω_0 . In particular, suppose that the propagating pulse contains spectral components which are not commensurate with ω_0 but are off by ω . Since the frequency of the pump pulse corresponds to the center frequency of the signal pulse, the following relations must hold for the coupled frequency components ω_1 and ω_2 of the propagating pulse and ω_3 of the pump

$$\omega_1 = \omega_0 + \omega \quad (2.30a)$$

$$\omega_2 = \omega_0 - \omega \quad (2.30b)$$

$$\omega_3 = \omega_0. \quad (2.30c)$$

Upon inserting Eq. (2.30) into Eq. (2.29) it is found

$$\Delta k = 2k_3(\omega_0) - k_2(\omega_0 - \omega) - k_1(\omega_0 + \omega), \quad (2.31)$$

where Δk is the phase-mismatch in the fiber PSA. Applying a Taylor expansion to Eq. (2.31) reduces the phase-mismatch to the following

$$\Delta k = -\omega^2 k''(\omega_0). \quad (2.32)$$

Here, use has been made of the fact that the type I phase-matching requires that $k_1(\omega_0) = k_2(\omega_0) = k(\omega_0)$. The value of $k''(\omega_0)$ can be found in standard texts on

nonlinear optical fibers [2, 3]. Note that the characteristic length of a fiber amplifier is approximately 100 m.

It now becomes necessary to investigate the interaction of the frequency components at ω_1 and ω_2 . Previously, the assumption $\Delta k = 0$ was one of the significant simplifications made in deriving the jump condition of Eq. (2.36). This condition allows for a straightforward decomposition of the signal into phase-locked and anti-phase-locked quadrature components. In what is to be considered now, the phase-mismatch is assumed to be zero only for the center frequency of the propagating pulse. Therefore, the phase-mismatch Δk must be incorporated into the nondimensionalized equations (2.24).

In the Fourier domain, the coupling of the frequency components are governed by the following set of equations [1, 26]

$$\frac{\partial \hat{q}(\omega)}{\partial Z} = i\alpha \hat{q}^*(-\omega) e^{i\Delta k(\omega)Z} \quad (2.33a)$$

$$\frac{\partial \hat{q}^*(-\omega)}{\partial Z} = -i\alpha^* \hat{q}(\omega) e^{-i\Delta k(\omega)Z}, \quad (2.33b)$$

where $\hat{q}(\pm\omega)$ represents the spectral component located at $\omega_0 \pm \omega$, α is the gain coefficient which depends on $\chi^{(3)}$, and $\Delta k(\omega)$ is given by Eq. (2.32). Equation (2.33) can be readily solved [1], and it is shown to yield the following

$$Q(Z) = \begin{pmatrix} a & b \\ b^* & a^* \end{pmatrix} Q(0), \quad (2.34)$$

where $Q(Z) = (\hat{q}(\omega) \ \hat{q}^*(-\omega))^T$, $a = (\cosh(gZ) - i(\Delta k/2g) \sinh(gZ)) \exp(i\Delta k/2)$ and $b = i(\alpha/g) \sinh(gZ) \exp(i\Delta k/2)$ with $g = \sqrt{|\alpha|^2 - (\Delta k/2)^2}$. The eigenvalues of the above matrix determine the gain of the pulse as a function of the frequency. In particular, it is found that

$$\lambda_{\pm} = \text{Re}\{a\} \pm \sqrt{\text{Re}\{a\}^2 - 1}, \quad (2.35)$$

where λ_+ corresponds to the gain quadrature of interest.

The gain as a function of the frequency can be more simply understood by studying the real part of the effective gain $g = \sqrt{|\alpha|^2 - (\Delta k/2)^2}$. This gives a good

idea of the bandwidth associated with the fiber PSA. Here, a 100 m section of fiber is considered with values of $k'' = -17, -20$ and $-22 \text{ ps}^2/\text{km}$ for values of $|\alpha|z_a = 1.0$ and $|\alpha|z_a = 1.609$. Note that each of these values for k'' give rise to approximate PSA bandwidths (FWHM) of 2.0 THz, 1.9 THz and 1.8 THz for $|\alpha|z_a = 1.0$ and 2.7 THz, 2.5 THz and 2.4 THz for $|\alpha|z_a = 1.609$. A 200 m fiber PSA can also be considered and is shown to give bandwidths of 1.4 THZ, 1.3 THz and 1.2 THz for $|\alpha|z_a = 1.0$.

It is interesting to further compare the bandwidth of the fiber PSA with the bandwidth of a propagating soliton-like pulse solution. In particular, it will be assumed that the initial characteristic width of a hyperbolic secant pulse is 50 ps. This corresponds to a frequency bandwidth of 11.4 GHz. Figures 2.5a-b depict the bandwidth associated with a 100 m fiber PSA ($k'' = -17 \text{ ps}^2/\text{km}$ and $|\alpha|z_a = 1.0$) along with the frequency bandwidth of the 50 ps hyperbolic secant pulse. Note that the gain is nearly uniform across the entire profile of the pulse. This is seen in more detail from Fig. 2.5b. These figures suggest the possibility that the bandwidth constraints in the regime of 50 ps pulses are negligible. In fact, upon looking more closely at the frequency response, it is found that the edge of the localized pulse experiences a gain difference of $O(10^{-8})$ from the center frequency of the propagating pulse. Therefore, treating the PSAs as frequency independent is an excellent approximation.

2.6 Summary

Through the assumptions and approximations made in the preceding sections, it has been shown that the underlying behavior of the phase-sensitive amplifier in the simplest case is governed by Eq. (2.26). This leading order behavior is a consequence of the asymptotic reduction of the full vector Maxwell's equations in the quadratic medium and the appropriate asymptotic regime. In the following chapters, this leading order behavior of the PSAs will be incorporated into a physically realizable optical communications line (see Figure 2.6). In this case, all of the asymptotic reductions and scalings used to derive the coupled amplitude equations and the simplified behavior given by Eq. (2.26) remain valid. Moreover, since the length scale of the amplifier itself is negligible in comparison with that of the communications line,

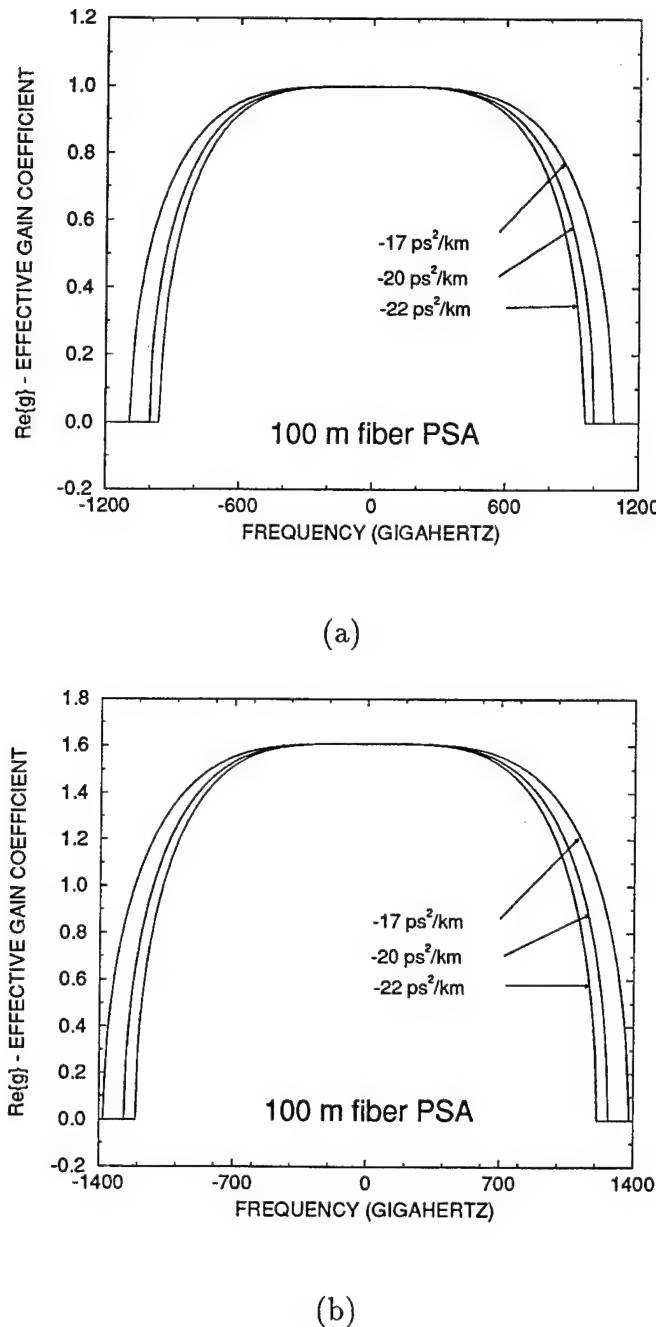
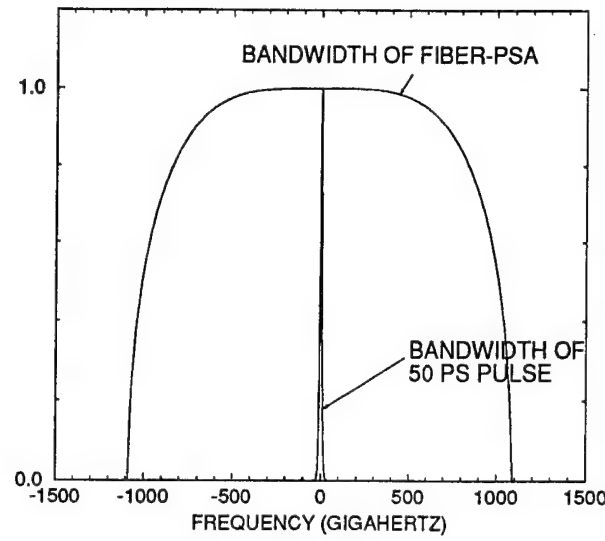
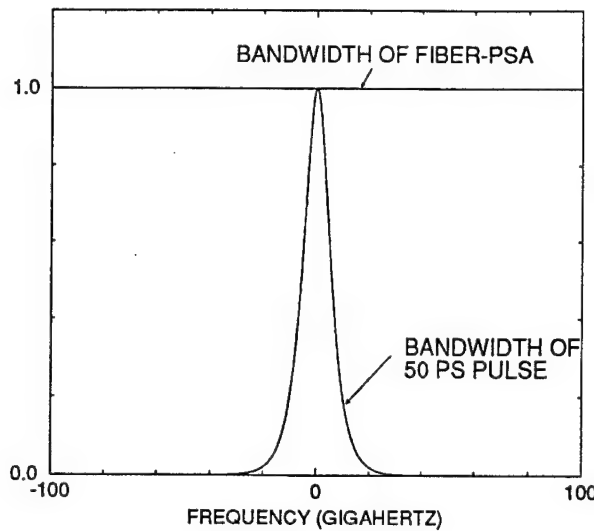


Figure 2.4: In (a) and (b), the effective gain, i.e., $\text{Re}\{g\}$, is plotted as a function of the frequency for $|\alpha|z_a = 1$ ($e^{|\alpha|z_a} = 2.72$) and $|\alpha|z_a = 1.609$ ($e^{|\alpha|z_a} = 5.0$) respectively given $k'' = -17, -20$ and $-22 \text{ ps}^2/\text{km}$.



(a)



(b)

Figure 2.5: Qualitative comparison of the bandwidth of a fiber-PSA ($k'' = -17 \text{ ps}^2/\text{km}$) with a normalized 50 ps (11.4 GHz) pulse. In (a), the pulse spectrum is seen to be extremely narrow in comparison to the PSA bandwidth. In (b), a blown up version depicts the normalized pulse spectrum more clearly.

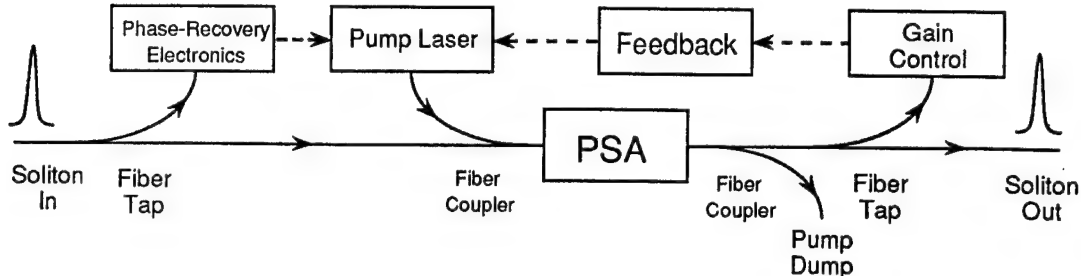


Figure 2.6: A physically realizable PSA employing a degenerate optical parametric amplifier for use in an optical communications line

the amplifiers can be essentially treated as a strongly localized forcing, i.e., a delta function. With this in mind, Eq. (2.26) can be thought of as the appropriate jump condition associated with a phase-sensitive amplifier. In particular, it is found that

$$Q_+ = \cosh \alpha Q_- + e^{i\phi(Z)} \sinh \alpha Q_-^*, \quad (2.36)$$

where Q_{\pm} denotes the signal pulse just before (+) and just after (-) the amplifier. Further, the total gain associated with each amplifier is given by $\alpha = \beta Z_a$ where Z_a is the length of the amplifier and $\beta = B|P|$ as before. Eq. (2.36) therefore describes the qualitative features of a PSA and explicitly demonstrates the phase dependence through the coupling of the signal field to its complex conjugate.

This chapter is concluded by the following general remarks. Although the PSA behavior has been tremendously simplified to give Eq. (2.36), Section 2.5 considered the case for which the phase-mismatch was not zero across the entire signal field profile, i.e., the frequency response of the PSA was investigated. The bandwidth of the PSA was explored for a fiber amplifier, and it was found that the bandwidth limitations have a negligible effect on the amplifier dynamics. Therefore, Eq. (2.36) is in general quite accurate. Moreover, the assumptions considered thus far, which correspond to quasi-monochromatic fields, high-frequency/large-wavenumber and the paraxial waveguide approximation, all remain valid when the PSAs are considered in an optical communications system. Therefore, the PSAs present a realistic candidate for loss compensation in a fiber optic communications line.

Chapter 3

Averaged Pulse Propagation using Phase-Sensitive Amplifiers

3.1 Introduction

It has been well established that the evolution of an optical soliton in a length of fiber which is attenuated by linear loss behaves according to the cubic nonlinear Schrödinger equation (NLS) [3, 4, 7]

$$\frac{\partial q}{\partial z} = -i \frac{k''}{2} \frac{\partial^2 q}{\partial t^2} + i \left(\frac{\omega^2 \chi^{(3)}}{2kc^2} \right) |q|^2 q - \left(\frac{\omega^2 \chi_I}{2kc^2} \right) q. \quad (3.1)$$

Here $k'' = \partial^2 k / \partial \omega^2 < 0$ (anomalous dispersion regime), ω and k denote the angular frequency and wavenumber of a propagating pulse, χ_I represents the imaginary part of the linear response kernel to applied electric field, and $\chi^{(3)}$ is a measure of the nonlinear cubic susceptibility. Note that $q(z, t)$ represents the pulse envelope in the reference frame moving with the group velocity of the propagating pulse. Equation (3.1) can be derived via the same asymptotic reduction used to obtain the envelope equations of Chapter 2 for the phase-sensitive amplifiers. In fact, as was noted in the previous chapter, many of the underlying assumptions used to derive the coupled amplitude equations (2.19) are carried over to the derivation of Eq. (3.1). In particular, a polarization preserving, single-mode fiber is considered for which Maxwell's equations are once again reduced to a simple formulation. Further, the assumptions of high-frequency (large-wavenumber) carrier waves and the paraxial waveguide approximation remain valid within the context of pulse propagation in an optical fiber.

These facts, which are used in conjunction with the disparate length scales of the large propagational distance and small transverse core structure of the fiber provide the natural setting for the asymptotic reduction of Maxwell's equations to a one dimensional wave equation.

The major differences between the derivation of the envelope equations of the phase-sensitive amplifier and the nonlinear Schrödinger equation (3.1) arise due to the material properties and nonlinear response of the medium in question. Fused-silica fiber is a centrosymmetric medium, i.e., fibers display inversion symmetry, and therefore $\chi^{(2)} = 0$. Moreover, the dominant behavior of the cubic nonlinearity neglects the higher harmonics, or nonresonant terms, and is dependent upon the magnitude of the electric field alone. This fact allows the index of refraction to be expressed as a sum of the linear and nonlinear response terms as follows

$$n(\omega, E) = n_0(\omega) + n_2(\omega)|E|^2 \quad (3.2)$$

where $n_2 > 0$. It is clear from Eq. (3.2) that those parts of a propagating pulse which are of larger magnitude experience a higher index of refraction. This fact allows the pulse to experience a self-phase modulation and to retain a highly localized structure upon propagation through a section of dispersion-shifted fiber. If in addition, the dispersion and self-phase modulation are exactly balanced, Eq. (3.1) with $\chi_I = 0$ gives rise to nondispersive soliton solutions which are of the hyperbolic secant form. The hyperbolic secant soliton solution of the NLS can be thought of as the result of a fundamental balance between the linear dispersion and the cubic Kerr nonlinearity.

Prior to discussing the qualitative features associated with solitons, it is helpful to normalize Eq. (3.1) upon the relevant physical scalings of an optical communications line. It is then found that

$$\frac{\partial Q}{\partial Z} = \frac{i}{2} \frac{\partial^2 Q}{\partial^2 T} + i|Q|^2 Q - \gamma Q, \quad (3.3)$$

where Q, Z and T have been normalized on the pulse width t_0 (full-width at half maximum – FWHM) such that

$$Z_0 = \left(\frac{\tau}{1.76} \right)^2 \frac{1}{-k''} \quad (3.4a)$$

$$E_0^2 = \frac{2kc^2}{\chi^3\omega^2} \left(\frac{1.76}{\tau}\right)^2 (-k'') \quad (3.4b)$$

$$\gamma = \delta Z_0, \quad (3.4c)$$

where Z_0 is the dispersion length, E_0 is the peak-field amplitude and $\delta = \omega^2\chi_I/2kc^2$ is a measure of the power loss rate. For a typical dispersion-shifted fiber at a wavelength of $\lambda = 1.55 \mu\text{m}$, for example, $Z_0 = 500 \text{ km}$ for $t_0 = 50 \text{ ps}$ and $\delta = 0.02763 \text{ km}^{-1}$ which gives a total power loss rate of 0.24 dB/km . Recall that $k'' < 0$ so that the optical fiber is operated in the anomalous dispersion regime necessary for soliton propagation. As a final note, the effective transverse structure of the fiber, i.e., its cross section, can be accounted for through the normalization of the peak-field amplitude. This can be more fully understood from considering the relation $n_2 = \chi^3/2\alpha_c n_0$ where α_c is a geometric factor dependent upon the index of refraction profile. This relation can be used in Eq. (3.4) to express the peak-field amplitude in terms of the geometric transverse structure of the fiber. In typical applications, which will be pursued below, $\alpha_c \sim 1/2$.

As noted earlier, Eq. (3.3) with $\gamma = 0$ is known to exhibit a robust set of soliton solutions [11]. In particular, a general single-soliton solution, which can be derived using the inverse scattering transform, can be expressed in the following form

$$Q(Z, T) = 2\eta \operatorname{sech}[2\eta(T - 4\xi Z)] e^{-2i\xi T + 4i(\xi^2 - \eta^2)Z}. \quad (3.5)$$

The parameters η and ξ characterize the soliton; 2η being its amplitude and inverse width and 4ξ its velocity relative to some reference frame. In what will follow, the parameter ξ can be taken to be identically zero without loss of generality, i.e., the NLS can always be transformed so that $\xi = 0$. Associated with the single-soliton solution of Eq. (3.5) is an infinity of conservation laws which arise due to the Hamiltonian structure of the NLS. This completely integrable structure allows the single-soliton solution to be robust to perturbations of the governing NLS equation. In particular, perturbations of the NLS have been shown to modify the hyperbolic secant solution in two ways. First, the soliton parameters, which are constants of the motion for the unperturbed case, can now vary with distance of propagation. In the perturbations

of interest, this variation in the soliton parameters occurs on a length scale which is much longer than the typical evolution, i.e., it can be thought of as adiabatic. The second way in which perturbations effect the soliton solution given by Eq. (3.5) is in the generation of a background radiation field which is superimposed upon the single-soliton solution. Rigorous study of the dispersive radiation field is a nontrivial matter as it can exhibit quite complicated behavior. Numerous studies have been conducted on various perturbations which are of physical interest. And although the dispersive radiation field which is generated exhibits much complicated behavior, the leading order soliton solution, with the appropriate slow evolution of its parameters, has been shown to be robust and stable. Along with its nondispersive behavior, it is this fact which makes solitons ideal candidates for use as bits in long-haul communications systems.

3.2 Formulation

In considering an optical communications system where loss and gain are present, which is the case of interest of this dissertation, the governing NLS must be modified in order to incorporate the effects of periodic amplification and linear loss which are incurred in the pulse propagation (see Fig. 3.1). These modifications involve the addition of appropriate perturbing terms, which are not necessarily small, that can correctly account for the linear attenuation and phase-sensitive gain. In particular, pulse propagation in a length of fiber where linear loss in the fiber is balanced by a chain of periodically spaced phase-sensitive amplifiers is considered. Moreover, the case for which the amplifier spacing Z_l is much less than the soliton period Z_0 , i.e., $Z_l/Z_0 = \epsilon l$ where $\epsilon \ll 1$ and $l \sim O(1)$, is investigated [18, 19]. Given these considerations, the modified pulse evolution can be shown to be governed by,

$$\frac{\partial Q}{\partial Z} = \frac{i}{2} \frac{\partial^2 Q}{\partial^2 T} + i|Q|^2 Q + \frac{1}{\epsilon} \left[-\Gamma Q + h \left(\frac{Z}{\epsilon} \right) Q + e^{i\phi(Z)} f \left(\frac{Z}{\epsilon} \right) Q^* \right], \quad (3.6)$$

where $\Gamma = \delta Z_l/l$ is the linear loss coefficient in the fiber, ϕ is the phase of the pump pulse associated with the PSA, and Q represents the pulse envelope which has been normalized on the soliton period through Eq. (3.4). The $h(Z/\epsilon)$ and $f(Z/\epsilon)$ terms

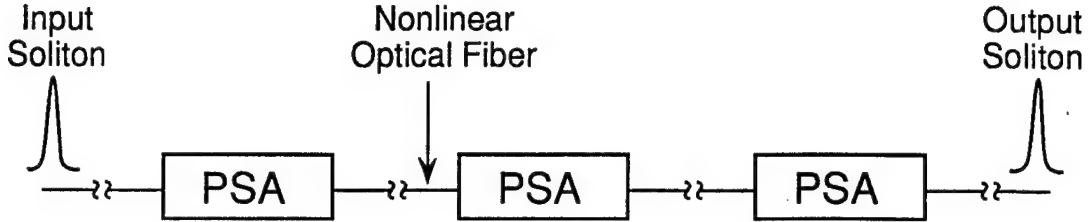


Figure 3.1: Schematic of a nonlinear optical fiber transmission line in which loss is balanced by a chain of periodically-spaced, phase-sensitive amplifiers (PSAs).

represent the periodic gain of the phase-sensitive amplifiers and are given by

$$h(\zeta) = (\cosh \alpha - 1) \sum_{n=1}^N \delta(\zeta - nZ_l) \quad (3.7a)$$

$$f(\zeta) = \sinh \alpha \sum_{n=1}^N \delta(\zeta - nZ_l), \quad (3.7b)$$

where α is the gain coefficient associated with the amplifiers as given in Chapter 2. Because the amplifiers act on a length scale which is essentially negligible in comparison with the remaining length scales of the problem, they can be simply modeled as periodic delta function forcings [18]. Note that the phase-sensitive nature of the amplifiers arises through the coupling to the complex conjugate through the term $\exp(i\phi)f(\zeta)Q^*$. In Eq. (3.6), the nonlinearity and dispersion have been explicitly made small in comparison with the loss and gain terms. This is expected from the characteristic scalings of the problem, i.e., the amplifier spacing is much less than the typical length scale of the soliton evolution. Therefore, the loss and gain can be effectively treated as strong, periodic, and rapidly-varying perturbations to the governing NLS equation. These perturbations can be averaged over, which is done in the next section, in order to determine an effective pulse evolution over distances much longer than that of the soliton period.

If instead, phase-insensitive amplifiers are considered [18], Eq. (3.6) would no longer be coupled to its complex conjugate, i.e., the amplification would no longer be a parametric process and $f(\zeta) = 0$. Further, $h(\zeta)$ would be modified in order to account for the total gain associated with the amplifiers. In this case, averaging

the rapid fluctuations due to the loss and gain gives back the NLS as the effective leading order behavior of the pulse propagation on the characteristic length scale of the soliton period. Through its coupling to the complex conjugate, phase-sensitive amplifiers will be shown to give a strikingly different averaged behavior than that which is normally associated with phase-insensitive amplifiers.

3.3 Quadrature Decomposition

Before averaging Eq. (3.6), it is important to understand the dynamics of the PSAs. In particular, consider the jump conditions across a single amplifier. It was shown in Chapter 2 that the following jump condition applies

$$Q_+ = \cosh \alpha Q_- + e^{i\phi} \sinh \alpha Q_-^* \quad (3.8)$$

where Q_{\pm} indicates the pulse just after (+) and before (-) an amplifier. Again, ϕ represents the phase associated with the pump pulse of the amplifier, and α is the gain coefficient of the amplifier. It can be shown that a natural, or convenient, set of variables exists in which to investigate the pulse dynamics. This idea is motivated from the phase-sensitive nature of the amplifiers being considered, i.e., PSAs exhibit a ‘prefered’ direction of amplification. By decomposing the propagating pulse into two orthogonal quadratures,

$$Q = (A + iB)e^{i\phi/2}, \quad (3.9)$$

the dynamics of the pulse propagation can be separated into those components which are phase-locked and those which are anti-phase-locked with respect to the amplifier. Inserting Eq. (3.9) into Eq. (3.8) gives the following jump conditions for the two quadratures A and B ,

$$A_+ = e^\alpha A_- \quad (3.10a)$$

$$B_+ = e^{-\alpha} B_- \quad (3.10b)$$

The phase-locked quadrature A experiences exponential gain across an amplifier while the anti-phase-locked quadrature B is exponentially attenuated. Therefore, as the

pulse propagates through a chain of amplifiers, the B quadrature will be attenuated by both the amplifiers and the linear loss of the fiber. This quadrature component will then be quickly attenuated after several amplifiers and will not remain an $O(1)$ quantity as the pulse evolves. In contrast, the A quadrature experiences both loss (from the fiber) and gain (from the amplifiers). The idea in the next section will be to balance the loss and gain in the phase-locked quadrature and average over this in order to derive an effective long-distance evolution equation for the pulse propagation.

It will now be made clear how the quadrature decomposition in Eq. (3.8) formulates the pulse propagation in terms of a natural and convenient set of coordinates. Using the quadrature decomposition in Eq. (3.6), i.e., inserting Eq. (3.9) into Eq. (3.6) and collecting real and imaginary parts, gives the following set of coupled equations

$$\frac{\partial A}{\partial Z} + \frac{1}{\epsilon}(\Gamma - h(Z/\epsilon) - f(Z/\epsilon))A = -\frac{1}{2}\frac{\partial^2 B}{\partial T^2} - (A^2 + B^2)B + \frac{\kappa}{2}B \quad (3.11a)$$

$$\frac{\partial B}{\partial Z} + \frac{1}{\epsilon}(\Gamma - h(Z/\epsilon) + f(Z/\epsilon))B = \frac{1}{2}\frac{\partial^2 A}{\partial T^2} + (A^2 + B^2)A - \frac{\kappa}{2}A. \quad (3.11b)$$

Here, the reference phase of each PSA has been assumed to change from one amplifier to next, i.e., $\phi = \phi(Z)$, and specifically, the present analysis assumes the phase rotation of the reference phase to be constant so that $d\phi/dZ = \kappa$. It is clear from Eq. (3.11) that the perturbing terms associated with Q , i.e., the loss and gain, are diagonalized by the quadrature decomposition. This decoupling allows for a relatively straightforward averaging of the phase-locked quadrature A which determines the effective evolution of the pulse propagation. Note that the quadrature decomposition further serves to eliminate the coupling of the propagating pulse to its complex conjugate. In fact, Eqs. (3.11) are now a set of real, coupled equations.

3.4 Multiple-Scale Averaging

It is now appropriate to investigate the pulse dynamics as dictated by Eq. (3.11). The aim of this section will be to average over the rapid fluctuations caused by the loss and gain using a multiple-scale approach. The method of multiple-scales

allows for the separation of relevant physical phenomena which occur on fundamentally different length scales [34]. A multiple-scale approach is a natural consequence of the disparate characteristic length scales involved in the formulation of the problem of interest. From the analysis thus far, it has been assumed that the gain and loss occur on a length scale which is much shorter in comparison to the length scale of the dispersion and nonlinearity, i.e., the soliton period. This fact can be utilized to show the averaged pulse evolution occurs on a length scale which is much longer than that of the soliton period. Therefore define the following characteristic length scales

$$\zeta = Z/\epsilon \quad (3.12a)$$

$$\xi = \epsilon Z, \quad (3.12b)$$

where ζ corresponds to the length scale of the amplifier spacing and ξ will be shown to be the ‘extended’ length scale on which the averaged evolution of the pulse is captured. These length scales separate the rapid fluctuations of the loss and gain from the slow evolution of the envelope which occurs on the longer length scales Z and ξ . It is interesting to note that the multiple-scale expansion is similar in spirit to the Lie transform methods used by Kodama and Hasegawa for the guiding-center soliton [18]. Both methods effectively capture, via averaging, the effective evolution behavior on longer length scales.

As discussed in the previous section, the analysis is formulated in terms of the quadrature variables A and B . Since a multiple-scale analysis is being performed, the quadrature decomposition is now dependent on the new variables ζ and ξ . The quadrature decomposition is then

$$Q = (A(\zeta, Z, \xi, T) + iB(\zeta, Z, \xi, T)) e^{i\phi(Z)/2}, \quad (3.13)$$

where the phase has been assumed to be dependent on the Z -scale only, i.e., $d\phi/dZ = \kappa$. This multiple scale quadrature decomposition modifies the Z derivative of the coupled quadrature equations (3.11). The equations governing the pulse dynamics are then as follows,

$$\frac{\partial A}{\partial \zeta} + (\Gamma - h(\zeta) - f(\zeta)) A = \epsilon \left\{ -\frac{\partial A}{\partial Z} - LB \right\} + \epsilon^2 \left\{ -\frac{\partial A}{\partial \xi} \right\} \quad (3.14a)$$

$$\frac{\partial B}{\partial \zeta} + (\Gamma - h(\zeta) + f(\zeta)) B = \epsilon \left\{ -\frac{\partial B}{\partial Z} + LA \right\}, \quad (3.14b)$$

where the operator L is given by $L = \left(\frac{1}{2} \frac{\partial^2}{\partial T^2} + (A^2 + B^2) - \frac{\kappa}{2} \right)$. As previously noted, the rapid fluctuations which occur on the ζ length scale have been decoupled and diagonalized via the quadrature separation. As will be seen, this allows for a relatively simple averaging of the phase-locked quadrature.

The next step in the analysis, which is clear from the asymptotic orderings given in Eqs. (3.14), is to simply expand the quadratures in powers of ϵ as follows,

$$A = A^0 + \epsilon A^1 + \epsilon^2 A^2 + \dots \quad (3.15a)$$

$$B = B^0 + \epsilon B^1 + \epsilon^2 B^2 + \dots \quad (3.15b)$$

Recall that this allows for the separation of fluctuations which are merely local on the ζ scale from those which contribute to the pulse dynamics on the longer length scales Z and ξ . The perturbation expansion successively captures at each order the dynamics of the pulse propagation on the three distinct length scales ζ , Z and ξ . Note that the appropriate jump conditions across the amplifiers at each order are given by,

$$A^i_+ = e^\alpha A^i_- \quad (3.16a)$$

$$B^i_+ = e^{-\alpha} B^i_-, \quad (3.16b)$$

where $i = 0, 1, 2, \dots$ and α again corresponds to the amplifier gain.

At leading order, the pulse dynamics is found to be governed by the following uncoupled set of equations

$$\frac{\partial A^0}{\partial \zeta} + (\Gamma - h(\zeta) - f(\zeta)) A^0 = 0 \quad (3.17a)$$

$$\frac{\partial B^0}{\partial \zeta} + (\Gamma - h(\zeta) + f(\zeta)) B^0 = 0. \quad (3.17b)$$

Note that in between amplifiers $h(\zeta) = f(\zeta) = 0$. Therefore, when the pulse is between amplifiers, the leading order behavior of both quadratures reduces to trivial first

order differential equations whose solutions exhibit exponential decay. Each quadrature component is therefore attenuated by a factor of $e^{-\Gamma l}$ between amplifiers. The jump conditions given by Eq. (3.16) are now imposed on the leading order solutions and it is found that

$$A^0(l_+) = R(Z, \xi, T) e^{\alpha - \Gamma l} \quad (3.18a)$$

$$B^0(l_+) = P(Z, \xi, T) e^{-\alpha - \Gamma l}. \quad (3.18b)$$

These are the leading order solutions after one pass through an amplifier. After traversing a chain of N such amplifiers, the solutions are similar and are given by $A^0(Nl_+) = R(Z, \xi, T) e^{N(\alpha - \Gamma l)}$ and $B^0(Nl_+) = P(Z, \xi, T) e^{-N(\alpha + \Gamma l)}$. It becomes clear that the leading order solution of the B quadrature decays quickly away to zero after only a few amplifiers due to the attenuation from both the fiber and amplifiers. The leading order solution to the phase-locked quadrature A experiences both loss and gain. These effects can be balanced by imposing periodicity on the leading order solution. The balancing of the loss and gain in the phase-locked quadrature is depicted in Fig. 3.2. This then gives the following relation between the loss and gain coefficients,

$$\alpha = \Gamma l + \epsilon^2 \tilde{\alpha}. \quad (3.19)$$

Here, the loss and gain are balanced to $O(\epsilon^2)$. This allows for slight over or under amplification from the PSAs through the parameter $\tilde{\alpha}$. To summarize the leading order results, the loss and gain have been balanced in the phase-locked quadrature to give a periodic solution in ζ while the anti-phase-locked quadrature is shown to decay quickly to zero and be of higher order, i.e., it exhibits an initial transient behavior and is of $O(\epsilon)$ or higher thereafter.

Proceeding to the next order, $O(\epsilon)$, gives the following coupled set of equations

$$\frac{\partial A^1}{\partial \zeta} + (\Gamma - h(\zeta) - f(\zeta)) A^1 = -\frac{\partial A^0}{\partial Z} \quad (3.20a)$$

$$\frac{\partial B^1}{\partial \zeta} + (\Gamma - h(\zeta) + f(\zeta)) B^1 = L_0 A^0, \quad (3.20b)$$

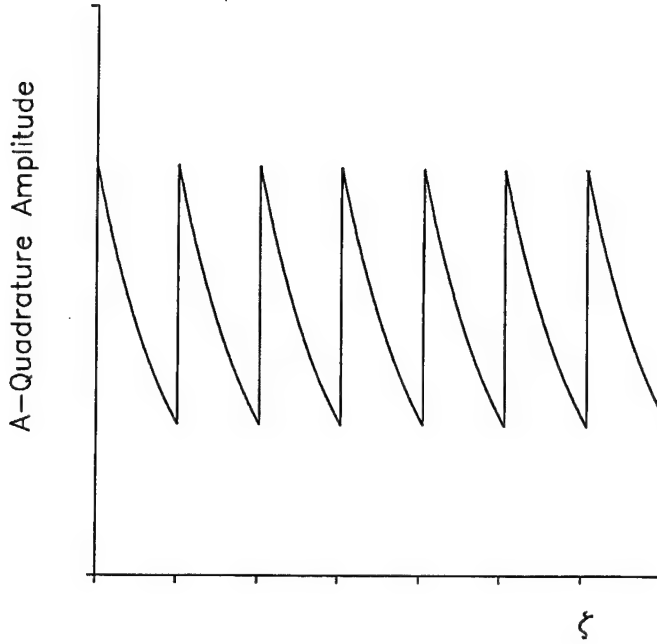


Figure 3.2: Qualitative behavior of the rapid fluctuations which occur in the phase-locked quadrature A on the ζ length scale. Note the balance between the loss and gain over each successive fiber/amplifier segment.

where $L_0 = \left(\frac{1}{2} \frac{\partial^2}{\partial T^2} + (A^0)^2 - \frac{\kappa}{2} \right)$ and the jump conditions of Eq. (3.16) are imposed. It is convenient to study each quadrature equation separately. First, consider the equation for the correction term A^1 . Looking between amplifiers gives a first order differential equation with a periodic forcing $-\partial A^0 / \partial Z$. In order for a solution to exist for A^1 , the forcing $-\partial A^0 / \partial Z$ must be in the range of the homogeneous operator for A^1 . This is equivalent to the forcing being orthogonal to the null space of the adjoint leading order operator for A^0 , i.e., Fredholm's alternative must be satisfied [35]. This solvability condition essentially restricts the solution A^1 to the space of periodic functions and removes any secular growth terms which would lead to unbounded growth. The solvability condition requires that

$$\int_0^l e^{\Gamma\zeta} \left(-\frac{\partial A^0}{\partial Z} \right) d\zeta = 0. \quad (3.21)$$

Using the leading order solution $A_0 = R(Z, \xi, T) e^{-\Gamma\zeta}$ in Eq. (3.21) gives the following

condition for the evolution of the envelope of A^0 ,

$$\frac{\partial R}{\partial Z} = 0. \quad (3.22)$$

Recall that the Z scale corresponds to the typical evolution scale of a soliton, i.e., the length scale of the linear dispersion and nonlinear self-phase modulation. This fundamental result explicitly shows that the PSAs do not allow the pulse to evolve on the soliton period. Rather, the evolution is forced to occur on a fundamentally different length scale than what is normally expected [18]. This is in contrast to the behavior exhibited by phase-insensitive amplifiers for which the averaged evolution occurs on the length scale of the soliton period. The longer length scale ξ will be shown to inherit the slow envelope evolution of the propagating pulse. The suppression of the pulse evolution on the soliton period can be understood from the fact that the PSAs compensate for phase variations experienced by the propagating pulse between amplifiers which are due to the linear dispersion and nonlinear self-phase modulation. In other words, the PSAs work to keep a flat phase profile across the propagating pulse. Since $\partial R/\partial Z = 0$, the equation for A^1 reduces to a simple homogeneous differential equation for which we can take $A^1 \equiv 0$.

The above conclusions can be further supported and understood from solving for the correction term B^1 . Using $A^0 = R(\xi, T)e^{-\Gamma\xi}$ and the appropriate jump condition given by Eq. (3.16b) in Eq. (3.20) gives the following

$$\begin{aligned} B^1 = & \frac{1}{2} \left(\frac{\partial^2 R}{\partial T^2} - \kappa R \right) \zeta e^{-\Gamma\xi} - \frac{1}{2\Gamma} R^3 e^{-3\Gamma\xi} \\ & + \left[\frac{le^{-\alpha}}{4 \sinh \alpha} \left(\frac{\partial^2 R}{\partial T^2} - \kappa R \right) + \frac{l}{\alpha} R^3 e^{-\alpha} \cosh \alpha \right] e^{-\Gamma\xi}. \end{aligned} \quad (3.23)$$

As previously mentioned, the quadrature correction B^1 provides further evidence concerning the attenuation of phase variations of the pulse between amplifiers. By considering B^1 just after an amplifier, it is found that

$$B_+^1 = \frac{le^{-\alpha}}{4 \sinh \alpha} \left(\frac{\partial^2 R}{\partial T^2} - \kappa R \right) + \frac{l}{2\alpha} R^3 e^{-2\alpha}. \quad (3.24)$$

Note that the effects of linear dispersion and nonlinear self-modulation, which correspond to the first and third terms in Eq. (3.24) respectively, are both in the attenuated, anti-phase-locked quadrature of the PSAs. The quadrature separation therefore

shows that the PSAs give rise to a mechanism whereby the attenuation of phase variations of a propagating pulse lead to the suppression of the pulse evolution on the length scale of the soliton period. The averaged evolution is now captured at higher order and shown to evolve on the extended length scale ξ .

Therefore, continuing the perturbation expansion to higher order in the phase-locked quadrature, $O(\epsilon^2)$, gives the following

$$\frac{\partial A^2}{\partial \zeta} + (\Gamma - h(\zeta) - f(\zeta))A^2 = -\frac{\partial A^0}{\partial \xi} + \frac{\tilde{\alpha}}{l}A^0 - L_0B^1. \quad (3.25)$$

The second term on the right hand side of Eq. (3.25), $(\tilde{\alpha}/l)A^0$, comes about from the $O(\epsilon^2)$ deviation from the exact balance of the loss and gain given in Eq. (3.19). Just as in the case of Eq. (3.20), the forcing terms in Eq. (3.25) must satisfy an orthogonality condition in order for a solution to exist, i.e., in order for the solution A^2 to be periodic and contain no secular growth terms. The solvability condition is

$$\int_0^l e^{\Gamma\zeta} \left(-\frac{\partial A^0}{\partial \xi} + \frac{\tilde{\alpha}}{l}A^0 - L_0B^1 \right) d\zeta = 0. \quad (3.26)$$

Notice that the solvability condition gives the evolution of A^0 on the the length scale ξ . Prior to evaluating the integral given by Eq. (3.26), it will be useful to introduce a convenient set of rescalings for the envelope R , the time T , the distance ξ and the overamplification $\tilde{\alpha}$. These rescalings are given as follows

$$U = \left(\frac{1 - e^{-2\Gamma l}}{2\Gamma l \kappa} \right)^{1/2} R \quad (3.27a)$$

$$\tau = \kappa^{1/2} T \quad (3.27b)$$

$$\bar{\xi} = \left(\frac{l}{2} \coth \alpha \right) \xi \quad (3.27c)$$

$$\Delta\alpha = \frac{2}{l^2} \tanh \alpha \frac{\tilde{\alpha}}{\kappa^2}. \quad (3.27d)$$

The rescaling of the envelope amplitude (with $\kappa = 1$) is the same rescaling used when considering soliton propagation with erbium-doped amplifiers, i.e., the guiding-center soliton rescaling [18]. This amplitude rescaling corresponds to normalizing on the average energy of the pulse over one amplifier and fiber segment. The phase rotation

κ is also scaled out by the proper scaling in the amplitude and time. These rescalings along with Eq. (3.26) give the following equation for the pulse evolution

$$\frac{\partial U}{\partial \xi} + \frac{1}{4} \left(\frac{\partial^2}{\partial \tau^2} - 1 \right)^2 U - \Delta\alpha U - U^3 + U^5 + 3\beta U \left(\frac{\partial U}{\partial \tau} \right)^2 + (\beta+1)U^2 \frac{\partial^2 U}{\partial \tau^2} = 0, \quad (3.28)$$

where $\beta = (2 - \tanh \alpha/\alpha)$. Eq. (3.28) is a fourth-order, nonlinear, dissipative equation which governs the pulse dynamics over the long length scale $\bar{\xi}$. Equation (3.28) is the central result of this dissertation and will be the focus of study throughout the remaining chapters.

Upon a careful investigation of Eqs. (3.14), (3.20), and (3.25), it can be understood why the pulse evolution is governed by the fourth-order equation Eq. (3.28). First note that the quadrature correction B^1 , in Eq. (3.20b), is forced by the NLS-type operator $L_0 A^0$ at $O(\epsilon)$. In Eq. (3.25), B^1 in turn forces the phase-locked quadrature at $O(\epsilon^2)$ with the operator $L_0 B^1$. This gives the fourth-order, iterated-NLS type structure governing the pulse evolution as shown in Eq. (3.28). And although the evolution equation inherits much of the structure from the underlying NLS equation, it is important to note that the evolution is of a non-Hamiltonian nature, and therefore, the dynamics will resemble that of dissipative systems.

The central question and concern now is whether the new, averaged evolution equation is capable of supporting stable pulse solutions. In the next two chapters, an investigation is made of the existence and stability of pulse solutions which are governed by Eq. (3.28) in appropriate asymptotic parameter regimes. This is followed by numerical simulations which present evidence of the existence of stable pulse solutions valid for a wide range of parameter values, including physically realizable values of the parameters as applied to soliton based communication systems.

3.5 Summary

It has been the aim of this chapter to investigate the use of phase-sensitive amplifiers as a method for compensating for linear loss in a fiber optic communications line. In particular, the object was to develop a method which would allow

the averaged pulse evolution to be investigated over long distances. The two essential steps in this direction included the quadrature decomposition given by Eq. (3.9) and the averaging via the multiple scales of Eq. (3.12). The quadrature separation was shown to diagonalize the rapidly varying components associated with the loss and gain. Moreover, it allowed the governing equation to be, in a sense, decoupled from its complex conjugate dependence. When the quadrature separation was used in conjunction with the multiple scales, a clear asymptotic ordering resulted which allowed for a straightforward averaging procedure to be carried out. As a result, a fourth-order, nonlinear, dissipative amplitude equation (3.28) was derived which governed the pulse evolution on a length scale much longer than that of the soliton period. The evolution occurs on an extended length scale due to the PSAs attenuation of phase variations across the pulse profile. This averaged equation behaves in a markedly different manner than that of its phase-insensitive counterpart. Whereas the phase-insensitive evolution retains its Hamiltonian structure at leading order, the phase-sensitive amplifiers give rise to a dissipative evolution structure.

As was mentioned in the preceding section, Eq. (3.28) represents a fundamental result of this dissertation. It will be shown in the next chapter that nonlinear, soliton-like pulses can propagate with little or no distortion over long distances in the parameter regime which corresponds to a soliton based communications system, i.e., a regime for which the amplifier spacing is much less than the soliton period. This fact is somewhat surprising in view of the fact that the pulse is continually undergoing $O(1)$ changes in its amplitude as depicted in Figure 3.2. However, this result is consistent with the guiding-center soliton dynamics of phase-insensitive amplifiers. And just as with phase-insensitive amplifiers, the initial power level of the soliton-like pulse is slightly higher than the ideal soliton power. This fact can be understood from the averaging used for both the phase-sensitive and phase-insensitive amplifiers, i.e., the averaged evolution gives rise to a corresponding averaged power which is less than the initial power of the pulse. Therefore, the initial pulse power must be enhanced by the factor $((1 - e^{-2\Gamma l})/2\Gamma l)^{1/2}$ which is given in the rescaling of the pulse amplitude Eq. (3.27a).

The analysis carried out in this chapter for phase-sensitive amplifiers in a

fiber optic line once again attests to the remarkable robustness of solitons under strong perturbations. And although the PSAs break the Hamiltonian structure associated with the NLS, the underlying dynamics of Eq. (3.28) inherits a strong affiliation with the NLS. The relationship between Eq. (3.28) and the NLS will be further explored in the remaining chapters. It will suffice to say at this point that much of the analysis concerning the stability of propagating pulses will rely on the structure of the linearized operator associated with the NLS.

Chapter 4

Existence and Stability of Pulse Solutions

4.1 Introduction

The question which must be addressed at this point concerns the existence of stable pulse solutions governed by Eq. (3.28). In general, the stability and dynamics of pulse solutions of Eq. (3.28) can only be investigated through numerical simulations. However, the aim of the next section is to investigate analytically a parameter regime for which the averaged evolution is simplified via asymptotic and perturbation methods. It is then hoped that the qualitative structure of the results might remain valid outside of the asymptotic regime explored. In particular, a parameter regime is explored, which although unphysical, provides preliminary evidence for the existence of stable pulse solutions. This regime corresponds physically to taking a very small amplifier spacing and overamplification, i.e., $\Gamma l \ll 1$ and $\Delta\alpha \ll 1$, for $U \sim O(1)$. Within this regime, it is reasonable to expect that a stable pulse solution might exist since the amplifiers and loss act as small perturbing terms to the governing NLS equation. Further, it would not be surprising to find the solution to be of the hyperbolic secant type due to the underlying structure and dominance of the NLS. These conjectures follow from what is known of the robust nature of the soliton solutions of the NLS.

In fact, if $\Gamma l = 0$ in Eq. (3.28), then $U = A_{\pm} \operatorname{sech} A_{\pm}\tau$ where $A_{\pm} = \sqrt{1 \pm 2\sqrt{\Delta\alpha}}$. The two solution branches are plotted in Fig. 4.1. It is remarkable

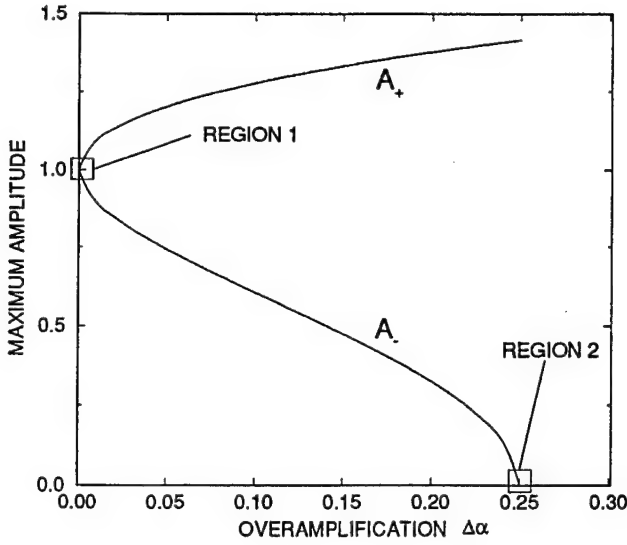


Figure 4.1: Plot of the maximum amplitude for the two solution branches $U = A_{\pm} \operatorname{sech} A_{\pm} \tau$ where $A_{\pm} = (1 \pm 2(\Delta\alpha)^{1/2})^{1/2}$. Region 1 is the asymptotic regime explored in the next section while region 2 is an asymptotic regime explored in the next chapter.

that an exact solution for Eq. (3.28) for $\Gamma l = 0$ is known for all values of $\Delta\alpha$. From this fact and Fig. 4.1, it can be seen that there are two regions which are of analytic interest. Region 1 corresponds to the small amplifier spacing and small overamplification regime mentioned in the preceding paragraph. This region will be explored in Section 4.2. In Section 5.2 of the next chapter, region 2 will be explored by once again making use of asymptotic and perturbation methods. It will be found that a subcritical bifurcation occurs at $(U, \Delta\alpha) = (0, 1/4)$.

Although the results from the asymptotic analysis are valid only for a limited range in parameter space, full numerical simulations will show that in fact the qualitative behavior is preserved for a wide range of parameter space. The results of these numerical simulations will be presented in Section 4.3. Further, the next chapter will explore the bifurcation structure of Eq. (3.28) for a wide range of parameters. In particular, the focus will be in exploring the range of physically realizable parameters

associated with a soliton based communications system. What will be of interest is the range for which the fiber-PSA line supports long-distance pulse propagation.

Before presenting the results of the asymptotic analysis and numerical simulations, some comments concerning the dimensionless parameters are required in order to aid in the understanding of the range of physical values investigated. In the runs that follow it is of interest to note that $\Gamma l = \delta Z_l$ where δ is the linear field amplitude loss rate (e.g., $\delta = 0.02763$ km for a power loss rate of 0.24 dB/km) and Z_l is the amplifier spacing in km. With this definition of Γl in mind and with the aid of Eq. (3.27c), the relevant length scale of propagation can be shown to be given by,

$$\bar{\xi} = \frac{2}{\tanh(\delta Z_l)} \frac{Z_l}{Z_0} Z$$

which gives $\bar{\xi}$ in terms of Z . Recall that Z was the original length scale which was normalized upon the soliton period. Further, the overamplification can be expressed as

$$\alpha = \delta Z_l + \left(\frac{Z_l}{Z_0} \right)^2 \frac{\Delta\alpha}{2 \tanh(\delta Z_l)}$$

which gives the total amplifier gain. Therefore in the remaining numerical simulations, the parameters which will be varied include the amplifier spacing Z_l and the overamplification $\Delta\alpha$ which is given by Eq. (3.27d). These comments apply mainly to Section 4.3 for which physically realizable values of the parameters are considered.

4.2 Pulse Stability for Small Amplifier Spacing

Equation (3.28) is now considered when the amplifier spacing is small. In this case, the close PSA spacing causes very little attenuation of the pulse to occur between amplifiers which in turn requires a correspondingly small amount of phase-sensitive gain. Therefore, the perturbations which modify the governing NLS equation can be thought of as small perturbations to the leading order single-soliton solution. An investigation of this asymptotic regime provides analytic evidence for the existence and stability of a propagating pulse. Although this regime is somewhat unrealistic physically, it is mathematically convenient because a simple, closed form solution of

the hyperbolic secant type is found in this limit. Since the parameter β in Eq. (3.28) is an even functions of Γl , let $\delta = (\Gamma l)^2 \ll 1$ and expand as follows

$$U = U^0 + \delta U^1 + \delta^2 U^2 + \dots \quad (4.1a)$$

$$\Delta\alpha = \delta\alpha^1 + \delta^2\alpha^2 + \dots \quad (4.1b)$$

In addition, define the length scale $\sigma = \delta\bar{\xi}$, and make use of another multiple-scale expansion to capture any slow growth in U caused by the perturbation measured in δ . It will turn out that the slow length scale σ will capture at $O(\delta^2)$ a condition on the overamplification which insures the stability of the leading order solution.

At leading order in δ , $O(1)$, Eq. (3.28) becomes

$$\frac{\partial U^0}{\partial \xi} + \left(\frac{1}{2} \frac{\partial^2}{\partial \tau^2} + (U^0)^2 - \frac{1}{2} \right)^2 U^0 = 0. \quad (4.2)$$

It is easy to show that the hyperbolic secant solution $U_0 = \operatorname{sech} \tau$ satisfies the above steady-state equation. Note that the shape of this pulse agrees with what is expected physically as δ approaches zero — a limit where the fluctuations caused by the attenuation and phase-sensitive amplification are negligible — namely, the hyperbolic secant shape associated with a soliton solution of the nonlinear Schrödinger equation. The structure of Eq. (4.2) is clearly inherited from the underlying NLS equation. This strong connection with the NLS structure will be extensively used to prove the linear stability of the leading order hyperbolic secant solution in the parameter regime being considered.

Before proceeding further in the expansion, it is interesting to note the following properties associated with the fourth-order operator of Eq. (3.28), i.e., $U_{\bar{\xi}} + N(U) = 0$. When expanded in powers of δ using Eqs. (4.1), it is found that

$$\begin{aligned} N(U) &= L_- L_- U^0 + \delta [L_- L_+ U^1 - H_0(U^0, \alpha^1)] \\ &\quad + \delta^2 [L_- L_+ U^2 - H_1(U^0, U^1, \alpha^1, \alpha^2)] + \dots \end{aligned} \quad (4.3)$$

where $L_- L_- U^0$ is a nonlinear operator given in Eq. (4.2) and H_N represents the perturbing terms which force the higher order correction terms U^{N+1} , and

$$L_+ = -\frac{1}{2} \partial_\tau^2 - 3(U^0)^2 + \frac{1}{2} \quad (4.4a)$$

$$L_- = -\frac{1}{2} \partial^2 \tau - (U^0)^2 + \frac{1}{2} \quad (4.4b)$$

are the real and imaginary parts of the linearized operators associated with the NLS equation. The structure and dependence of Eq. (3.28) upon the underlying NLS behavior is made explicitly clear through the leading order and linearized operators $L_- L_-$ and $L_- L_+$ respectively. Fortunately, many properties of the L_+ and L_- operators, both of which are self-adjoint, are well understood [36]. In particular, the spectrum of each operator is known. L_+ contains two discrete modes, one which is at $\lambda = -3$ and the other at $\lambda = 0$, with a continuous spectrum starting at $\lambda = 1$. L_- can be shown to have one discrete spectral component at $\lambda = 0$ with a continuous spectrum also starting at $\lambda = 1$. These characteristic features of the spectra of L_+ and L_- , namely the discrete spectrum and their associated eigenfunctions, are explicitly given in what follows. The discrete zero mode solution of L_- is given by the hyperbolic secant, i.e.,

$$L_-(\operatorname{sech} \tau) = 0.$$

The two discrete modes associated with L_+ are given by

$$L_+(\operatorname{sech} \tau \tanh \tau) = 0$$

$$L_+(\operatorname{sech}^2 \tau) = -3 \operatorname{sech}^2 \tau.$$

Although much is understood concerning the spectra of L_+ and L_- , the spectrum of the linearized operator is what will determine the behavior of the perturbations measured in δ . Therefore, the spectrum of $-L_- L_+$ becomes the key to understanding the pulse stability.

The focus for the remainder of this section will be to investigate the spectral composition of the linearized operator. In particular, it is convenient to separate the spectrum into two distinct categories. In the following Subsection 4.2.1, the zero modes and their corresponding stability are investigated. An analysis pertaining to the remainder of the spectrum follows in Subsection 4.2.2. The reason for this separation becomes clear upon considering the linearized operator $-L_- L_+$. Note that $-L_- L_+$ is a non self-adjoint operator since L_- and L_+ do not commute and

therefore its spectrum is unknown aside from the two zero mode solutions which are investigated in Subsection 4.2.1. As a consequence, the most one can hope for is some kind of bounds upon the remaining spectral components of the linearized operator. In Subsection 4.2.2, it can be shown that the spectrum is bounded away from the origin in the left half plane and therefore, no instabilities can arise due to the remaining spectral components. This will suffice to insure the existence and stability of the leading order hyperbolic secant solution.

4.2.1 Zero Modes of the Linearized Operator and Their Stability

It can be shown that $-L_- L_+$ contains two zero eigenvalues with corresponding eigenmodes given by,

$$\begin{aligned} L_- L_+ (\operatorname{sech} \tau \tanh \tau) &= 0 \\ L_- L_+ (\operatorname{sech} \tau - \tau \tanh \tau \operatorname{sech} \tau) &= 0. \end{aligned}$$

The zero mode solutions of the adjoint linearized operator $-L_+ L_-$, which will be important in determining the appropriate solvability conditions associated with the forcings H_N , can be shown to satisfy,

$$\begin{aligned} L_+ L_- (\operatorname{sech} \tau) &= 0 \\ L_+ L_- (\tau \operatorname{sech} \tau) &= 0. \end{aligned}$$

As will be made clear in what follows, the behavior of the zero modes of the linearized operator and its adjoint are fundamental in understanding the stability of the leading order solution.

Returning now to the perturbation expansion at the next order, $O(\delta)$, it is found that

$$\frac{\partial U^1}{\partial \xi} + L_- L_+ U^1 = H_0(U^0, \alpha^1) = -U^0 \left(\frac{\partial U^0}{\partial \tau} \right)^2 - \frac{1}{3} (U^0)^2 \frac{\partial^2 U^0}{\partial \tau^2} + \alpha^1 U^0. \quad (4.5)$$

Since the homogeneous part of the linear equation for U^1 ,

$$\frac{\partial U^1}{\partial \xi} + L_- L_+ U^1 = 0,$$

has the symbolic solution

$$U^1(\xi) = e^{-\bar{\xi}L_-L_+} U^1(0),$$

it becomes necessary to determine the effects of the perturbation upon the two zero eigenvalues in order to ascertain the stability of Eq. (3.28). As noted earlier, the remainder of the spectrum will be dealt with shortly in Subsection 4.2.2. One of the two zero eigenmodes arises due to the translation invariance of Eq. (4.2), i.e., $\operatorname{sech} \tau \tanh \tau$, and therefore this eigenvalue remains zero under perturbation since Eq. (3.28) is also translationally invariant. The remaining zero mode, $\operatorname{sech} \tau - \tau \tanh \tau \operatorname{sech} \tau$, is affected by the perturbation, however, and the stability of a pulse is determined by this single eigenvalue provided once again that the rest of the spectrum does not give rise to any instabilities.

Since Eq. (4.5) has homogeneous solutions, solvability conditions are required in order for a solution of the perturbed problem to exist [35]. It is necessary that the forcing, H_0 , be orthogonal to the null space of the adjoint linearized operator. A condition is therefore associated with each of the zero eigenmodes. These are as follows,

$$(H_0, \operatorname{sech} \tau) = 0 \quad (4.6a)$$

$$(H_0, \tau \operatorname{sech} \tau) = 0, \quad (4.6b)$$

where $(h, g) = \int_{-\infty}^{\infty} hg d\tau$ denotes the inner product with respect to τ . Note that in the case of interest, both h and g are real and complex conjugation is not necessary in the definition of the inner product. Upon forcing the right hand side of Eq. (4.5) to satisfy the above orthogonality relations, it is found that the first condition, Eq. (4.6a), is automatically satisfied, but the second condition, Eq. (4.6b), is only satisfied if $\alpha^1 = 0$. With $\alpha^1 = 0$, the following solution is obtained for U^1

$$U^1 = -(1/6) \operatorname{sech} \tau + h(\sigma)(\operatorname{sech} \tau - \tau \tanh \tau \operatorname{sech} \tau), \quad (4.7)$$

where $h(\sigma)$ is arbitrary at this order.

At the second order, $O(\delta^2)$, the situation is similar, in that a forced (inhomogeneous) equation is obtained which can only be solved if the orthogonality conditions of Eqs. (4.6) are satisfied. However, H_0 is now replaced by the appropriate forcing H_1 associated with the second order equation, i.e., $(H_1, \operatorname{sech} \tau) = (H_1, \tau \operatorname{sech} \tau) = 0$ where H_1 is given by the following

$$\begin{aligned} H_1 = & -\alpha_2 U^0 - \frac{\partial U^1}{\partial \sigma} + 3U^0(U^1)^2 - 10(U^0)^3(U^1)^2 - 3U^0 \left(\frac{\partial U^1}{\partial \tau} \right)^2 - 6 \frac{\partial U^0}{\partial \tau} \frac{\partial U^1}{\partial \tau} U^1 \\ & - 2(U^1)^2 \frac{\partial^2 U^0}{\partial \tau^2} - 4U^0 U^1 \frac{\partial^2 U^1}{\partial \tau^2} - 2U^0 \frac{\partial U^0}{\partial \tau} \frac{\partial U^1}{\partial \tau} - \left(\frac{\partial U^0}{\partial \tau} \right)^2 U^1 \\ & - \frac{1}{3}(U^0)^2 \frac{\partial^2 U^1}{\partial \tau^2} - \frac{2}{3}U^0 U^1 \frac{\partial^2 U^0}{\partial \tau^2} + \frac{2}{5}U^0 \left(\frac{\partial U^0}{\partial \tau} \right)^2 + \frac{2}{15}(U^0)^2 \frac{\partial^2 U^0}{\partial \tau^2}. \end{aligned} \quad (4.8)$$

Solvability determines $h(\sigma)$ by producing the equation

$$\frac{dh}{d\sigma} = (2\alpha_2 - 2h^2 + \frac{8}{9}h - \frac{16}{135}). \quad (4.9)$$

It is straightforward to show that a steady-state solution of Eq. (4.9) exists and is stable provided $\alpha_2 > (4/405)$, or equivalently, $\Delta\alpha > (4/405)(\Gamma l)^4 \equiv \Delta\alpha_c$ (when Γl is small). Therefore, when this condition is satisfied, the above analysis implies that a stable steady-state pulse solution of Eq. (3.28) should exist provided, of course, the remainder of the spectrum contains no components which give rise to instability.

The critical value $\Delta\alpha_c$ determines the minimum amount of overamplification necessary for stable pulse solutions to occur. The need for a small amount of overamplification is consistent with the use of PSAs. As was noted in Chapter 2, there is a small amount of decay due to ‘losses’ in the anti-phase-locked quadrature. These ‘losses’ are actually due to the sum-frequency generation which occurs when a small portion of the signal field is converted into the pump field at twice the frequency. This process is depicted in Fig. 2.1b. For values of $\Delta\alpha$ below $\Delta\alpha_c$, it is expected that a pulse decays to zero. Of course, these results are only valid when Γl is small, but they are nonetheless indicative of the results obtained using numerical simulations for values of $\Gamma l \sim O(1)$.

4.2.2 Spectral Estimates for the Linearized Operator when Excluding the Zero Modes

Although the two zero modes of the spectrum of $-L_- L_+$ have been determined, the remainder of the spectrum of this non self-adjoint operator remains unknown. And since the linearized operator determines the stability of the leading order solution, the spectrum of $-L_- L_+$ must be further investigated. This subsection will show that the spectrum of $-L_- L_+$ is bounded to the left of the origin with the exception of the two zero modes which were previously determined in Subsection 4.2.1. This result will be shown to imply the exponential stability of the leading order hyperbolic secant solution provided a minimum amount of overamplification is supplied. Note that the spectrum being bounded to the left of the origin represents modes which decay and are stable. This result, in conjunction with those of the previous subsection, demonstrate the existence of stable hyperbolic secant pulse solutions.

It now remains to be shown that the remainder of the spectrum of the $-L_- L_+$ operator is bounded to the left of the origin. This is equivalent to showing that perturbations to the leading order hyperbolic secant solution of Eq. (4.5) are attenuated as ξ gets large, i.e., there are no spectral components which give rise to an instability. The question of stability is then completely understood within the framework of the behavior of the linearized perturbation U^1 which satisfies

$$\frac{\partial U^1}{\partial \xi} = -L_- L_+ U^1. \quad (4.10)$$

It has already been shown that two zero modes exist for the operator $-L_- L_+$. Further, the stability properties corresponding to these modes have been investigated. In order to determine the remaining spectral components, U^1 is confined to the space which is orthogonal to the two adjoint zero modes of $-L_- L_+$. Therefore, the two zero modes of $-L_+ L_-$ are projected out as follows

$$(U^1, \operatorname{sech} \tau) = 0 \quad (4.11a)$$

$$(U^1, \tau \operatorname{sech} \tau) = 0. \quad (4.11b)$$

This then imposes two constraints on the evolution of U^1 and effectively removes the two zero modes associated with the previous stability analysis.

The approach used to determine the stability of $U^1 = 0$ is Liapunov's direct method [37]. The idea is to define a positive definite quantity which is somehow associated with the 'energy' of the problem and to show this 'energy' is monotonically decreasing in 'time' (here 'time' represents $\bar{\xi}$). In particular, the following Liapunov function V is defined

$$V = V(U^1) = (U^1, L_+ U^1). \quad (4.12)$$

Weinstein [36] shows that subject to the constraints given in Eqs. (4.11), the following inequalities hold for the Liapunov function defined in Eq. (4.12)

$$(U^1, L_+ U^1) \geq C_1 \|U^1\|, \quad (4.13)$$

where $\|U^1\| = (U^1, U^1)$ and C_1 is a positive constant. This result clearly indicates that the Liapunov function V or 'energy' is a positive definite quantity.

Using the definition of V given by Eq. (4.12) in conjunction with Eq. (4.10), the following property can be shown to hold

$$V'(U^1(\bar{\xi})) = -2(U^1, L_+ L_- L_+ U^1), \quad (4.14)$$

where $\tau = d/d\bar{\xi}$ and use has been made of the fact L_+ , L_- , and $L_+ L_- L_+$ are all self-adjoint operators. As with all Liapunov functions, the rate of increase or decrease of the 'energy' will be crucial in determining stability. Therefore, it becomes necessary to understand some properties of the inner product $(U^1, L_+ L_- L_+ U^1)$. Since L_+ is a self-adjoint operator, the following can be shown to hold

$$(U^1, L_+ L_- L_+ U^1) = (W, L_- W), \quad (4.15)$$

where $W = L_+ U^1$. Upon using the constraint given by Eq. (4.11a) and the fact that $U^1 = L_+^{-1} W$, a constraint for W can be derived from $(U^1, \operatorname{sech} \tau) = (L_+^{-1} W, \operatorname{sech} \tau) = (W, L_+^{-1} \operatorname{sech} \tau) = 0$. It is not difficult to show that the self-adjoint inverse operator for L_+ acting on a hyperbolic secant solution gives $L_+^{-1} \operatorname{sech} \tau = 1/2(\tau \operatorname{sech} \tau \tanh \tau -$

$\operatorname{sech} \tau$) where the arbitrary $\operatorname{sech} \tau \tanh \tau$ factor has been neglected. This then imposes the following constraint on W ,

$$(W, \tau \operatorname{sech} \tau \tanh \tau - \operatorname{sech} \tau) = 0. \quad (4.16)$$

But Weinstein [36] also shows that

$$(W, L_- W) \geq C_2(W, W) \quad (4.17)$$

subject to the constraint of Eq. (4.16). Written in terms of the original variable U^1 , the following inequalities then hold

$$(U^1, L_+ L_- L_+ U^1) \geq C_2(L_+ U^1, L_+ U^1) = C_2(U^1, L_+^2 U^1) \quad (4.18)$$

where C_2 is some positive constant.

Investigation of an associated Lagrange multiplier problem for $(U^1, L_+^2 U^1)$ provides one further inequality which can be shown to hold. These details will be presented towards the end of this subsection. For the present, the result will simply be stated as follows,

$$(U^1, L_+^2 U^1) \geq C_3(U^1, L_+ U^1), \quad (4.19)$$

where C_3 is some positive constant. Making use of the inequalities given by Eqs. (4.18) and (4.19) implies the following relation

$$V' \leq -2C_2 C_3 V, \quad (4.20)$$

upon using Eq. (4.12) and Eq. (4.14). Therefore, the ‘energy’ decreases monotonically since V' is a negative definite quantity. From Eq. (4.20) it can be shown that the Liapunov function, and hence the linear perturbation U^1 , decays to zero exponentially in $\bar{\xi}$ with some bound on the exponential decay rate. In particular, by integrating Eq. (4.20) directly, it is found that

$$V(U^1(\bar{\xi})) \leq V(U^1(0)) e^{-2C_2 C_3 \bar{\xi}}. \quad (4.21)$$

And upon using Eq. (4.13), the following is found to hold

$$\|U^1\| \leq \frac{V(U^1(0))}{C_1} e^{-2C_2 C_3 \bar{\xi}}. \quad (4.22)$$

Therefore, $U^1 \rightarrow 0$ as $\bar{\xi} \rightarrow 0$ at an exponential rate equal to or faster than $2C_2C_3$ for any given initial condition $V(U^1(0))$.

The preceding result hinges on the inequality given in Eq. (4.19) which was stated without proof. Therefore, it now remains to be shown that

$$(U^1, L_+^2 U^1) \geq C_3(U^1, L_+ U^1).$$

Specifically, it was this condition that gave rise to the inequality of Eq. (4.20) which by integration implied the exponential stability of the leading order hyperbolic secant solution. Therefore, the following problem is considered

$$\text{minimize } (U^1, L_+^2 U^1),$$

subject to the constraints

$$(U^1, L_+ U^1) = 1 \quad (4.23a)$$

$$(U^1, \operatorname{sech} \tau) = 0 \quad (4.23b)$$

$$(U^1, \tau \operatorname{sech} \tau) = 0. \quad (4.23c)$$

It is clear that $(U^1, L_+^2 U^1)$ is non-negative. Now, for what follows define $\alpha = \min (U^1, L_+^2 U^1)$. As in the work of Weinstein [36], the object is to assume that the minimum is zero, i.e., $\alpha = 0$, and show that this gives rise to a contradiction. First however, it is necessary to prove that a zero minimum is indeed attained by a function in a proper admissible class. This will be done shortly. For the present, however, the aim will be to show that $\alpha = 0$ gives rise to a contradiction.

The contradiction regarding the minimum follows in a relatively straightforward manner by considering the following Lagrange multiplier problem associated with the constrained minimization above, i.e.,

$$L_+^2 U^1 = \lambda L_+ U^1 + \beta \operatorname{sech} \tau + \gamma \tau \operatorname{sech} \tau, \quad (4.24)$$

subject to the constraints given by Eq. (4.23). Taking the inner product of this equation with respect to the zero mode of L_+ , $\operatorname{sech} \tau \tanh \tau$, gives immediately $\gamma = 0$. Inverting, i.e., multiplying through by L_+^{-1} , gives

$$L_+ U^1 = \lambda U^1 - \frac{\beta}{2} (\operatorname{sech} \tau - \tau \operatorname{sech} \tau \tanh \tau) + \delta \operatorname{sech} \tau \tanh \tau. \quad (4.25)$$

Taking the inner product again with respect to $\operatorname{sech} \tau \tanh \tau$ gives $\delta = 0$ since the minimum at zero implies $\lambda = 0$. Upon inverting once more, it is found that

$$U^1 = -\frac{\beta}{2} L_+^{-1}(\operatorname{sech} \tau - \tau \operatorname{sech} \tau \tanh \tau) + \omega \operatorname{sech} \tau \tanh \tau. \quad (4.26)$$

The constraint $(U^1, \tau \operatorname{sech} \tau)$ applied to the above equation forces $\omega = 0$ and further implies that U^1 must be an even function in τ . Taking the inner product now with respect to $\operatorname{sech} \tau$ gives

$$(\operatorname{sech} \tau, U^1) = -\frac{\beta}{2} (\operatorname{sech} \tau, L_+^{-1}(\operatorname{sech} \tau - \tau \operatorname{sech} \tau \tanh \tau)). \quad (4.27)$$

The remaining constraint on U^1 , namely $(U^1, \operatorname{sech} \tau) = 0$, must now be satisfied. Since L_+^{-1} is self-adjoint and $L_+^{-1} \operatorname{sech} \tau = \operatorname{sech} \tau - \tau \operatorname{sech} \tau \tanh \tau$, the above equation can be written as

$$(\operatorname{sech} \tau, U^1) = -\frac{\beta}{2} \|\operatorname{sech} \tau - \tau \operatorname{sech} \tau \tanh \tau\| = 0. \quad (4.28)$$

This can only be satisfied for $\beta = 0$. Therefore, since $\beta = \gamma = \delta = \omega = 0$, no solution exists for $\lambda = 0$ and assuming that the minimum occurs at zero leads to a contradiction. As a consequence, the minimum must occur at some positive value, i.e., $\alpha > 0$ and $(U^1, L_+^2 U^1) \geq C_3(U^1, L_+ U^1)$, where C_3 is some positive constant.

The preceding Lagrange multiplier problem assumed the zero solution to be attained. The focus now will be to show that this is indeed true. In particular, it is necessary to show that if $\lambda = 0$, the minimum is attained in the admissible class. This fact is required in order validate the contradiction in the previous analysis of the associated Lagrange multiplier problem.

Therefore, define $\{f_\nu\}$ to be a minimizing sequence, i.e., $(f_\nu, L_+ f_\nu) = 1$, $(f_\nu, L_+^2 f_\nu) \downarrow 0$ and $(f_\nu, \operatorname{sech} \tau) = (f_\nu, \tau \operatorname{sech} \tau) = 0$. The condition on the norm,

$$(f_\nu, L_+ f_\nu) = \frac{1}{2} \int_{-\infty}^{\infty} \left[f_\nu^2 + \left(\frac{\partial f_\nu}{\partial \tau} \right)^2 - 6(U^0)^2 f_\nu^2 \right] d\tau = 1 \quad (4.29)$$

implies that $\|f_\nu\|_{H^1}$ and $\|f_\nu\|_2$ are both bounded since Eq. (4.13) with f_ν holds. Here $\|g\|_{H^n} = \int_{-\infty}^{\infty} (g^2 + (\partial_\tau g)^2 + \dots + (\partial^n \tau g)^2) d\tau$ and the cases $n = 0, 1$ correspond to

the standard L_2 and H^1 Sobolov norms respectively. With this mind, consider the following,

$$(f_\nu, L_+^2 f_\nu) = \int_{-\infty}^{\infty} [(\Delta f_\nu)^2 + 2(\nabla f_\nu)^2 + f_\nu^2 + 9(U^0)^4 f_\nu^2 - 6(U^0)^2 f_\nu^2 - 6(U^0)^2 (\nabla f_\nu)^2] d\tau \quad (4.30)$$

where $\Delta = \partial_\tau^2$ and $\nabla = \partial_\tau$. Then for any $\eta > 0$, we can choose f_ν such that

$$\begin{aligned} 0 &< \int_{-\infty}^{\infty} [(\Delta f_\nu)^2 + 2(\nabla f_\nu)^2 + f_\nu^2 + 9(U^0)^4 f_\nu^2] d\tau \\ &\leq \int_{-\infty}^{\infty} [6(U^0)^2 f_\nu^2 + 6(U^0)^2 (\nabla f_\nu)^2] d\tau + \eta \end{aligned} \quad (4.31)$$

which in turn gives

$$0 < \int_{-\infty}^{\infty} [(\Delta f_\nu)^2 + (\nabla f_\nu)^2 + f_\nu^2] d\tau \leq 6 \int_{-\infty}^{\infty} (U^0)^2 [(f_\nu^2 + (\nabla f_\nu)^2)] d\tau + \eta. \quad (4.32)$$

Since $(f_\nu, L_+ f_\nu) = 1$ implies that $\|f_\nu\|_{H^1}$ is bounded, this in turn implies, upon using Eq. (4.32), that $\|f_\nu\|_{H^2}$ is uniformly bounded. Thus a subsequence f_ν exists that converges weakly to some H^2 function f_* . And by weak convergence, f_* satisfies the orthogonality relations given above. Further, it should follow as in Weinstein that $\int (U^0)^2 (f_\nu^2 + (\nabla f_\nu)^2) d\tau \rightarrow \int (U^0)^2 (f_*^2 + (\nabla f_*)^2) d\tau$ by Hölder's inequality, interpolation and the uniform decay of R . This further implies $\int (U^0)^4 f_\nu^2 d\tau \rightarrow \int (U^0)^4 f_*^2 d\tau$. It can then be concluded that $f_* \neq 0$ by Eq. (4.32) since η is arbitrary.

Thus far, statements concerning the last three terms of Eq. (4.30) have been made. Before we are able to show that the minimum is attained at f_* , the first three terms in Eq. (4.30) must be considered. By Fatou's lemma, the following holds for the third term

$$\|f_*\|_2 \leq \liminf_{\nu \rightarrow \infty} \|f_\nu\|_2. \quad (4.33)$$

It should be further possible to use arguments similar to Weinstein to say something concerning the remaining two terms in Eq. (4.30). First, let $\zeta \in L^2$ with $\|\zeta\|_2 = 1$. By weak convergence of f_ν to f_* , it follows that

$$(\zeta, \nabla f_*) = \liminf_{\nu \rightarrow \infty} (\zeta, \nabla f_\nu) \leq \liminf_{\nu \rightarrow \infty} \|\nabla f_\nu\|_2. \quad (4.34)$$

Maximizing over all such ζ , it is found that $\|\nabla f_*\|_2 \leq \lim_{\nu \rightarrow \infty} \inf \|\nabla f_\nu\|_2$. In a similar manner, let $\xi \in L^2$ with $\|\xi\|_2 = 1$. By weak convergence of f_ν to f_* , it again follows that

$$(\xi, \Delta f_*) = \liminf_{\nu \rightarrow \infty} (\xi, \Delta f_\nu) \leq \liminf_{\nu \rightarrow \infty} \|\Delta f_\nu\|_2. \quad (4.35)$$

Maximizing over all such ξ , it is found that $\|\Delta f_*\|_2 \leq \lim_{\nu \rightarrow \infty} \inf \|\Delta f_\nu\|_2$.

Combining all of the above results and using them in Eq. (4.30) gives the following

$$(f_*, L_+^2 f_*) \leq \liminf_{\nu \rightarrow \infty} (f_\nu, L_+^2 f_\nu) = 0. \quad (4.36)$$

This implies $(f_*, L_+^2 f_*) \leq 0$. But from what is known of the spectrum of L_+ , i.e., it is non-negative, it follows that

$$(f_*, L_+^2 f_*) = 0. \quad (4.37)$$

Therefore, the minimum is attained in the admissible class provided it can be shown that the weighted norm, with respect to L_+ , of Eq. (4.23a) is equal to unity. By Fatou's lemma, the fact that $\|\nabla f_*\|_2 \leq \lim_{\nu \rightarrow \infty} \inf \|\nabla f_\nu\|_2$, and $\int (U^0)^2 f_\nu^2 d\tau \rightarrow \int (U^0)^2 f_*^2 d\tau$, it is found that

$$(f_*, L_+ f_*) \leq \liminf_{\nu \rightarrow \infty} (f_\nu, L_+ f_\nu) = 1. \quad (4.38)$$

Now suppose $(f_*, L_+ f_*) < 1$, then define $g_* = f_*/(f_*, L_+ f_*)^{1/2}$ which is admissible. Then $(g_*, L_+ g_*) = 1$ with $(g_*, L_+^2 g_*) = 0$. Therefore, the minimum is indeed attained at zero with the condition on the norm being satisfied.

To recapitulate, the stability of the linearized perturbation was considered in the context of Liapunov's direct method. In particular, a positive definite Liapunov function V was considered whose derivative with respect to the 'time' variable, V' , was shown to be negative definite. This was shown by considering an associated Lagrange multiplier problem which was constrained to the space of functions for which the zero modes were projected out. Specifically, a contradiction was reached, provided the solution was in the admissible class, which forced V' to be negative definite and the leading order solution to be asymptotically (exponentially) stable.

The foregoing analysis implies that the spectrum of $-L_- L_+$ contains two zero modes with all other modes being bounded to the left of the origin. Therefore,

the stability of the leading order hyperbolic secant solution is entirely determined from the previous analysis on the two zero modes of Section 4.2.1. In particular, the leading order hyperbolic secant solution is exponentially stable for $\Delta\alpha > (4/405)(\Gamma l)^4 \equiv \Delta\alpha_c$.

In contrast with erbium-doped communications systems [18, 19], initial perturbations of the propagating pulse solution using PSAs exponentially approach the stable, steady-state, leading order solution without the shedding of a background radiation field. This behavior is indicative of the fact that the phase-sensitive amplifiers break the Hamiltonian structure of the underlying nonlinear Schrödinger equation. In contrast, an erbium-doped fiber amplifier system preserves, to leading order, the Hamiltonian structure associated with the NLS which allows initial perturbations of the propagating pulse to generate both shifts in the soliton parameters and a background radiation field. Both systems, however, generate a small background radiation field from the periodic forcing of the loss and gain.

4.3 Pulse Stability for Amplifier Spacing of $O(1)$

In the previous section, the stability of a steady-state pulse solution is shown to exist for $\Gamma l \ll 1$. For physically realizable values of the amplifier gain, fiber loss and dispersion length, the assumption that Γl is much less than unity no longer holds. This section considers the stability and evolution of propagating pulses when $\Gamma l \sim O(1)$. Numerical simulations provide the most direct and efficient method for studying this parameter regime in which asymptotic results of the previous sections fail to hold. In what follows, stable pulse solutions will be shown to exist and act as attractors for a wide range of initial conditions and parameter values. Further, the averaged evolution and the full NLS numerics will be compared in order to determine the validity and accuracy of the effective evolution given by Eq. (3.28).

The numerical method used in solving Eq. (3.28) utilizes a fourth-order Runge-Kutta method in time and filtered pseudo-spectral method in space [38]. The method combines the advantages of split-step [7, 39, 3] and explicit Runge-Kutta methods [40] and gives a relatively simple fourth-order scheme with improved numerical stability properties. The computational region in all of the runs was taken to be

larger than the region of interest and an absorbing boundary layer was implemented to eliminate any reflections from the edges of the computational domain. Numerical results were carefully checked by varying the number of Fourier modes, the time step and the size of the computational domain. The remainder of this section will focus on presenting the numerical results obtained from solving Eq (3.28).

To begin, Fig. 4.2 shows two representative numerical solutions of Eq. (3.28). Figure 4.2a is for an initial pulse $U(\tau, 0) = \text{sech } \tau$ and Fig. 4.2b for $U(\tau, 0) = 1.8 \text{ sech } \tau$. In both cases the solution exponentially approaches a stable steady state as it evolves. Further evidence concerning the asymptotic, exponential stability of the steady-states for Eq. (3.28) is provided by Fig. 4.3 in which various initial amplitudes are shown to decay onto the final steady-state amplitude. The parameters used in these simulations are $\Gamma l = 1$ (which corresponds to an amplifier spacing of roughly 36 km), $\kappa = 1$, and $\Delta\alpha = 0.1$. As was noted in the stability analysis of the previous section, positive values of $\Delta\alpha$ (i.e., overamplification) are necessary to obtain the stable pulse solutions. In these simulations, the pulses propagate 10 units in the long length scale $\bar{\xi}$.

Figure 4.4 reflects the fact that a wide range of initial pulse amplitudes and widths are capable of producing stable pulse solutions. This figure was made by simply solving Eq. (3.28) for many different initial pulses of the form $U(\tau, 0) = A \text{ sech}(\tau/\tau_0)$ with different values of A and τ_0 and noting the cases for which the stable steady-state pulse solution was reached. Note that all initial pulses within the shaded region asymptote to the same stable steady-state which is approximately given by $2 \text{ sech}(\tau/1.5)$. The numerical simulations were carried out using the same parameter values as in Fig. 4.2, i.e., $\Gamma l = 1$, $\kappa = 1$, and $\Delta\alpha = 0.1$. Similar numerical simulations indicate that stable pulse solutions are obtained for a wide range of Γl , which correspond to a variety of physically realizable amplifier spacings.

In Fig. 4.5, the steady-state pulse profiles that are obtained by solving Eq. (3.28) for different values of overamplification, $\Delta\alpha$, are depicted. Note that for larger values of overamplification small wings develop in the pulse's characteristic profile. This behavior is similar to what is observed when phase-sensitive amplifiers are used in linear systems (a fiber/PSA line in which the nonlinearity plays no role). [41, 32]

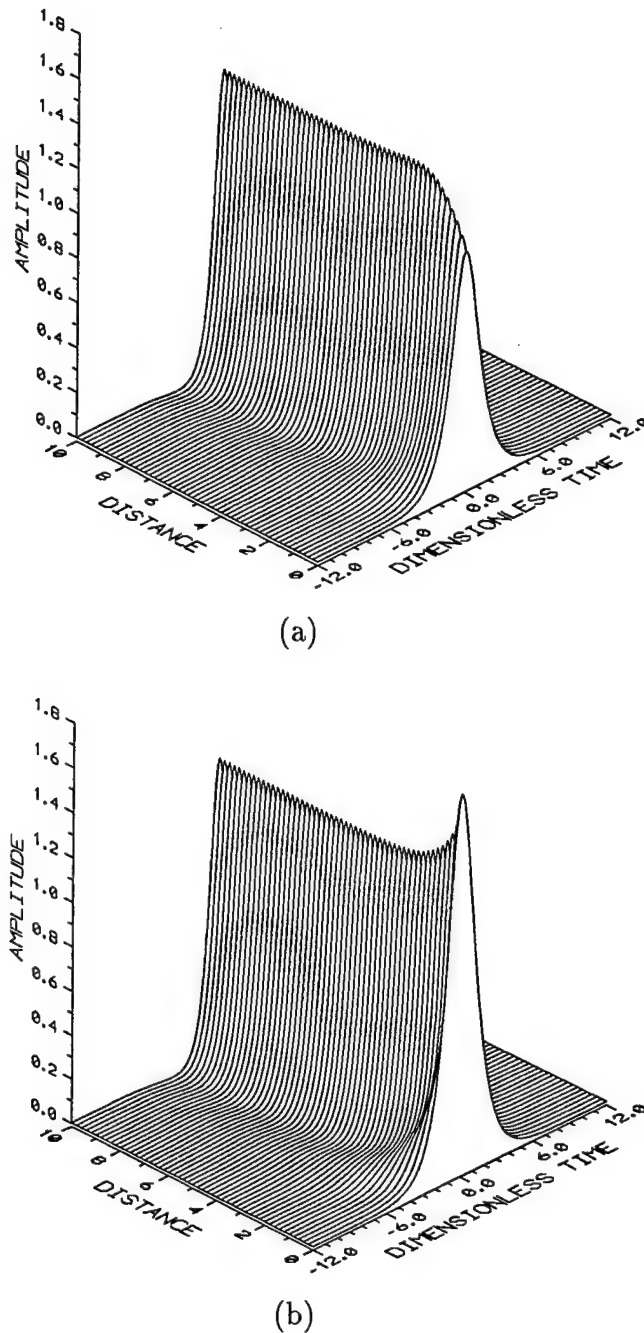


Figure 4.2: Evolution of initial hyperbolic-secant pulses $U(\tau, 0) = \text{sech } \tau$, (a), and $U(\tau, 0) = 1.8 \text{ sech } \tau$, (b), showing exponential decay onto the stable pulse solution. The parameters are: $\Gamma l = 1$ (corresponding to an amplifier spacing of 36 km), $\kappa = 1$, and $\Delta\alpha = 0.1$. The computations were run to $\xi = 10$ which explicitly shows the stability of the pulses.

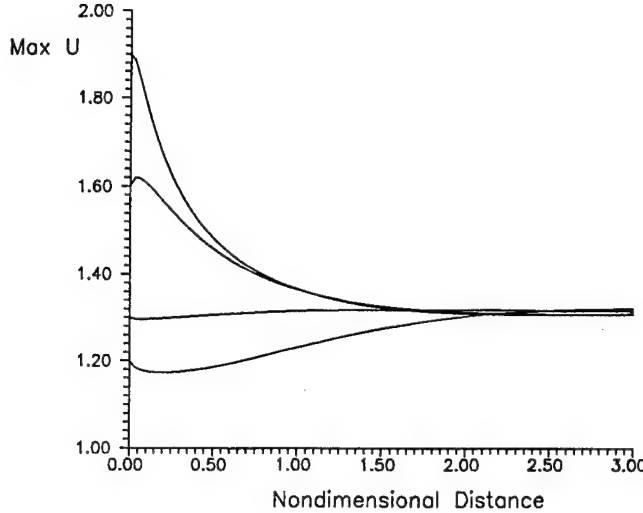


Figure 4.3: Asymptotic approach onto the final steady-state solution from initial conditions $U(\tau, 0) = A \operatorname{sech} 1.5\tau$, where $A = 1.9, 1.6, 1.3$ and 1.2 respectively. Note that the transient response to the initial amplitude is attenuated after a very short distance of the nondimensional distance ξ . Further, the steady-state is an attractor for a wide range of initial amplitudes. The parameter values used are identical with those of the previous figure.

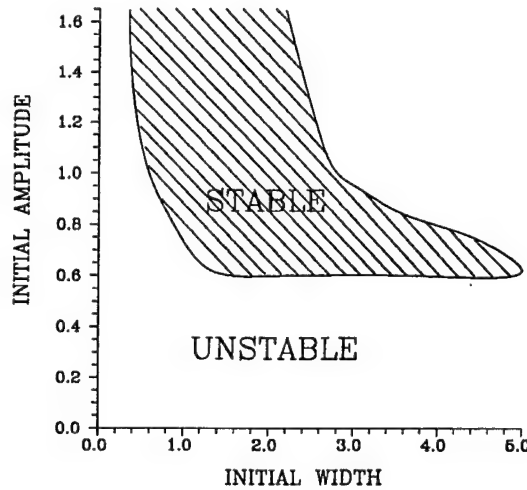


Figure 4.4: Initial pulse amplitudes A and widths T_0 which give stable pulse solutions for $\Gamma l = 1$, $\kappa = 1$, and $\Delta\alpha = 0.1$. The initial conditions $U(T, 0) = A \operatorname{sech}(T/T_0)$, with different values of A and T_0 , were used.

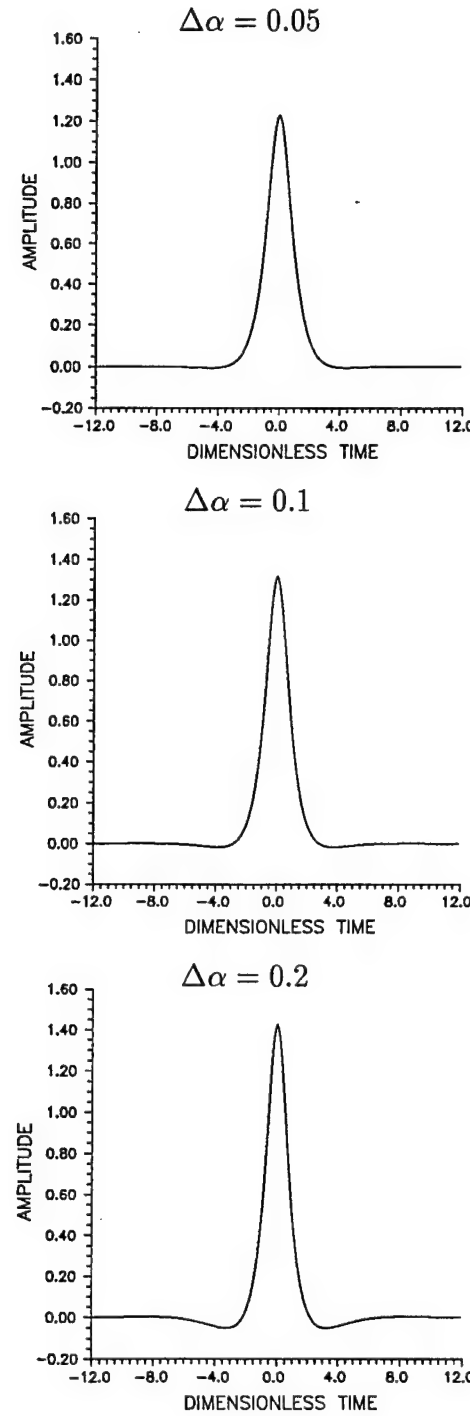


Figure 4.5: Final steady-state pulse profiles for different values of the overamplification parameter, $\Delta\alpha = 0.05, 0.10$, and 0.20 . Note the small wings in the pulse's profile which develop for the larger values of $\Delta\alpha$.

A crucial issue which is addressed at this juncture concerns the validity of the approximation Eq. (3.28) for the averaged evolution. A measure of the accuracy of the averaged envelope equation, Eq. (3.28), is obtained by comparing its solutions with numerical solutions of the full nonlinear Schrödinger equation with loss and periodic phase-sensitive amplification, Eq. (3.6). Figure 4.6a shows such a comparison for a total propagation distance of 10,000 km using the same initial pulse and physical parameters as those used in the simulation in Fig. 4.2a. Note that in this figure only the phase-locked quadrature of the full simulation of the NLS equation, i.e., A in Eq. (3.11), is plotted. Further, recall that due to the amplitude rescaling in Eq. (3.27a), the phase-locked quadrature of the full NLS simulations must be rescaled by the factor $[(1 - \exp(-2\Gamma l))/2\Gamma l]^{1/2}$ for comparison with Eq. (3.28). Because the two solutions are indistinguishable when plotted together, the difference between the two pulses is shown in Fig. 4.6b. Note that the difference is quite small, of order 10^{-4} , demonstrating that the averaged equation is an accurate approximation to the full NLS equation with loss and periodic phase-sensitive gain.

The majority of the difference between the two solutions can be attributed to second-order terms in the perturbation expansion (i.e., A_2) which have been ignored in this comparison. In addition, a small amount of linear dispersive radiation of $O(10^{-5})$ can be seen in Fig. 4.6b. It is largest in the vicinity of the main pulse and decreases away from it. This linear dispersive radiation is not expected to appear in the multiple-scale expansion because it is exponentially small in the perturbation parameter [42]. Such exponentially small terms typically do not show up in perturbation expansions using powers of the small parameter [34] unless special techniques are employed. [43]

It should be further noted that not all frequencies are present in the linear dispersive radiation. A detailed analysis of the linear response of an optical fiber line employing phase-sensitive amplifiers [32] shows that only certain frequencies are able to maintain phase-matching with the amplifiers as they propagate, and thus only these frequencies experience an overall gain close to unity as they pass through an optical fiber/PSA segment. The periodic forcing of the gain and loss can be shown to determine which frequencies become ‘transparent’ through a fiber-PSA line.

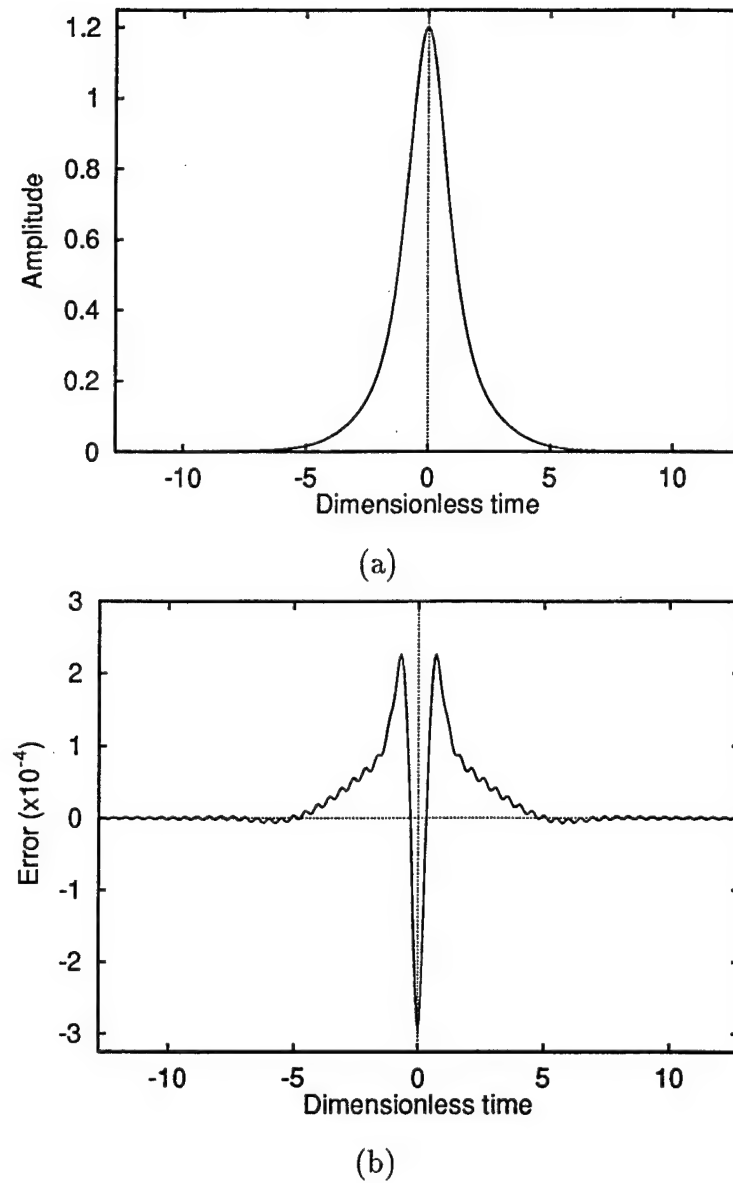


Figure 4.6: Comparison of the solutions of the averaged envelope equation and the full nonlinear Schrödinger equation with loss and periodic phase-sensitive amplification, showing the in-phase quadrature, (a), and the difference, (b), between the two solutions. The parameters are $\Gamma l = 1.0$, corresponding to an amplifier spacing of 36 km, $\kappa = 1$, and $\Delta\alpha = 0.1$. The solutions are plotted after a total propagation distance of 10,000 km or 275 amplifiers.

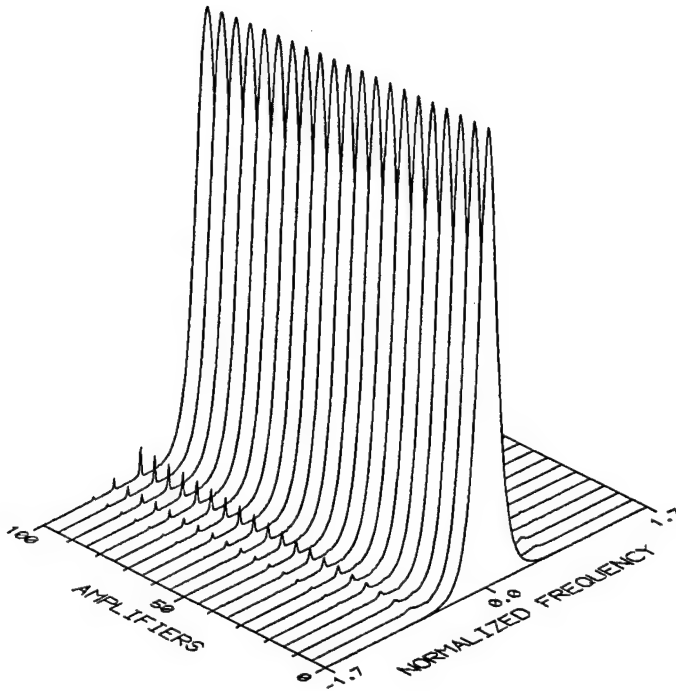


Figure 4.7: Spectral evolution over 10,000 km for an amplifier spacing of 100 km and $\Delta\alpha = 0.1$. Note that only certain frequencies, which are strongly dependent on the amplifier spacing, pass through the chain of amplifiers with unity gain. All other frequencies are attenuated.

Therefore, these frequencies exhibit a strong dependence upon the spacing between the amplifiers. For the calculations presented here the amplifier spacing was taken to be exactly periodic and thus the dispersive radiation is able to survive. In particular, Fig. 4.7 depicts the evolution of the spectrum of the full NLS equation with loss and phase-sensitive gain. For this figure, the amplifier spacing was chosen to be 100 km in order to more clearly depict the qualitative features of the spectrum as it evolves. Note the clear generation of several sideband frequencies. These sidebands are responsible for producing a background radiation field which is superimposed upon the soliton-like pulse propagation. As the amplifier spacing is decreased (increased), the amount of sideband frequency generated likewise decreases (increases). This then determines the amplitude of the background radiation field generated through the periodic forcing of the loss and gain. In a more realistic situation, where the amplifier spacing varies

somewhat with distance along the fiber line, this linear dispersive radiation is expected to be significantly reduced. The effect of variable amplifier spacing upon the solitons is expected to be minimal, however, because the solitons and the PSAs will be phase-locked. A more careful and detailed analysis regarding this situation is carried out in Chapter 6.

Upon comparing the anti-phase-locked quadrature B , which is an order of magnitude smaller than that of the phase-locked quadrature A , with that of the full NLS simulations, results similar to those found previously for the phase-locked quadrature are found to hold for B . In particular, Fig. 4.8 shows a comparison of the anti-phase-locked quadrature obtained from the averaged equation, a suitably rescaled Eq. (3.24), with the result for the anti-phase-locked quadrature obtained from the numerical solution of the NLS equation with loss and PSAs, i.e., B in Eq. (3.11). The two curves are plotted just after an amplifier in Fig. 4.8a, where the parameters and total propagation distance are the same as those for Fig. 4.6. Since the two curves are indistinguishable when plotted together, the difference between the two is plotted in Fig. 4.8b. Similar to the phase-locked quadrature, here a small amount of linear dispersive radiation is also seen.

In Chapter 3, Fig. 3.2 depicted the qualitative behavior of the phase-locked quadrature A . It is also illustrative to directly examine the stabilizing effect of the amplifiers by plotting the magnitude of the anti-phase-locked quadrature between the amplifiers. This is shown in Fig. 4.9, which provides clear evidence that after an amplifier the anti-phase-locked quadrature grows due to forcing from the dispersion and nonlinear self-phase modulation, but that upon reaching the next amplifier it is sharply attenuated. (Note that in this figure the exponential decay due to loss between the amplifiers has been factored out.)

In the preceding numerical simulations of Figs. 4.6–4.9, the solutions which are plotted are not yet close to a steady-state. Due to the suppression of the dispersion and self-phase modulation by the amplifiers, much longer distances are necessary for a true steady-state to be achieved. As an example, in Fig. 4.10 the value at the center of the pulse just after an amplifier is plotted as a function of distance (in dispersion lengths). Results from both the averaged equation, Eq. (3.28), and

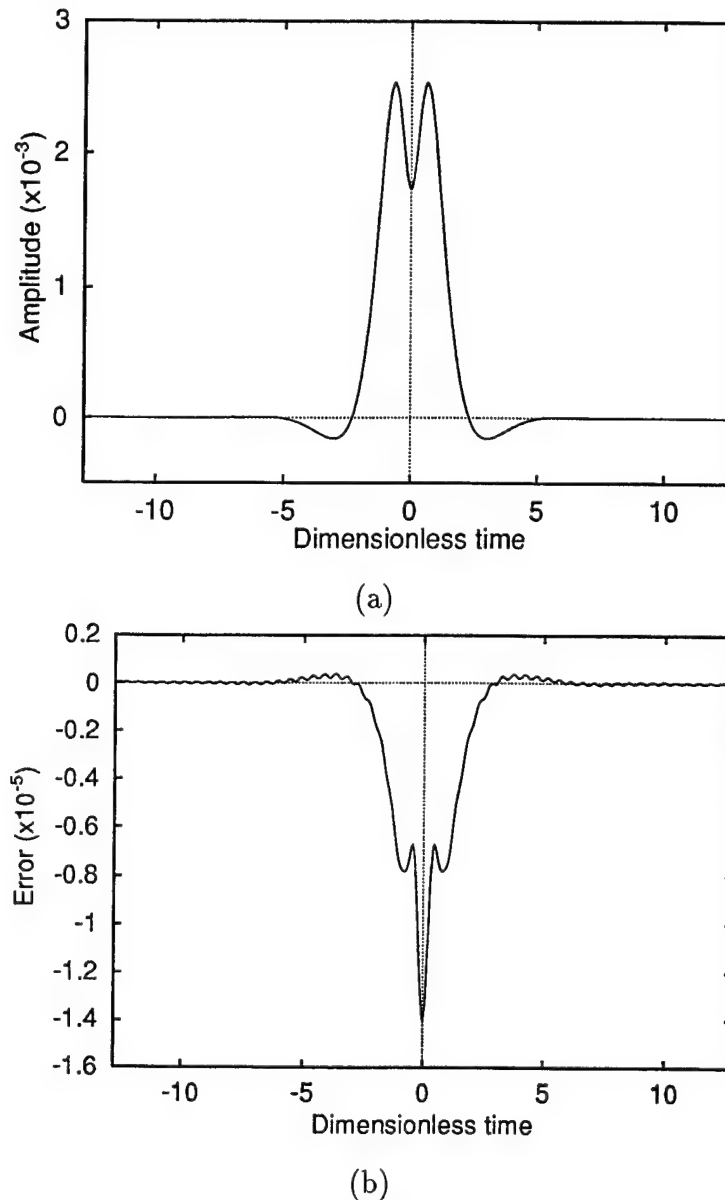


Figure 4.8: Comparison of the solutions of the averaged envelope equation and the full nonlinear Schrödinger equation with loss and periodic phase-sensitive amplification, showing the out-of-phase quadrature, (a), and the difference, (b), between the two solutions. The parameters are the same as in Fig. 4.6.

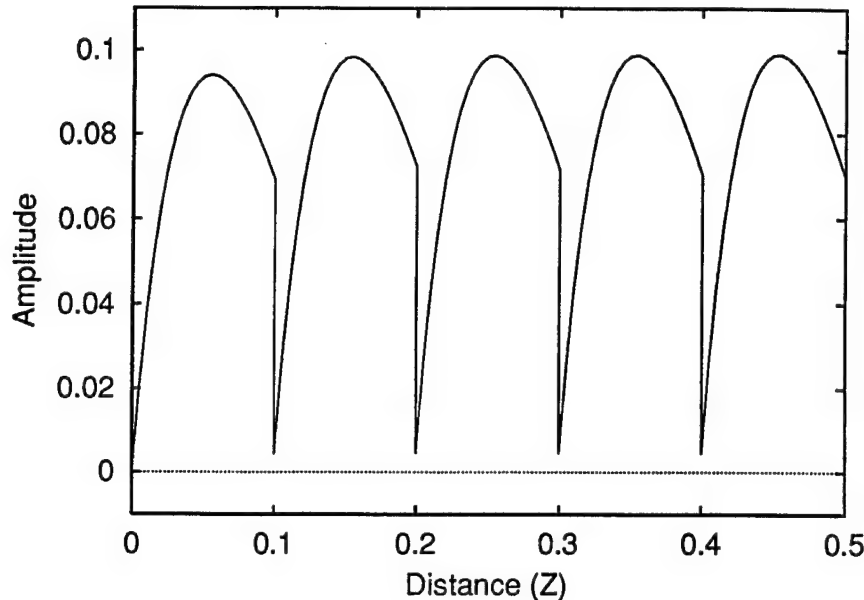


Figure 4.9: Midpoint value of the out-of-phase quadrature plotted as a function of distance, showing the evolution between the amplifiers (calculated using the full nonlinear Schrödinger equation with loss and periodic phase-sensitive amplification). The exponential decay due to loss between the amplifiers has been factored out. The magnitude grows after an amplifier, but upon reaching the next one it is sharply attenuated. Here the amplifier spacing is 50 km, and the distance is in terms of dispersion lengths ($z = 1$ corresponds to 500 km).

the full NLS simulations, Eq. (3.6), are plotted. The curves are once again almost indistinguishable. Note that the solution is not even close to the steady-state until the pulse has propagated approximately 50,000 km. This shows the degree to which the phase-sensitive amplifiers are able to eliminate the effects of dispersion and self-phase modulation.

In considering a fiber-PSA line for use in a communications system, it is of interest to determine how far one can push the parameter regime and still achieve stable pulse propagation. Therefore, the case for 100 km amplifier spacing is investigated. The results for the phase-locked and anti-phase-locked quadratures after 10,000 km are shown in Figs. 4.11a and 4.11b, respectively. In both figures, $\Gamma l = 2.76$, $\kappa = 1$, and $\Delta\alpha = 0.05$. Here the dispersive radiation generated as a result of the

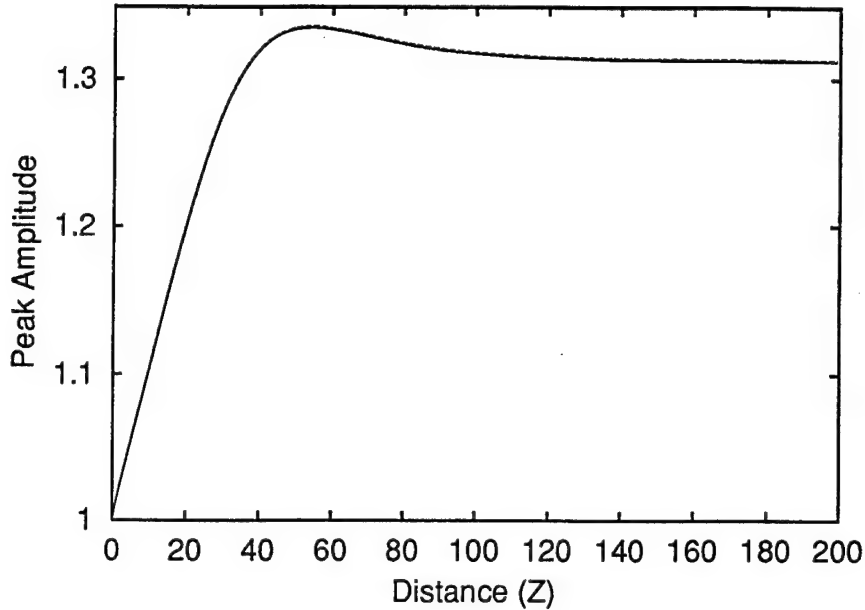


Figure 4.10: Midpoint value of the in-phase quadrature just after an amplifier plotted as a function of distance (dispersion lengths). Results from both the averaged equation (dashed curve), Eq. (3.28), and the full NLS equation with loss and periodic phase-sensitive amplification (solid curve) are plotted. The two are virtually indistinguishable. The parameters are $\Gamma l = 1.0$, $\kappa = 1$, and $\Delta\alpha = 0.1$. A total propagation distance of 100,000 km or 2750 is shown. Note that an approximate steady-state is not reached until after the pulse has propagated roughly 50,000 km.

periodic forcing by the loss and PSAs is relatively more pronounced, although it is still limited to a narrow range of frequencies by the action of the PSAs. Recall that Fig. 4.7 depicts the spectral evolution for these parameter values. As mentioned earlier, this radiation is expected to be largely eliminated when the amplifier spacing is allowed to vary along the length of the fiber. Note that these simulations were of the phase-locked quadrature using the full NLS with PSAs as given by Eq. (3.11). This is due to the fact that the averaged evolution is not capable of capturing the dispersive radiation which is exponentially small.

Finally, it is of interest to compare these numerical results with similar results obtained from the equations that are used to describe a communication system

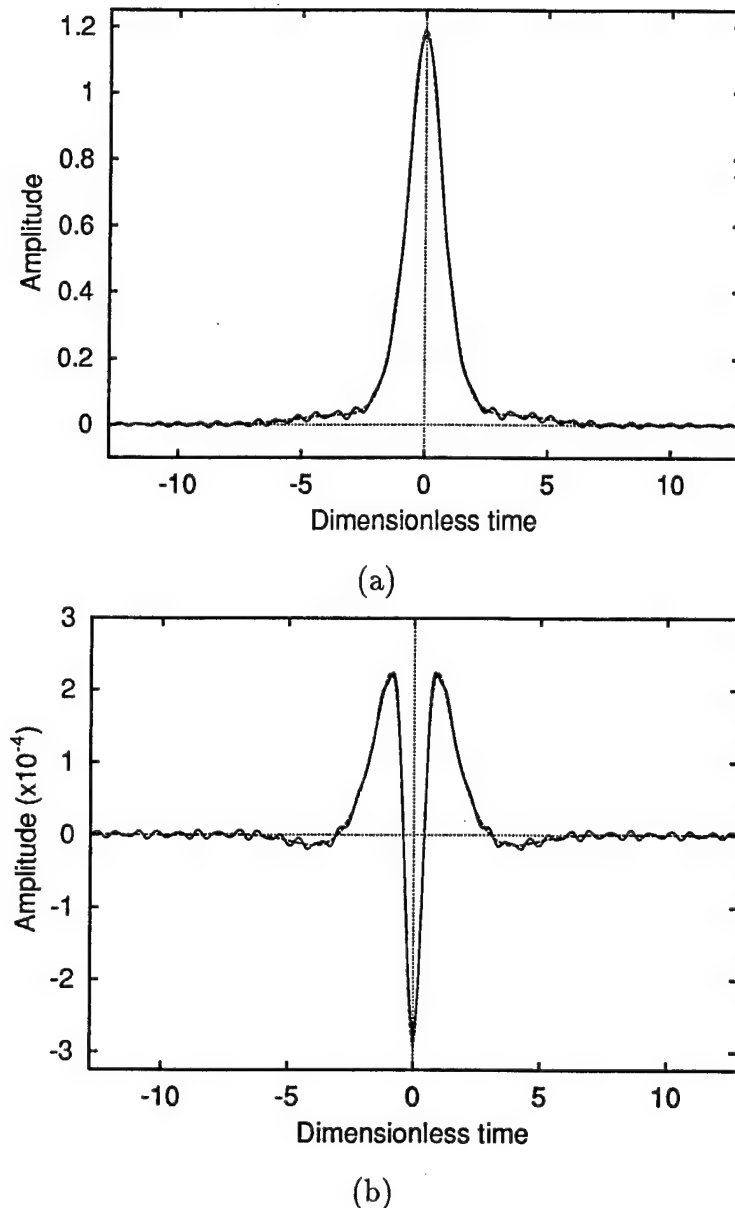


Figure 4.11: Comparison of the solutions of the averaged envelope equation (dotted lines) and the full nonlinear Schrödinger equation with loss and periodic phase-sensitive amplification (solid lines), for both the in-phase, (a), and out-of-phase, (b), quadratures. The parameters are $\Gamma l = 2.76$, corresponding to an amplifier spacing of 100 km, $\kappa = 1$, and $\Delta\alpha = 0.05$. The solutions are plotted after a total propagation distance of 10,000 km or 100 amplifiers.

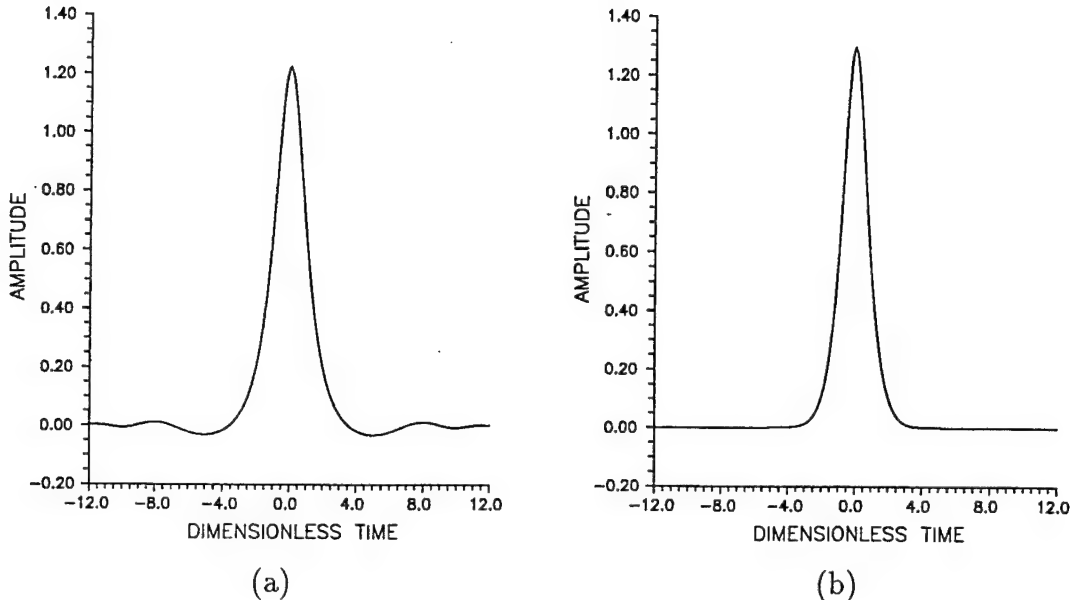


Figure 4.12: Qualitative comparison of pulse solutions showing the amount of dispersive radiation shed by the soliton-based communication systems employing erbium amplifiers, (a), and PSAs, (b). In both cases the initial pulse amplitude was taken to be 10% higher than the optimum (for a fixed width). The system employing PSAs, (b), generates considerably less linear dispersive radiation with such an initial condition. For these simulations, the dispersion length was taken to be 411 km, the amplifier spacing was 50 km, and the gain of the amplifiers was set to exactly cancel the fiber loss between the amplifiers. [18]

employing solitons and lumped erbium-doped fiber amplifiers [18]. The physical parameters in the numerical simulation of the erbium amplifier system include a dispersion length of 411 km and an amplifier spacing of 50 km. If the amplitude of the initial pulses in both cases are taken to be precisely those required for the corresponding steady-state solutions (a one-soliton in the erbium amplifier case), then the amount of dispersive radiation generated in each case is roughly of the same magnitude. If the amplitudes of the pulses are initially taken to be 10 percent larger than those required for the corresponding steady-state solutions, however, then the system employing erbium amplifiers generates a significant amount of dispersive radiation. This is illustrated in Figs. 4.12a and 4.12b. In the system employing PSAs, Fig. 4.12b, the

amplifiers attenuate most of the linear dispersive radiation that is shed by the pulse as it adjusts its amplitude. This can be understood from the underlying stability results of each system in consideration. Within the context of an erbium-doped line, which is a phase-insensitive amplifier system, the perturbations due to the loss and gain do not break the leading order Hamiltonian structure. Therefore, the excess ‘energy’ which is carried in the pulse through the initial amplitude and width fluctuations acts to generate a background radiation field as it cannot dissipate this excess ‘energy’. However, in the previous section, the averaged evolution with the PSAs is shown to exhibit a dissipative structure which simply attenuates exponentially any initial amplitude and width fluctuations.

4.4 Summary

At the onset of this chapter, the aim was to determine whether stable pulse solutions which were governed by the averaged evolution equation (3.28) could be supported in a fiber optic communications line. In general, one is forced to resort to numerical simulations to study the parameter regime of interest. However, in the limit of small amplifier spacing, perturbation and asymptotic methods allow for the extraction of valuable information concerning the pulse propagation and its stability. Remarkably enough, many of the underlying results found in the asymptotic limit hold qualitatively in the regime of physical interest. In what follows, the significant features of the stability analysis results are summarized.

To begin, it is noted that in order for a soliton-like pulse to propagate over long distances, a slight amount of overamplification must be supplied. As was mentioned in both Chapter 2 and Section 4.2, this requirement for overamplification arises due to the three wave interaction in the PSAs which convert a small amount of signal field into the pump field. This mechanism is also responsible for breaking the underlying Hamiltonian structure normally associated with the NLS.

Because the Hamiltonian structure is no longer applicable, the averaged evolution for the PSAs inherits the dynamics associated with dissipative, nonlinear systems. This fact allows the pulse propagation and its corresponding stability to

exhibit some markedly different behavior than that of its phase-insensitive counterpart. In particular, the asymptotic regime investigated in Section 4.2 implies that the steady-state solutions are reached in an exponential manner, i.e., the steady-state solutions act as attractors for a wide range of parameter values and initial conditions. Further, the transients associated with the initial conditions are attenuated on the slow $\bar{\xi}$ length scale without the generation of a background radiation field. This also is in stark contrast to the stability behavior of phase-insensitive amplifiers where the stability is reached via the shedding of a background radiation field. In a sense, the PSAs are shown to exhibit improved stability results provided the proper overamplification is supplied.

In this chapter, it has been shown, both analytically and numerically, that the averaged evolution is capable of supporting soliton-like pulse propagation over large distances for a wide range of input parameters. The goal of the next chapter will be to improve on this by further investigating the parameter space of the averaged evolution. In particular, the bifurcation structure of Eq. (3.28) can be quantified and the full range of parameter space can be explored. This allows one to further understand the limitations and validity of the approximations involved deriving the averaged evolution.

Chapter 5

Bifurcation Analysis

5.1 Introduction

In the last chapter, the aim was to develop an analytical and numerical framework from which to document the existence and stability of propagating soliton-like pulse solutions. This goal was achieved and the steady-state solutions were shown to act as exponential attractors for a wide range of parameters and initial conditions. However, each numerical simulation was limited to the exploration of a single steady-state for fixed values of Γl and $\Delta\alpha$ respectively. Further, it was required that each initial condition be investigated individually to insure that they indeed approached the appropriate final steady-state. In order to provide any extensive overview and detail concerning the full range of parameter space, many simulations would be required which would lead to considerable computational expense.

The aim of this chapter is develop an alternative method which can explore parameter space in a relatively simple manner and which will not require large numerical simulations and computational expense. The idea then is to try and develop some scheme which can produce a more general understanding of the parameter space and its stable and unstable steady-states. Once the stable and unstable branch of solutions are known, the bifurcation structure associated with Eq. (3.28) can be easily understood.

In Section 5.2, use is once again made of well known asymptotic and perturbation methods in order to investigate a parameter regime which is crucial to the understanding of the bifurcation structure of the averaged evolution. Just as in Sec-

tion 4.2 of the previous chapter, the parameter regime for which this is applicable is not of physical interest. However, the results obtained are indicative of a bifurcation structure valid for a wide range of parameters. This section will be followed by an analysis of the steady-states of Eq. (3.28) using the bifurcation software package AUTO. Here, the stable and unstable branch of solutions can be found by simply tracking the steady-states for a wide range of parameter space which incurs little computational expense.

As was mentioned in Chapter 3, the averaged evolution and its solution structure is at the heart of this dissertation. Therefore, upon combining the results found in Sections 5.2 and 5.3, the qualitative and quantitative features of the solution branches of Eq. (3.28) can be documented and well understood in terms of the bifurcation structure. This then gives a clearer picture of the stability of long-distance pulse propagation and the potential advantages of a fiber-PSA communications line for a wide range of physically realizable parameter values.

5.2 Bifurcation from the Trivial Solution

The focus of the last chapter was to understand the stability of the steady-state hyperbolic secant solutions of Eq. (3.28) for $U \sim O(1)$. And in particular, asymptotics were used in Section 4.2 in order to understand the limit $\Gamma l \ll 1$ and $\Delta\alpha \ll 1$. In this section, the asymptotic regime of interest to be explored corresponds to $U \ll O(1)$ for arbitrary Γl and $\Delta\alpha$. Therefore, the stability of the basic solution, which corresponds to U identically zero, is considered [44]. This can be simply done by linearizing Eq. (3.28) about the basic state, i.e., letting

$$U = 0 + \tilde{U}, \quad (5.1)$$

where $\tilde{U} \ll O(1)$ and the higher order terms are ignored. Inserting Eq. (5.1) into Eq. (3.28), the linearized evolution about the basic state is governed by

$$\frac{\partial \tilde{U}}{\partial \xi} + \frac{1}{4} \frac{\partial^4 \tilde{U}}{\partial \tau^4} - \frac{1}{2} \frac{\partial^2 \tilde{U}}{\partial \tau^2} + \left(\frac{1}{4} - \Delta\alpha \right) \tilde{U} = 0. \quad (5.2)$$

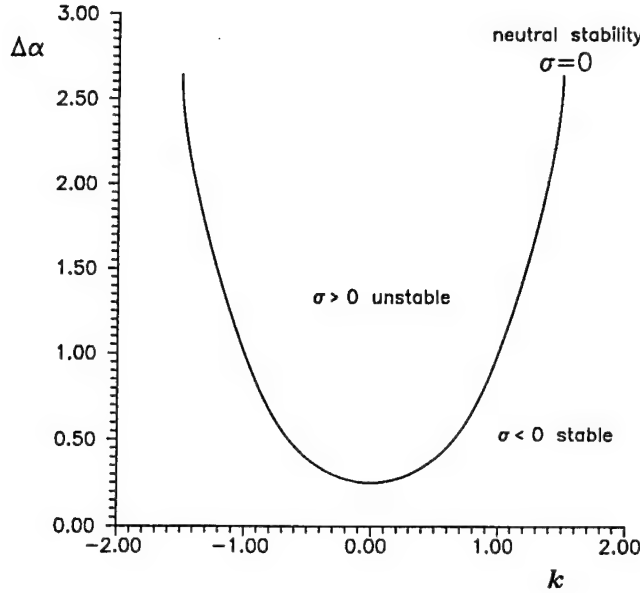


Figure 5.1: Plot of the neutral stability curve ($\sigma = 0$) in the wavenumber k versus overamplification $\Delta\alpha$ plane. Note that the most unstable wavenumber, $k = 0$, corresponds to a value of $\Delta\alpha = 1/4$.

In order to understand the linearized evolution given by Eq. (5.2), it is convenient to look for a Fourier-mode solution of the form $U = \exp(\sigma\xi + ik\tau)$. This then gives the dispersion relation

$$\sigma + \frac{1}{4}k^4 + \frac{1}{2}k^2 + \left(\frac{1}{4} - \Delta\alpha\right) = 0. \quad (5.3)$$

Note that for $\sigma < (>) 0$, the solution is stable (unstable). The value $\sigma = 0$ corresponds to neutral stability and is given by the following relation between the wave number k and the critical overamplification parameter value $\Delta\alpha_c$

$$\Delta\alpha_c = \frac{1}{4} (k^2 + 1)^2. \quad (5.4)$$

The neutral stability curve given by Eq. (5.4) is depicted in Fig. 5.1. As can be seen from this figure, the zero wavenumber is the most unstable wavenumber. Therefore, the remainder of the analysis in this section will be carried out in the vicinity of $(U, \Delta\alpha) = (0, 1/4)$ for arbitrary Γl .

The preceding analysis identifies the appropriate regime to be explored. Therefore, in order to determine the dynamics and behavior of the solution near the

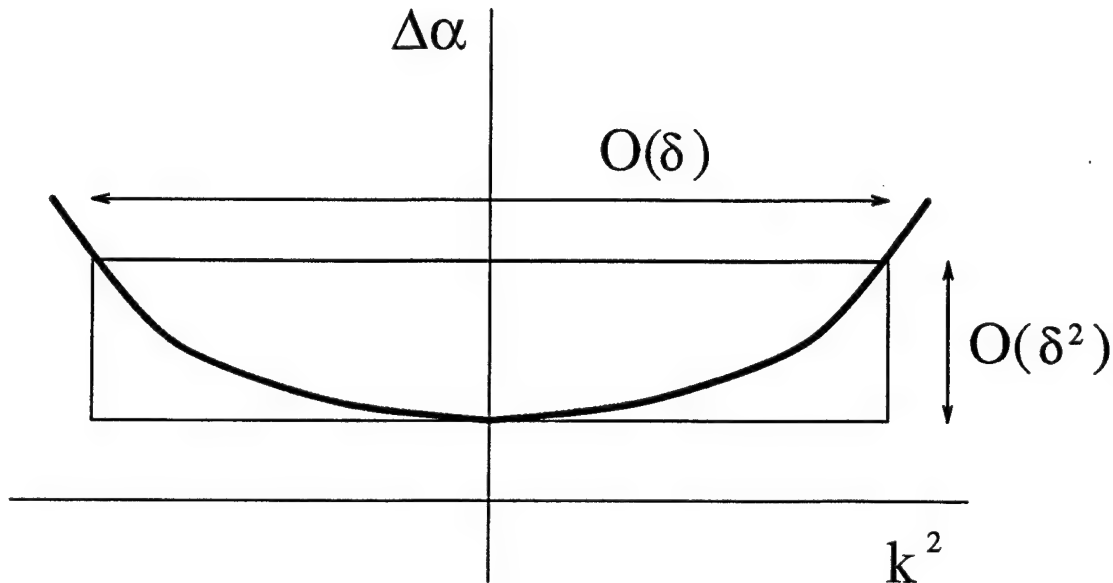


Figure 5.2: Qualitative depiction of the scalings associated with the neutral stability curve ($\sigma = 0$) in the k^2 versus $\Delta\alpha$ plane. Note the quadratic relation between the squared wavenumber and overamplification.

minimum of the neutral stability curve, it is necessary to expand about $U = 0$ and $\Delta\alpha = 1/4$. Higher order terms will now be important in determining the bifurcation structure, and therefore they cannot be neglected. Prior to expanding however, use is once again made of appropriately defined multiple-scales. As in previous chapters, the slow evolution associated with the linearized operator can be correctly and conveniently captured using these new slow scales. Note that because of the quadratic relationship between the squared wavenumber and the overamplification (see Fig. 5.2), the following slow spatial and time variables can be introduced in order to determine the appropriate behavior near the unstable values of the wavenumber and overamplification [44], i.e., define

$$\eta = \delta^2 \bar{\xi} \quad (5.5a)$$

$$\hat{\tau} = \delta \tau, \quad (5.5b)$$

where again $\delta \ll 1$. These scales will capture any slow growth in the perturbation which will be measured in δ .

Now expand about the zero wavenumber to determine the behavior of the solution near the minimum of the neutral stability curve, i.e., let

$$U = 0 + \delta U^1(\bar{\xi}, \tau, \eta, \hat{\tau}) + \delta^2 U^2(\bar{\xi}, \tau, \eta, \hat{\tau}) + \dots \quad (5.6a)$$

$$\Delta\alpha = \frac{1}{4} - \delta^2 \mu + \dots \quad (5.6b)$$

Collecting those terms which are of leading order, it is found that

$$L U^1 = \frac{\partial U^1}{\partial \xi} + \frac{1}{4} \frac{\partial^4 U^1}{\partial \tau^4} - \frac{1}{2} \frac{\partial^2 U^1}{\partial \tau^2} = 0. \quad (5.7)$$

The steady-state solution can be simply given by a ‘constant’ with respect to the fast variables, i.e., $U^1 = V(\hat{\tau}, \eta)$. This solution follows from the fact that the expansion is about the zero wavenumber, i.e., $\exp ik\tau = \exp i(0 + \epsilon)\tau = V(\hat{\tau})$.

Solving at higher order and requiring the forcing terms to be in the range of the linearized operator (e.g. solvability must be satisfied) gives nothing new at $O(\epsilon^2)$. However, at $O(\epsilon^3)$ the slow evolution of the envelope $V(\hat{\tau}, \eta)$ can be found. The evolution is governed by

$$\frac{\partial V}{\partial \eta} = \frac{1}{2} \frac{\partial^2 V}{\partial \hat{\tau}^2} + V^3 - \mu V, \quad (5.8)$$

with $V \rightarrow 0$ as $\hat{\tau} \rightarrow \pm\infty$ [44]. Note the striking resemblance of the right hand side of Eq. (5.8) with the definition of the L_- operator of the last chapter. In particular, if $\mu = 1/2$ then Eq. (5.8) reduces to analyzing $\partial V/\partial \eta + L_- V = 0$. With this in mind and recalling that $L_-(\operatorname{sech} \tau) = 0$, a steady-state solution to Eq. (5.8) can be easily found for values of $\mu > 0$. This steady-state is given by

$$V_s = \sqrt{2\mu} \operatorname{sech} \sqrt{2\mu} \hat{\tau}, \quad (5.9)$$

where V_s denotes the steady-state solution. It now remains to determine the stability of the above steady-state. Therefore, linearize about V_s in the following manner

$$V = V_s(\hat{\tau}) + \tilde{V}(\hat{\tau}, \eta), \quad (5.10)$$

where $\tilde{V} \ll V_s$. The higher order terms can be neglected due to the fact the stability can be determined from the first correction term \tilde{V} . In particular, upon making the

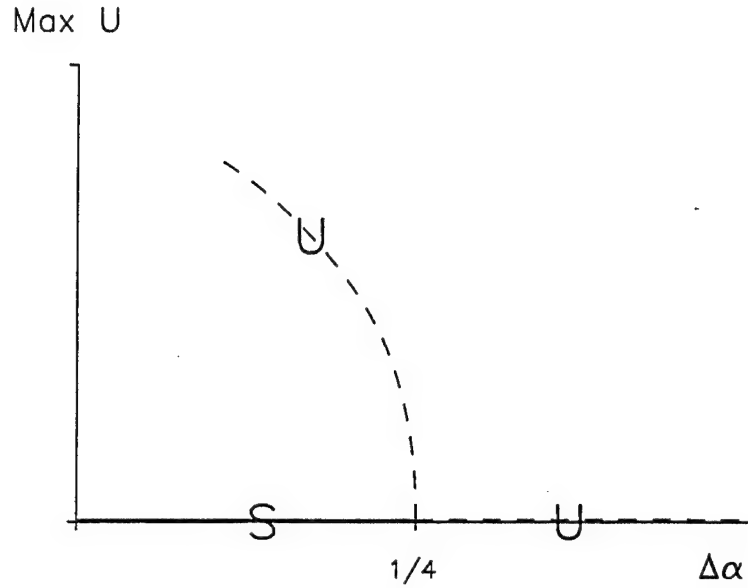


Figure 5.3: Characteristic behavior of the subcritical bifurcation emanating from $(U, \Delta\alpha) = (0, 1/4)$. Note that S (solid line) corresponds to the stable branch of solutions and U (dashed line) to the unstable branch.

substitution $\tilde{V} = We^{\sigma\eta}$ and substituting Eq. (5.10) into Eq. (5.8), it is found that the stability of the leading order hyperbolic secant solution reduces to understanding the behavior of

$$\hat{L}_+ W = \sigma W, \quad (5.11)$$

where $\hat{L}_+ = \frac{1}{2} \frac{\partial^2}{\partial \tilde{\tau}^2} + 3(V^s)^2 - \mu$. From the previous chapter, it is known that the operator \hat{L}_+ as defined contains one positive eigenmode. This mode will give rise to exponential growth and instability. Therefore, it can be understood that the hyperbolic secant, steady-state branch of solutions which emanates from the bifurcation point $(U, \tilde{\alpha}) = (0, \frac{1}{4})$ is unstable and gives rise to a subcritical bifurcation from the basic solution $U = 0$. This is depicted in Fig. 5.3.

The foregoing analysis has implied the existence of a subcritical bifurcation from $U = 0$ for $\Delta\alpha = 1/4$ and Γl arbitrary. Note that the analysis is limited to an asymptotic regime which is $O(\delta)$ away from the bifurcation point. It is of interest however, to determine the global nature of the bifurcation structure associated with the averaged evolution. In the next section, through use of the bifurcation soft-

ware package AUTO, the full bifurcation diagram associated with Eq. (3.28) will be explored for a wide range of parameters which are outside the asymptotic regimes explored thus far. It will be shown that the solution branch associated with the sub-critical bifurcation from $U = 0$ will eventually reach a limit point and fold back onto the stable steady-state branch of solutions of Eq. (3.28) which were found in the last chapter.

5.3 Bifurcation Structure via AUTO

In this section, the bifurcation software package AUTO [45] is used to determine the steady-state solutions and bifurcation diagram associated with Eq. (3.28). In particular, our aim is to explore the full range of parameters for which Eq. (3.28) gives rise to stable pulse solutions. AUTO allows for the investigation of the parameter regime which is beyond the range of the asymptotic and perturbation analysis of the previous section and Section 4.2 of the last chapter.

AUTO is a software package which allows for the numerical continuation of steady-state solution branches in parameter space. In particular, AUTO is capable of performing numerical analysis of systems of nonlinear differential or algebraic equations. The concern here will be with systems of differential equations. And of primary concern will be the detection of both bifurcation points and limit points. In what follows, Eq. (3.28) with $\partial U / \partial \bar{\xi} = 0$ is considered as a system of four coupled ordinary differential equations with some appropriate boundary conditions.

Implementing AUTO does not follow directly from Eq. (3.28) because an exact solution from which to start the calculations does not exist. However, an associated problem may be considered which exhibits an exact solution. Namely, the iterated NLS equation is considered. The iterated NLS is obtained by simply taking the derivative of Eq. (3.3) (with $\gamma = 0$) with respect to Z and making use of the fact that mixed partials can be interchanged. Looking strictly at steady-state solutions ($\partial / \partial Z \rightarrow 0$), the iterated-NLS structure can be expressed as follows

$$\left(\frac{\partial^2}{\partial \tau^2} - 1 \right)^2 V - 8V^3 + 12V^5 + 12V \left(\frac{\partial V}{\partial \tau} \right)^2 + 12V^2 \frac{\partial^2 V}{\partial \tau^2} = 0. \quad (5.12)$$

Therefore, a homotopy from the iterated NLS equation is used in view of the exact hyperbolic secant solution it exhibits, i.e $V = \operatorname{sech} \tau$. Once this is implemented and the correct boundary conditions are imposed, AUTO can be used to explore the full parameter regimes of Γl and $\Delta\alpha$. Note that the terms of Eq. (5.12) are identical to those which are found for the averaged evolution of Eq. (3.28) with the exception of the coefficients.

Since the aim is to make use of a homotopy from the iterated-NLS, the steady-state fourth-order ODE of Eq. 5.12 can be combined with that of the averaged evolution of Eq. (3.28). This gives the following combined steady-state equation

$$\begin{aligned} & \left(\frac{\partial^2}{\partial \tau^2} - 1 \right)^2 U + (1 - \theta) \left[-8U^3 + 12U^5 + 12U \left(\frac{\partial U}{\partial \tau} \right)^2 + 12U^2 \frac{\partial^2 U}{\partial \tau^2} \right] \\ & + \theta \left[-4\Delta\alpha U - 4U^3 + 4U^5 + 12\beta U \left(\frac{\partial U}{\partial \tau} \right)^2 + 4(\beta + 1)U^2 \frac{\partial^2 U}{\partial \tau^2} \right] = 0, \quad (5.13) \end{aligned}$$

where for $\theta = 0$ Eq. (5.13) reduces to the iterated NLS and for $\theta = 1$ Eq. (5.13) reduces to the averaged evolution of Eq. (3.28). Since the interest is in using a homotopy from the iterated NLS to get a solution for the averaged equation, θ will be treated as parameter which is initially zero and is continued so that θ becomes unity. This then will give an initial starting solution for exploring the parameter space of the averaged evolution.

Before proceeding to find appropriate boundary conditions, it will be helpful to express Eq. (5.13) as a set of coupled first-order, nonlinear differential equations. Therefore, Eq. (5.13) can be expressed in the following form

$$U'_1 = TU_2 \quad (5.14a)$$

$$U'_2 = TU_3 \quad (5.14b)$$

$$U'_3 = TU_4 \quad (5.14c)$$

$$\begin{aligned} U'_4 &= T [2U_3 - U_1 \\ &+ (1 - \theta) \{8U_1^3 - 12U_1^5 - 12U_1U_2^2 - 12U_1^2U_3\}] \\ &+ \theta \{4\Delta\alpha U_1 + 4U_1^3 - 4U_1^5 + 12\beta U_1U_2^2 + 4(\beta + 1)U_1^2U_3\}], \quad (5.14d) \end{aligned}$$

where $U_i = \partial^{(i-1)}U/\partial\tau^{(i-1)}$ and the prime denotes differentiation with respect to τ . In the above, the averaged evolution and the iterated NLS have been considered on some finite interval $\tau \in [-T, T]$. The appearance of T in Eqs. (5.14) reflects the fact that the interval $[-T, T]$ has been scaled on to the interval $\tau \in [-1, 1]$. Therefore, $\tau = 1$ now represents the edge of the computational domain.

At this point, the appropriate boundary conditions associated with the system of ODEs is considered. Two of the four boundary conditions imposed are due to the even symmetry of the solution about the origin, i.e., $\partial U/\partial\tau = 0$ and $\partial^3 U/\partial\tau^3 = 0$ at $\tau = 0$. The remaining two boundary conditions considered are derived from the decaying modes associated with the linear part of the fourth-order evolution. In particular, when far from the localized pulse, the nonlinear terms can be neglected and the steady-state evolution reduces to the linear equation given by

$$\frac{\partial^4 U}{\partial\tau^4} - 2\frac{\partial^2 U}{\partial\tau^2} + (1 - 4\Delta\alpha)U = 0. \quad (5.15)$$

Letting $U = e^\lambda\tau$ gives rise to a fourth-order characteristic equation whose eigenvalues are given by

$$\lambda = \pm\sqrt{1 + \gamma}, \pm\sqrt{1 - \gamma}, \quad (5.16)$$

where $\gamma = \sqrt{4\Delta\alpha}$. Note that the eigenvalues imply the existence of two growth and two decay eigenmodes for $\Delta\alpha < 1/4$. For $\Delta\alpha > 1/4$, Eq. (5.16) implies the existence of one decay, one growth, and a pair of complex conjugate modes. In what follows, it will be assumed that $\Delta\alpha < 1/4$ and appropriate boundary conditions will be derived for this case.

Far from the pulse, the growth modes, $-\sqrt{1 + \gamma}$ and $-\sqrt{1 - \gamma}$, are unphysical. This then leaves the two decay modes, $-\sqrt{1 + \gamma}$ and $-\sqrt{1 - \gamma}$, from which a second order ODE can be constructed from the characteristic equation

$$\lambda^2 + (\sqrt{1 + \gamma} + \sqrt{1 - \gamma})\lambda + \sqrt{1 - \gamma^2} = 0. \quad (5.17)$$

The associated ODE, which governs the two decay modes of the fourth-order evolution, is now easily shown to behave according to

$$\frac{\partial^2 U}{\partial\tau^2} + (\sqrt{1 + \gamma} + \sqrt{1 - \gamma})\frac{\partial U}{\partial\tau} + \sqrt{1 - \gamma^2}U = 0. \quad (5.18)$$

Eq. (5.18) along with its derivative

$$\frac{\partial^3 U}{\partial \tau^3} + (\sqrt{1+\gamma} + \sqrt{1-\gamma}) \frac{\partial^2 U}{\partial \tau^2} + \sqrt{1-\gamma^2} U_\tau = 0 \quad (5.19)$$

are the two appropriate boundary conditions to be imposed at the end point of the computational domain. Written in terms of the appropriate system of ODEs, all four boundary conditions can be expressed succinctly as follows

$$U_3(1) + [\sqrt{1+\gamma} + \sqrt{1-\gamma}] U_2(1) + \sqrt{1-\gamma^2} U_1(1) = 0 \quad (5.20a)$$

$$U_4(1) + [\sqrt{1+\gamma} + \sqrt{1-\gamma}] U_3(1) + \sqrt{1-\gamma^2} U_2(1) = 0 \quad (5.20b)$$

$$U_2(0) = 0 \quad (5.20c)$$

$$U_4(0) = 0. \quad (5.20d)$$

Here $U_i(1)$ represents the amplitude at the edge of the computational domain while $U_i(0)$ is the value at the center of the computational domain.

Equations (5.14) with its boundary conditions given by Eqs. (5.20) can now be implemented directly into AUTO. Starting with an initial hyperbolic secant profile and $\theta = 0$, the length of the computational domain, T in Eqs. (5.14), is increased. After reaching a large value for the size of the computational domain, the homotopy parameter θ is increased from zero to unity. The overamplification $\Delta\alpha$ and parameter Γl can then be adjusted independently in search of bifurcation points and limit points. In what follows, the results of this search are given.

In Fig. 5.4, the maximum pulse amplitude of the steady-state solutions versus Γl is explored for two different values of the overamplification parameter $\Delta\alpha$. In particular, the values of $\Delta\alpha = 0.1$ and $\Delta\alpha = 0.2$ are considered. Note that the steady-states persist as Γl approaches large numbers, i.e., infinity. Although the amplitude of U in Eq. (3.28) remains $O(1)$ as Γl approaches such large values, the physical pulse envelope R grows without bound as Γl approaches infinity. This can be understood from the amplitude rescaling

$$R = \left(\frac{1 - e^{-2\Gamma l}}{2\Gamma l} \right)^{-1/2} U,$$

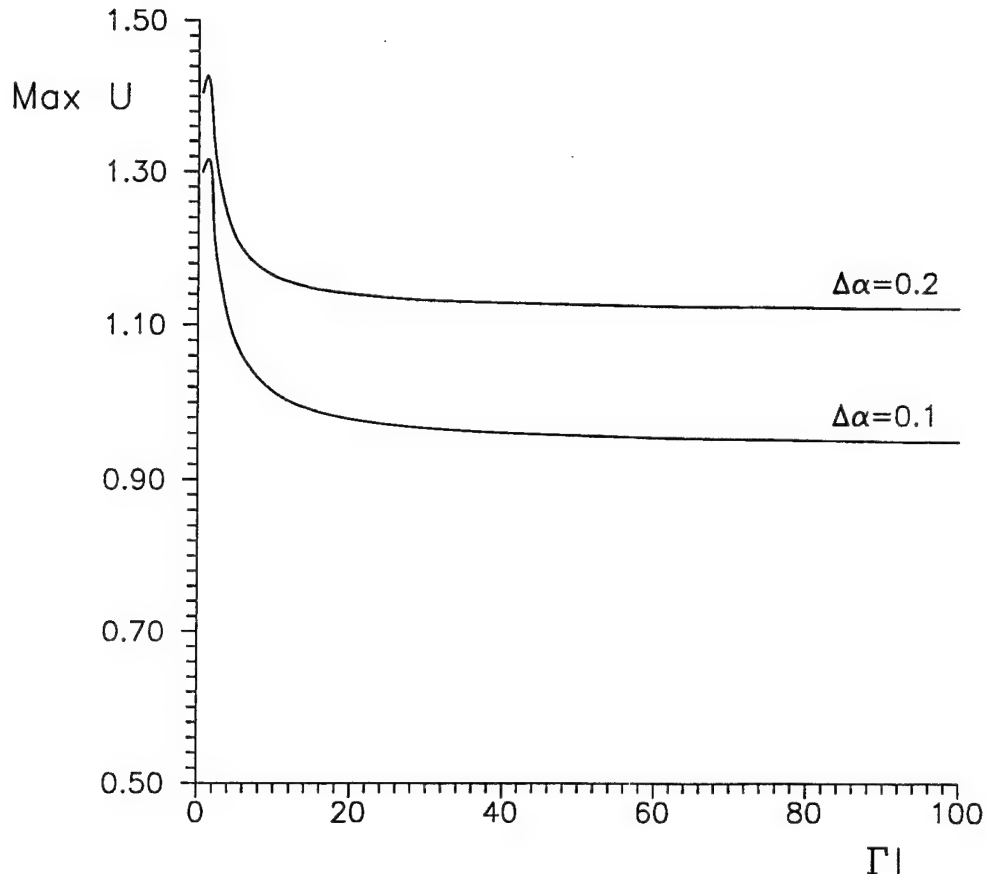


Figure 5.4: Depiction of the maximum amplitude U as a function of the parameter Γl for the values of $\Delta\alpha = 0.1$ and $\Delta\alpha = 0.2$.

where the phase rotation κ has been taken to be unity in Eq. (3.27). Figure 5.4 reflects a remarkable range in parameter space which is capable of supporting stable, propagating pulse solutions. Note however that the averaged evolution equation ceases to be valid for such large values of Γl .

The steady-state solutions computed via AUTO can be compared to the numerical simulations of Eq. (3.28). Figs. 5.5a and 5.5b, show a comparison for the values of $\Gamma l = 1$ and $\Delta\alpha = 0.2$. Various propagation times indicate the exponential approach of solutions of Eq. (3.28) to the steady-state branch of solution computed via AUTO. In particular, Fig. 5.5a shows half the pulse profile computed using AUTO along with the averaged pulse envelope computed from Eq. (3.28) for the propagation distances of $\xi = 20$ and $\xi = 50$. Figure 5.5b depicts the comparison for the values

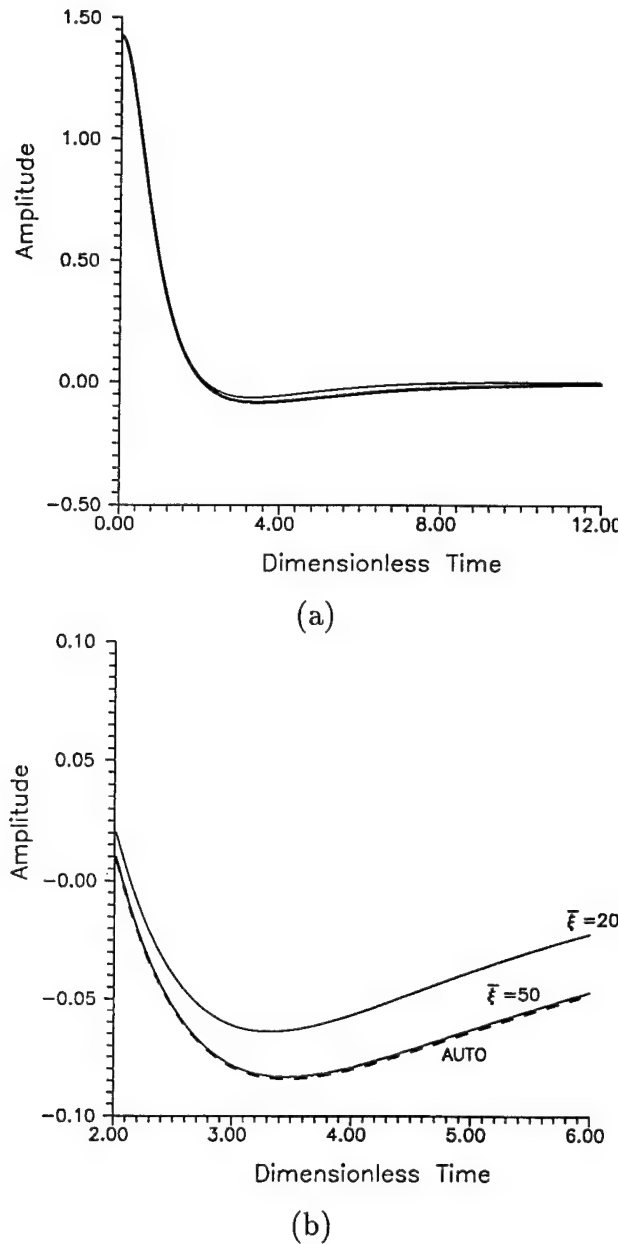


Figure 5.5: Comparison of steady-states computed via AUTO versus full numerical simulations of the averaged evolution. Three pulse profiles are depicted corresponding to the AUTO solution and the averaged evolution for values of $\bar{\xi} = 20$ and $\bar{\xi} = 50$. In (a) $\tau \in [0, 12]$. (b) contains the interval $\tau \in [2, 6]$ which further depicts the difference in the three solutions. Note that as $\bar{\xi}$ gets large, the averaged solution approaches the steady-state solution generated via AUTO.

of $\tau \in [2, 6]$. Note that as ξ gets large, the averaged evolution from Eq. (3.28) approaches the AUTO solution. AUTO provides a direct method for finding the final steady-state without having to propagate the solution of the averaged evolution for large times. Similar numerical results hold for various values of the parameters Γl and overamplification $\Delta\alpha$.

Returning now to the aim of this section, which is the investigation of the bifurcation diagram associated with Eq. (3.28), the stable and unstable solution branches are computed for various values of Γl and $\Delta\alpha$. It is convenient to begin by fixing the values of Γl and exploring the maximum amplitude as a function of the overamplification $\Delta\alpha$. From this perspective, Figs. 5.6a-d depict the subcritical bifurcation from $\Delta\alpha = 1/4$ for various values of Γl . This is in agreement with the analysis of the previous section. Note that after the unstable branch reaches the limit point, the solution branch folds back and becomes the branch of solutions which correspond to the stable pulses of physical interest. As the value of Γl increases, the limit point moves away from values of $\Delta\alpha$ near zero. The bifurcation diagram associated with Γl as it approaches infinity is essentially given by Fig. 5.6d.

Next, the value of $\Delta\alpha$ is fixed and an investigation of the maximum amplitude as a function of the parameter Γl is carried out. Fig. 5.7 depicts both the stable and unstable branches as Γl is increased towards large values (i.e., infinity). For values of the overamplification above a critical value, the stable and unstable solution branches associated with a fixed value of Γl remain disconnected for all values of Γl . However, once the overamplification drops below a certain value, $\Delta\alpha < .088$, the stable and unstable branches are joined and limit points exists in the amplitude versus Γl plane. This can be thought of as an isola in the parameter space where the size of the isola is dependent on the value of the overamplification $\Delta\alpha$, i.e., as values of $\Delta\alpha$ get smaller (larger), so does the isola. This behavior is represented in Fig. 5.7 for various values of the overamplification $\Delta\alpha$.

In conclusion, this section demonstrates that AUTO provides an efficient and effective way in which to explore the parameter regime of Eq. (3.28). Stable pulse solutions are shown to exist and be in good agreement with numerical simulations of the full averaged equation. Further, AUTO avoids long computational runs associated

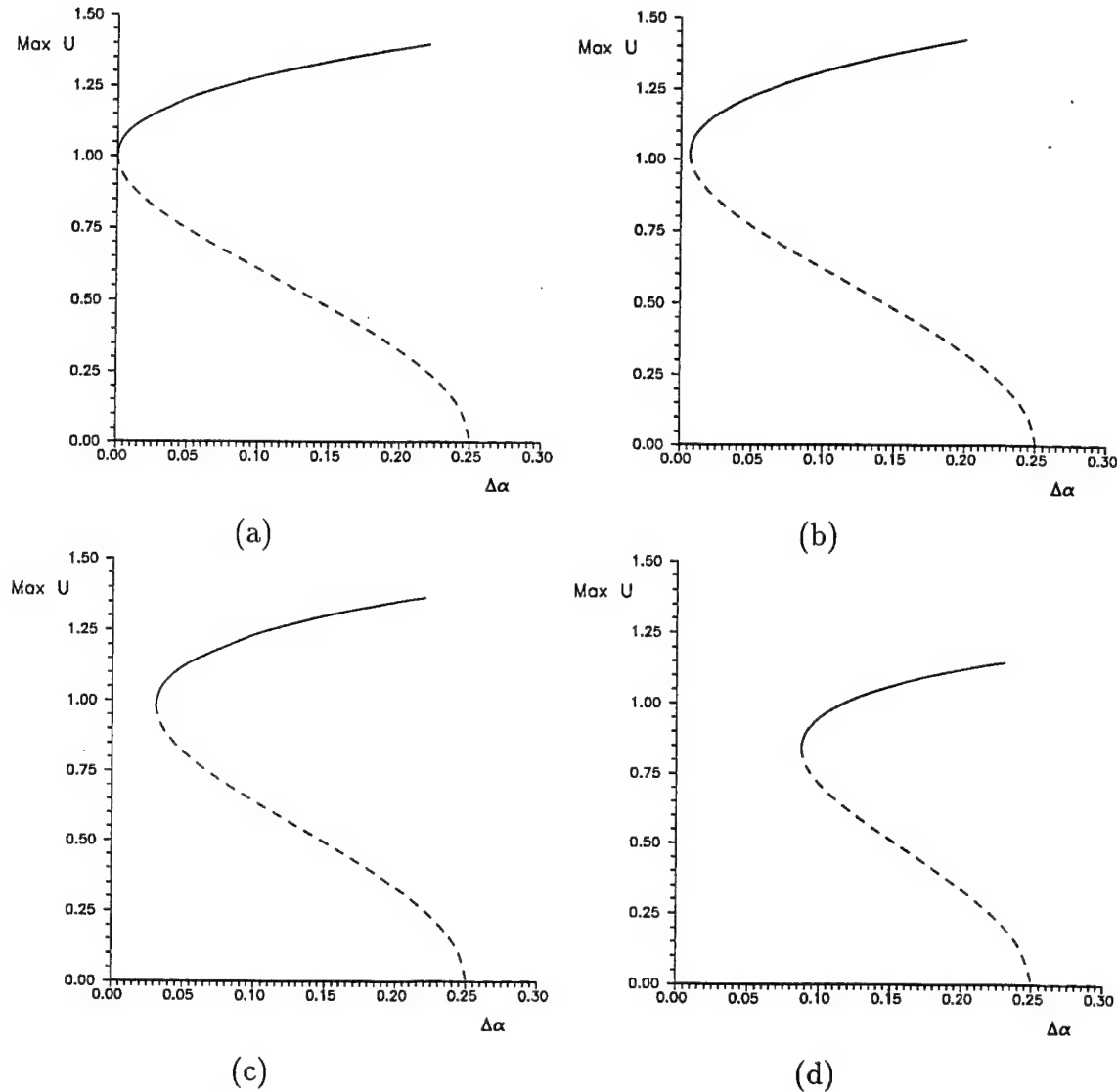


Figure 5.6: Bifurcation diagrams associated with the averaged envelope equation. The solid lines correspond to stable solutions while the dashed line corresponds to the unstable. In each case, the $U = 0$ solution is stable (unstable) for $\Delta\alpha < (>)1/4$. (a),(b),(c) and (d) depict the subcritical bifurcation from $\Delta\alpha = 1/4$ and the location of the limit point for the values of $\Delta\alpha = .02, 1, 2, 100$ respectively. Note that as Γl is increased from near zero to infinity, the limit point moves from $\Delta\alpha \sim 0$ to $\Delta\alpha \sim 0.088$.

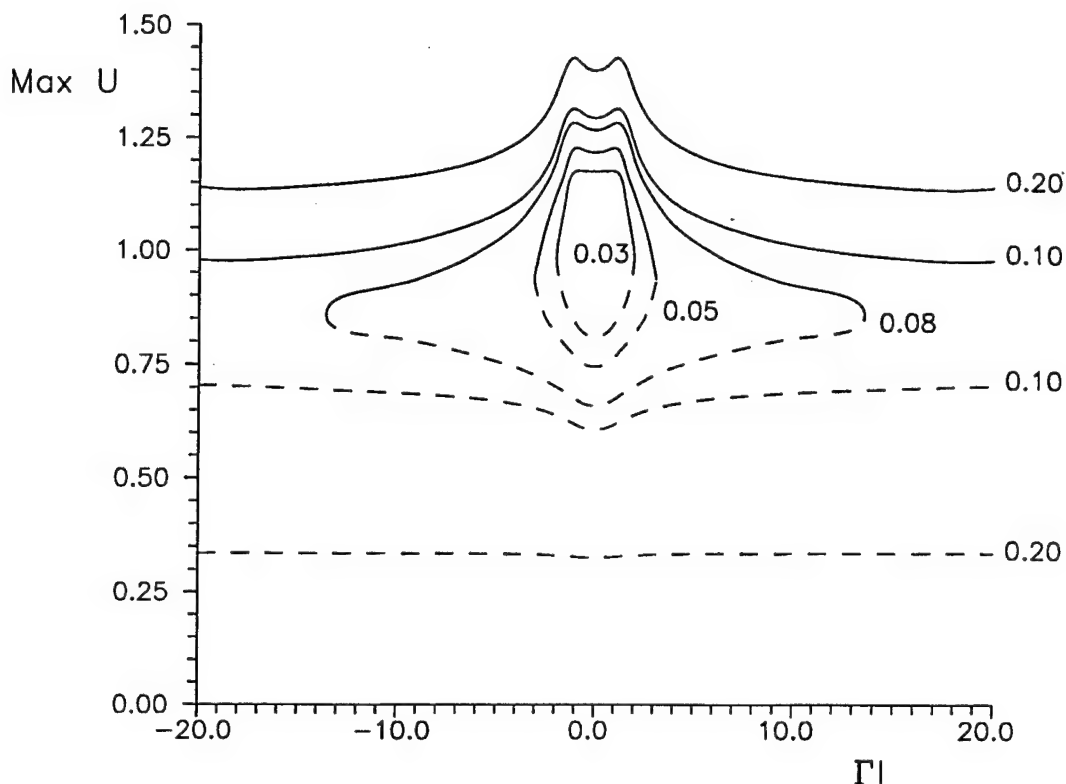


Figure 5.7: Solution curves in the amplitude versus Γl plane. The solution curves correspond to differing values of the overamplification parameter $\Delta\alpha$. Note the isolas which exists for values of $\Delta\alpha < 0.088$. As the overamplification becomes larger however, the solution branches separate into an upper and lower branch corresponding to stable and unstable branch solutions of the pulse propagation.

with finding steady-state solutions of the averaged evolution of Eq. (3.28). Instead, AUTO simply gives the steady-state solution for a wide range of parameter values and significantly reduces computational expense.

5.4 Summary

In this chapter, the bifurcation structure of the averaged evolution is explored. In particular, emphasis is placed on obtaining information regarding the stable and unstable steady-state pulse solutions and their dependence on the param-

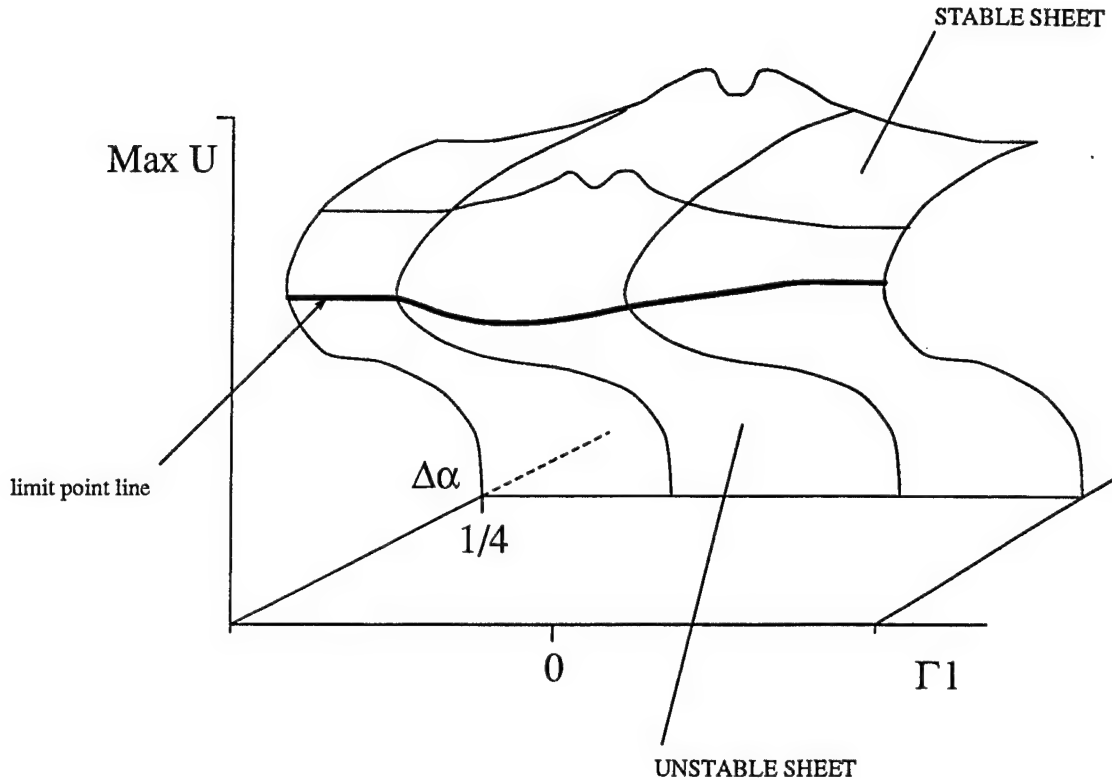


Figure 5.8: Qualitative structure of the bifurcation diagram associated with the averaged evolution. This is essentially a combination of the previous two figures which depict the amplitude versus. $\Delta\alpha$ and amplitude versus. Γl planes respectively.

eters Γl and $\Delta\alpha$. In contrast with the previous chapter, an alternative method for exploring the full range of parameter space is presented which does not depend on the initial conditions or full numerical simulations of Eq. (3.28).

In Section 5.2, asymptotic methods can be applied the averaged evolution in the vicinity of the basic solution $U \equiv 0$ in order to describe the subcritical bifurcation which occurs at $\Delta\alpha = 1/4$. Although this analysis is only valid in a small regime, it holds for arbitrary values of Γl . Therefore, it describes a ‘global’ behavior which aids in the understanding of the full bifurcation structure of Eq. (3.28).

Section 5.3 contains the bulk of this chapter’s results. It is this section which presents the results of the use of the software continuation package AUTO. AUTO provides a method for which to track steady-state branches of solutions regardless of

their stability. Moreover, AUTO is capable of detecting both bifurcation and limit points for a given set of couple, nonlinear ODEs. For the purposes of this chapter, steady-states of Eq. (3.28) were considered which allowed the averaged evolution to be described by the set of four, nonlinear, first-order ODEs of Eqs. (5.14). The use of AUTO provides a computationally inexpensive and rapid method for determining the dependence of the steady-states on the parameters Γl and $\Delta\alpha$.

The results of this entire chapter can be succinctly summarized in Fig. 5.8. Figure 5.8 combines the explorations of parameter space of Sections 5.2 and 5.3 to show the complete qualitative bifurcation diagram in the space of the maximum amplitude, Γl and $\Delta\alpha$. Note that although negative values of Γl are not permitted physically, they are convenient here in understanding the behavior of the steady-state solutions of Eq. (3.28). This gives the full bifurcation structure in the space of the relevant parameters of the problem.

Chapter 6

Variable Amplifier Spacing

6.1 Introduction

It is the purpose of this chapter to further investigate the assumption made concerning the periodic amplifier spacing which was essential in the averaging analysis of the previous chapters. The aim will be to understand a system which is more realistic in its dependence upon the amplifier spacing and to further understand the mechanism which gives rise to the sideband frequency generation and its accompanying background radiation field. In a sense, this chapter's primary concern is to investigate the spectral evolution and frequency dependence of a fiber-PSA communications line as it relates to the amplifier spacing.

Chapters 3-5 represent the analysis of a nonlinear optical communications system with periodically-spaced PSAs. In what has been considered, only the leading order, phase-matched behavior of the PSAs has been investigated. This led to the derivation of a fourth-order, nonlinear evolution equation which governs the soliton-like pulse propagation over a length scale much longer than that of the soliton period. The assumptions of perfect phase-matching and periodic amplifier spacing allowed for significant simplification of the governing model for the pulse propagation and allowed for a straight forward averaging of the phase-locked quadrature. These assumptions however, ignored both the bandwidth restrictions of the amplifier and the frequency components which arise due to the periodic forcing of the loss and gain. In particular, the assumption of perfect phase-matching, $\Delta k = 0$, allowed the phase-sensitive amplification to be frequency independent. Therefore, the PSAs were of an infinite

bandwidth and amplified all frequencies in an identical manner. In Section 2.5, this assumption was shown to be an excellent approximation to the physically realizable system and any bandwidth restrictions due to the amplifiers can be ignored. However, as was pointed out in Section 4.3, numerical simulations of the full NLS with PSAs indicate the generation of a background radiation field (see Figs. 4.11 and 4.7). This field arises due to the sideband frequencies generated via the periodic forcing of the loss and gain.

In Sections 6.3 and 6.4, the effect of variable amplifier spacing upon the averaged soliton-like pulse propagation is considered. Recall, that the assumption of periodic amplifier spacing allowed for the multiple-scale averaging of Chapter 3 to yield the effective evolution of Eq. (3.28). When the amplifier spacing is no longer periodic, any averaging procedure can be quickly rendered intractable and of little use. In certain cases however, an averaged evolution can still be derived. Specifically, Section 6.3 considers the averaged pulse evolution when the PSAs are alternately separated by two distinct amplifier spacings.

One advantage lies within the assumption of non-periodic amplifier spacings, namely the reduction of the dispersive radiation generated through the gain-loss forcings to the governing NLS. This fact is made clear upon recalling that the frequency of the dispersive radiation is strongly dependent upon the amplifier spacing. In other words, for a given periodic amplifier spacing, the pulse propagation will contain certain frequency ‘windows’ which experience unity gain from the PSAs. When the spacings are allowed to vary, these windows are no longer able to persist and the radiation which is generated from the periodic forcings are slowly attenuated. More on this will be given in Section 6.2. In particular, the dependence of the sideband frequencies upon the amplifier spacing can be analytically understood far from the localized pulse.

The analysis presented in the following sections will be largely concerned with understanding how the varying amplifier spacings effects the stability of propagating soliton-like pulses, i.e, the robustness of the localized pulse evolution is investigated. As always, the aim is to more fully understand the qualitative and quantitative consequences of physical effects which are of higher order upon the leading order anal-

ysis of Chapters 3-5. In particular, the focus will be centered on the use of variably spaced amplifiers as a possible mechanism for attenuating the dispersive radiation.

6.2 Sideband Frequency Generation

It was found in Chapter 4 that full numerical simulations of the NLS with periodically spaced PSAs generated a small background radiation field. This behavior was depicted most clearly in Figs 4.11 and 4.7. Further, the amplitude of the dispersive radiation was found to be dependent upon the amplifier spacing, i.e., the larger (smaller) the amplifier spacing, the larger (smaller) the corresponding radiation. For the case in which the amplifier spacing was 36 km, the background radiation was of $O(10^{-5})$ and could be essentially neglected (see Fig. 4.6). However, as the amplifier spacing was increased to 100 km, the radiation was visibly noticeable (see Fig. 4.11) and of $O(10^{-3})$. It was briefly mentioned in Section 4.3 that this radiation field was strongly dependent upon the periodic nature of the amplifiers. The aim of this section is to further understand the radiation field generated by the PSAs and to more clearly understand its dependence on the amplifier spacing.

To further understand this dependence of the radiation on the periodic amplifier spacing, an analysis will be carried out which is far from the localized soliton-like pulse. Therefore, consider the pulse evolution given by Eq. (3.6) which governs the NLS with periodically spaced PSAs. Far from the localized soliton-like pulse, the radiation is small and the nonlinearity becomes negligible. Ignoring the nonlinear term in Eq. (3.6) then gives the following equation governing the evolution of the dispersive radiation

$$i\frac{\partial Q}{\partial Z} + \frac{1}{2}\frac{\partial^2 Q}{\partial^2 T} + i\gamma Q = 0, \quad (6.1)$$

where the definition of $\gamma = \Gamma/\epsilon$ has been used and the jump condition of Eq. (3.8) applies at each amplifier. Unlike the averaging which was carried out in Chapter 3, Eq. (6.1) is linear and can be examined directly using Fourier transform methods. In particular, transforming Eq. (6.1) gives

$$\hat{Q} = \hat{Q}_0 e^{(-\gamma - i\omega^2/2)Z}, \quad (6.2)$$

where \hat{Q}_0 is the transform of the initial pulse profile. Moreover, the jump condition of Eq. (3.8), which is frequency independent, can also be transformed to give

$$\hat{Q}_+ = \cosh \alpha \hat{Q}_- + e^{i\phi_n} \sinh \alpha \hat{Q}_-^*, \quad (6.3)$$

where ϕ_n is the pump phase at the n^{th} amplifier. By defining $\hat{Q}_n = e^{-i\phi_n/2} \hat{Q}_+$ and making use of Eqs. (6.2) and (6.3), it can be easily found that the following relation now holds

$$\hat{Q}_n = [\cosh \alpha e^{-i\nu} \hat{Q}_{n-1} + \sinh \alpha e^{i\nu} \hat{Q}_{n-1}^*] e^{-\Gamma l}, \quad (6.4)$$

where $\nu = (Z_l/Z_0)(1+\omega^2)/2$, it has been assumed that the phase rotation is constant, i.e. $\delta\phi_n = \delta\phi = Z_l/Z_0$, and use has been made of the relationship $\gamma Z_l/Z_0 = \Gamma l$.

As was found in Chapter 3, the quadrature separation given by Eq. (3.9) greatly simplifies the analysis by decomposing the propagating pulse into phase-locked and anti-phase-locked components. This same quadrature decomposition can be used in Eq. (6.4) by introducing the quadrature variables as follows

$$\hat{A}_n = \frac{1}{2}(\hat{Q}_n + \hat{Q}_n^*) \quad (6.5a)$$

$$\hat{B}_n = \frac{1}{2}(\hat{Q}_n - \hat{Q}_n^*), \quad (6.5b)$$

where once again \hat{A}_n and \hat{B}_n represent the phase-locked and anti-phase-locked quadratures respectively. Introducing Eqs. (6.5) into Eq. (6.4) reduces the linear propagation problem into a set of coupled difference equations given by

$$\begin{pmatrix} \hat{A}_n \\ \hat{B}_n \end{pmatrix} = e^{-\Gamma l} \begin{pmatrix} e^\alpha \cos \nu & -ie^\alpha \sin \nu \\ -ie^{-\alpha} \sin \nu & e^{-\alpha} \cos \nu \end{pmatrix} \begin{pmatrix} \hat{A}_{n-1} \\ \hat{B}_{n-1} \end{pmatrix}. \quad (6.6)$$

The eigenvalues of this matrix can be readily computed to determine the frequency dependence of the linear dispersion in the fiber-PSA line upon the amplifier spacing. In particular, it is found that

$$\lambda_{\pm} = e^{-\Gamma l} \left[\cos \nu \cosh \alpha \pm \sqrt{\cos^2 \nu \cosh^2 \alpha - 1} \right]. \quad (6.7)$$

Upon recalling the fact that $\nu = (Z_l/Z_0)(1+\omega^2)/2$, the eigenvalue of the phase-locked quadrature, which correspond to λ_+ , can be plotted to determine the gain as a function of the modified frequency ν . Fig. 6.1 plots the real and imaginary parts of λ_+

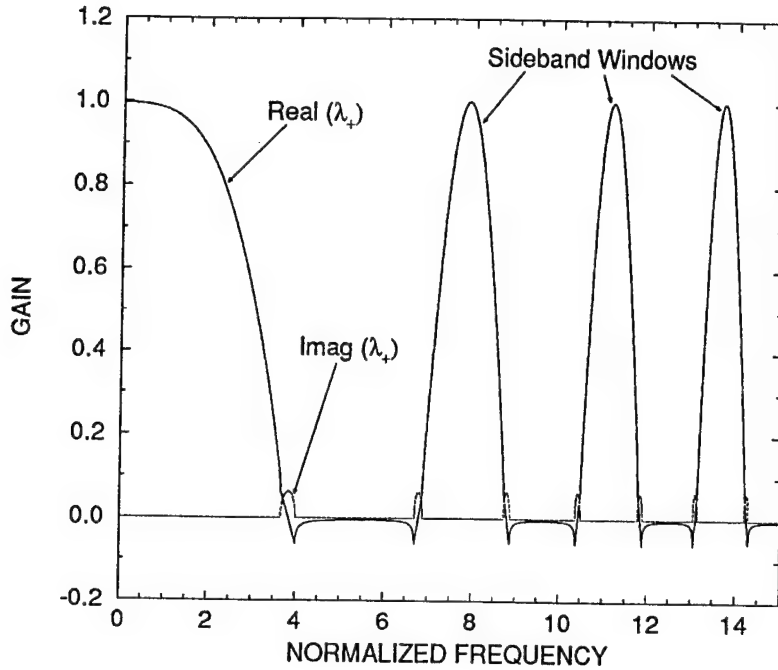


Figure 6.1: Depiction of the frequency windows which allow the propagating pulse to experience unity gain. Note that for these windows, the fiber-PSA line becomes effectively ‘transparent’.

versus the modified frequency. Specifically, note the frequency windows which experience a unity gain, or rather, a slight gain above unity due to the overamplification, which is $\Delta\alpha = 0.1$ in this case. These windows of transparency are responsible for the generation of the sideband frequencies which cause the linear dispersive radiation.

Although the preceding analysis is valid only far from the soliton-like pulses, the qualitative behavior remains the same when considering the full nonlinear evolution. In fact, Fig. 6.1 should be somewhat reminiscent of the spectral evolution of the full NLS with PSAs given in Fig. 4.7. In Fig. 4.7, the first and second sideband frequencies can be clearly seen while the third is barely visible. These first, second and third sidebands of Fig. 4.7 correspond to the first, second and third frequency windows of Fig. 6.1 respectively.

One can imagine that if the amplifier spacing varied along the fiber-PSA communications link, the windows of transparency would be altered at each consecutive amplifier. Therefore, the frequencies which experienced a unity gain at one amplifier, would now be shifted out of the range of transparency and would experience a gain of less than unity. This would lead to the attenuation of the radiation field generated from the sideband frequencies. This suggests the possibility of using the variable amplifier spacing as a method of attenuating the background radiation field. More on this will be discussed in the upcoming sections.

6.3 Two Distinct Amplifier Spacings

The aim of this section and the next is to investigate the effects of a variable amplifier spacing upon the stability of long distance pulse propagation and its associated dispersive radiation field. Typically, this task is rendered intractable and one must resort to numerical simulations. However, as a special case, the long-distance pulse propagation of a soliton-like pulse is considered in which the amplifier spacing alternates between two distinct lengths. Therefore, the underlying pulse propagation will remain periodic, but the period will now be measured over two amplifiers. This causes the windows of transparencies to alternate between two differing sets of frequencies which in turn should reduce the amount radiation generated.

Once again, the use of multiple-scale techniques can be exploited in order to average over the two distinct amplifier spacings. The analysis follows in a similar manner to that carried out in Chapter 3. In particular, use can be made of the results obtained in Chapter 3 in order to simplify what follows. Therefore, the following rescalings of Eq. (3.6), which are motivated by Eq (3.27), can be made

$$Q \rightarrow \kappa^{1/2} a_0^{-1/2} Q \quad (6.8a)$$

$$T \rightarrow \kappa^{-1/2} T, \quad (6.8b)$$

where once again $\kappa = d\phi/dZ$ and a_0 represents the average energy of the pulse over the two amplifier period. In the previous analysis of Chapter 3, the rescalings

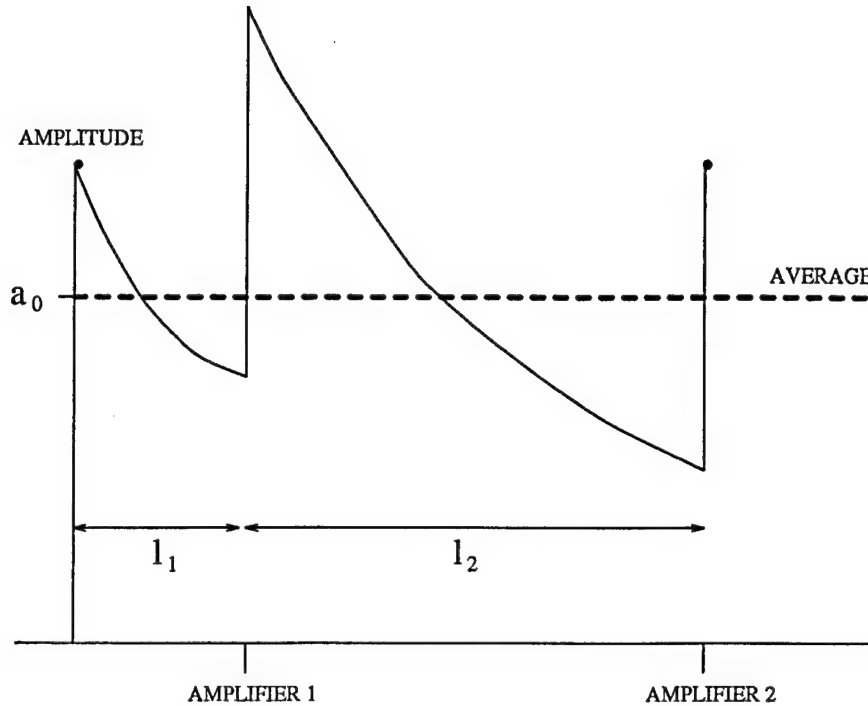


Figure 6.2: Qualitative depiction of the periodic structure associated with the two amplifier spacing case

of Eqs. (6.8) were carried out in Eqs. (3.27) at the end of the averaging analysis. Here, these rescalings will be performed beforehand in order to simplify the remaining analysis. Note that for this case, it will be assumed that the phase-rotation rate κ and the overamplification will be the same for both amplifier spacings. The assumption concerning the overamplification can easily be relaxed to account for differing amounts of overamplification at each amplifier. Further, it will be assumed that the evolution over the two amplifier spacings occurs such that each exhibits a common average. More will be said on this shortly.

The governing evolution equation (3.6) is then transformed through Eq. (6.8) to the following rescaled version

$$\frac{\partial Q}{\partial Z} = i \frac{\kappa}{2} \frac{\partial^2 Q}{\partial^2 T} + i \frac{\kappa}{a_0} |Q|^2 Q + \frac{1}{\epsilon} \left[-\Gamma Q + h \left(\frac{Z}{\epsilon} \right) Q + e^{i\phi(Z)} f \left(\frac{Z}{\epsilon} \right) Q^* \right], \quad (6.9)$$

where $h(\zeta)$ and $f(\zeta)$ are defined by Eq. (3.7) and the definition of ϵ is as before with the amplifier spacing now being the average of the two distinct lengths. Defining the

multiple scales as before to be $\zeta = Z/\epsilon$ and $\xi = \epsilon Z$, the multiple-scale averaging can now be easily carried out by once again introducing the quadrature decomposition given by

$$Q = [A(\zeta, \xi, T) + i\epsilon B(\zeta, \xi, T)] e^{i\phi(Z)/2}. \quad (6.10)$$

Note that the Z dependence appears solely in the phase ϕ and the anti-phase-locked quadrature has been assumed to be of $O(\epsilon)$. These assumptions make use of the results found in Chapter 3 in order to simplify the averaging procedure.

Upon expanding the quadratures in powers of ϵ^2 , i.e.,

$$A = A^0 + \epsilon^2 A^2 + \dots \quad (6.11a)$$

$$B = B^0 + \dots, \quad (6.11b)$$

and collecting terms of equal order of magnitude, the following three recursively related equations are found which govern the behavior of the pulse evolution

$$\frac{\partial A^0}{\partial \zeta} + (\Gamma - h(\zeta) - f(\zeta)) A^0 = 0 \quad (6.12a)$$

$$\frac{\partial B^0}{\partial \zeta} + (\Gamma - h(\zeta) + f(\zeta)) B^0 = \kappa L_- A^0 \quad (6.12b)$$

$$\frac{\partial A^2}{\partial \zeta} + (\Gamma - h(\zeta) - f(\zeta)) A^2 = -\frac{\partial A^0}{\partial \xi} + \frac{\tilde{\alpha}}{l_i} - \kappa L_- B^0. \quad (6.12c)$$

Here $L_- = (1/2 \partial^2 / \partial T^2 + (A^0)^2 / a_0 - 1/2)$ and the $\tilde{\alpha}/l_i$ of Eq. (6.12c) accounts for the overamplification which is of $O(\epsilon^2)$ at the first ($i=1$) and second ($i=2$) amplifier. Apart from the modification in the overamplification terms, the analysis thus far is identical to that of Chapter 3. Differences will arise, however, due to the averaging which occurs over a cycle of two amplifiers.

As mentioned earlier, the aim is to average over the amplifiers in such a way as to preserve a common average a_0 . This can be readily done by considering the system depicted in Fig. 6.2. The condition of a common average implies the following relation

$$\frac{e^{-\Gamma l_1}}{\Gamma l_1} \sinh \Gamma l_1 = e^{2(\alpha_1 - \Gamma l_1)} \frac{e^{-\Gamma l_2}}{\Gamma l_2} \sinh \Gamma l_2 = a_0, \quad (6.13)$$

where the factor $\exp(2(\alpha_1 - \Gamma l_1))$ arises as a consequence of the analysis which is carried out over the commensurate averages. In this case, the loss and gain are now balanced after two amplifiers. Moreover, the overamplification experienced at each amplifier is identical, i.e., $\tilde{\alpha}_1 = \tilde{\alpha}_2 = \tilde{\alpha}$.

Equations (6.12a-c) can be solved in progressive order to determine the effective evolution. Therefore, consider first the leading order problem given by Eq. (6.12a). Between amplifiers, the solution simply is exponentially attenuated just as in the previous analysis of Chapter 3. However, the appropriate jump conditions must now be imposed. Recall that the quadrature decomposition gives convenient jump conditions for both the phase-locked and anti-phase-locked quadratures. Therefore, the following hold

$$\text{amplifier 1: } A_+^0 = A_-^0 e^{\alpha_1} \quad (6.14a)$$

$$\text{amplifier 2: } A_+^0 = A_-^0 e^{\alpha_2}, \quad (6.14b)$$

and

$$\text{amplifier 1: } B_+^0 = B_-^0 e^{-\alpha_1} \quad (6.15a)$$

$$\text{amplifier 2: } B_+^0 = B_-^0 e^{-\alpha_2}. \quad (6.15b)$$

Upon using Eqs. (6.14a-b) with the leading order solution, it is found that $A^0 = R(\xi, T) \exp(-\Gamma \zeta)$ up to the first amplifier and $A^0 = R(\xi, T) \exp([\alpha_1 - \Gamma l_1] - \Gamma \zeta)$ between the first and second amplifiers. As was mentioned earlier in regards to the common average assumption, the factor of $\exp(2(\alpha_1 - \Gamma l_1))$ in the leading order solution between the first and second amplifier is crucial in the multiple scale averaging which is to be carried out. In addition, it is found that

$$\alpha_1 + \alpha_2 = \Gamma(l_1 + l_2) + O(\epsilon^2), \quad (6.16)$$

where again, it has been assumed that there exists an $O(\epsilon^2)$ correction to the exact balance of loss and gain in order to account for over or under-amplification. Recall that a minimum amount of overamplification was necessary to support stable pulse propagation due to the ‘loss’ incurred from the anti-phase-locked quadrature.

Many of the details considered thus far are similar to those of Chapter 3. To avoid needless repetition, only the highlights and results of the averaging will be considered in the remainder of this section. Certainly, the analysis will be more complicated as the averaging must be carried out over the two amplifiers. However, the analysis is simply as follows: the leading order behavior is investigated followed by the correction term in the anti-phase-locked quadrature and finishing with the appropriate solvability condition for Eq. (6.12c).

Proceeding then to the next order, Eq. (6.12b) gives the behavior of the anti-phase-locked quadrature. As in Chapter 3, upon applying the proper jump conditions for the anti-phase-locked quadrature, Eqs. (6.15), one can readily solve for B^0 over the two amplifier cycle. This is necessary in order to determine the appropriate solvability condition associated with the forcing in Eq. (6.12c). In particular, upon using the leading order behavior of the anti-phase-locked quadrature in Eq. (6.12c), it can be found after a bit of work and liberal use of Eq. (6.16) that the slow evolution of the envelope $U(\xi, T)$ evolves according to

$$\frac{\partial U}{\partial \xi} + \frac{1}{4} \left(\frac{\partial^2}{\partial \tau^2} - 1 \right)^2 U - \Delta\alpha U - U^3 + U^5 + 3\sigma U \left(\frac{\partial U}{\partial \tau} \right)^2 + (1+\sigma) U^2 \frac{\partial^2 U}{\partial \tau^2} = 0, \quad (6.17)$$

where

$$\Delta\alpha = \frac{4\tilde{\alpha} \sinh(\alpha_1 + \alpha_2)}{\kappa^2 [(l_1^2 + l_2^2) \cosh(\alpha_1 + \alpha_2) + 2l_1 l_2 \cosh(\alpha_1 - \alpha_2)]} \quad (6.18a)$$

$$\sigma = 1 + \sinh(\alpha_1 + \alpha_2) \frac{[l_1^2 \coth \Gamma l_1 - l_1/\Gamma + l_2^2 \coth \Gamma l_2 - l_2/\Gamma]}{(l_1^2 + l_2^2) \cosh(\alpha_1 + \alpha_2) + 2l_1 l_2 \cosh(\alpha_1 - \alpha_2)} \quad (6.18b)$$

and the long length scale ξ has been rescaled as follows

$$\bar{\xi} = \frac{\kappa^2 [(l_1^2 + l_2^2) \cosh(\alpha_1 + \alpha_2) + 2l_1 l_2 \cosh(\alpha_1 - \alpha_2)]}{2(l_1 + l_2) \sinh(\alpha_1 + \alpha_2)} \xi. \quad (6.19)$$

Equation (6.17) once again describes the average evolution of the soliton-like pulse on the familiar long length scale $\bar{\xi}$. This result is similar to the evolution of Eq. (3.28) derived for a single amplifier spacing with the exception of the coefficients of the nonlinear derivative terms, the overamplification parameter and the rescaling of ξ . In particular, the coefficients of the cubic and quintic terms again simultaneously scale

out. This fact can clearly be understood from the assumption of a common average for the two-amplifier spacing case which was carried out in the above analysis (see Fig. 6.2). Recall that the leading order solution is $A^0 = R \exp(-\Gamma\zeta)$ up to the first amplifier and $A^0 = R \exp(\alpha_1 - \Gamma l_1 - \Gamma\zeta)$ between the first and second amplifier. These solutions force the leading order solution of the anti-phase-locked quadrature which in turn force the higher order correction to the phase-locked quadrature. In the previous averaging of Chapter 3, this gave rise to the fourth-order structure. This result also holds here. However, the factor of $\exp(\alpha_1 - \Gamma l_1)$ is now crucial in the solvability conditions between the first and second amplifiers. Specifically, solvability of the higher order terms with this factor permits the simultaneous scaling of the cubic and quintic coefficients. This analysis strongly suggests the possibility of averaging over N distinct amplifier spacings in order to derive the same type of equation as that given in Eq. (6.17).

In the limit when $\Gamma l_1 = \Gamma l_2$, Eq. (6.17) reduces to Eq. (3.28). Qualitatively, the behavior will be similar to that discussed in Chapter 4. In particular, note that when the parameters $\Gamma l_1, \Gamma l_2$ and $\Delta\alpha$ are much less than unity, the leading order behavior of Eq. (6.17) reduces to Eq. (4.2) for which stable hyperbolic secant pulse solutions were shown to exist in Section 4.2. Further, in performing a bifurcation analysis from the trivial solution, Eq. (6.17) gives rise to a subcritical bifurcation from $(U, \Delta\alpha) = (0, 1/4)$. This is similar to the analysis carried out in Section 5.2 for the single, periodic amplifier spacing.

Just as in the previous chapters, the dynamics and stability of propagating soliton-like pulse solutions for arbitrary parameter values are left to be investigated through numerical simulations. These numerical simulations include the full computations of the NLS with the two distinct PSA spacings, numerical simulations of the averaged equation, and computations of the bifurcation curves via AUTO. The results of these computations will be presented in what follows.

The parameter regime considered first corresponds to amplifier spacings of 80 km and 100 km respectively. These spacings are chosen primarily to depict the qualitative and quantitative effects upon the generated sideband frequencies responsible for the background radiation field. Certainly a wide range of amplifier spacings

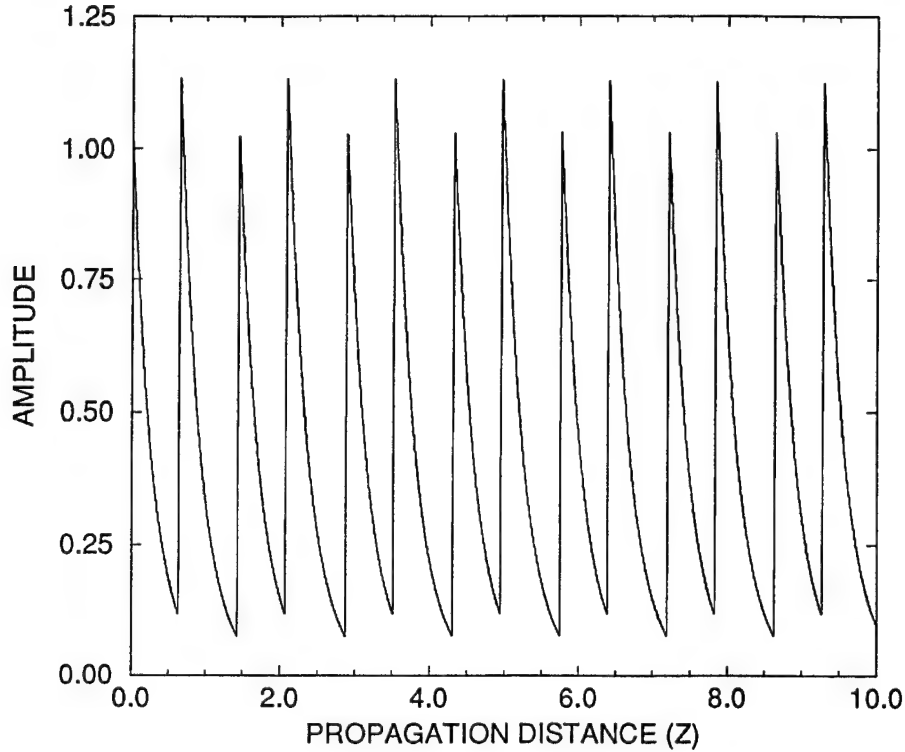


Figure 6.3: Depiction of the phase-locked quadrature dynamics for the two amplifier case. Note the periodic structure associated with the two amplifier spacing case.

may be considered, but for the present, the focus will be upon these characteristic lengths. In all the results that follow, the overamplification will remain fixed at $\Delta\alpha = 0.1$. With these parameters in mind, the midpoint values of the phase-locked quadrature A is plotted in Fig. 6.3. Note the periodic structure of this quadrature over the two distinct amplifier lengths.

Figure 6.4 represents the pulse propagation over 9,000 km in the Fourier domain for the full NLS with PSAs. Note the pulse amplitude is plotted after a two amplifier cycle in order to show more clearly the stability properties of a propagating pulse. Further, this avoids depicting the large amplitude changes which occur from one amplifier to the next due to the variable spacing of the amplifiers and the preservation of commensurate averages. Although Fig. 6.4 shows the stable evolution of

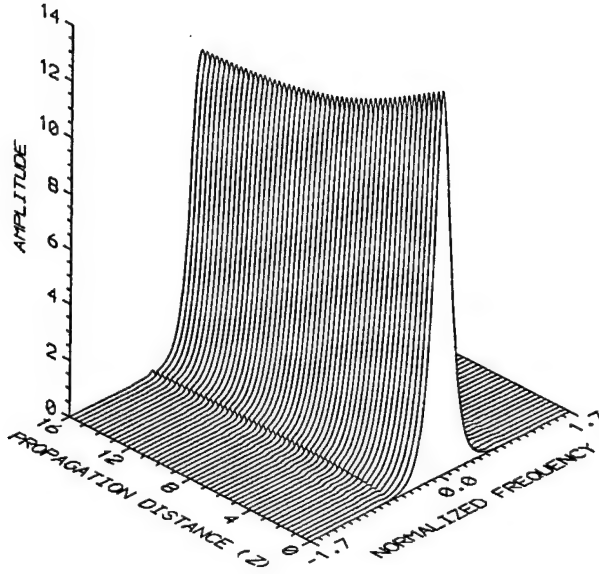


Figure 6.4: Pulse evolution in the Fourier domain over 9,000 km for the case when two distinct amplifier spacings are considered, namely 80 km and 100 km. The alternating amplifier spacings help reduce the sideband generation, i.e., compare this with the spectral evolution given by Fig. 4.6 in Chapter 4.

a propagating pulse over a fairly short distance, longer distances may be considered and can be shown to behave in a similar fashion. In fact, the pulse evolution is quite robust to the changes in the amplifier spacing. In Fig. 6.5, the averaged evolution of the two amplifier spacing case is considered and shown to decay exponentially onto the stable steady-state. This is just as before for the single, periodic spacing case. Further, it agrees quite well with the numerical results of the full NLS with PSAs.

Part of the aim of this section was to understand how the multiple amplifier spacing would change the dynamics of the pulse propagation and its associated dispersive radiation field. With this in mind, the spectrum of the two amplifier spacing case is compared with that of the single amplifier spacing case of previous chapters. Figure 6.6a represents the spectral composition after 18,000 km of a single amplifier spacing of 90 km. This is compared with Fig. 6.6b in which the alternating amplifier spacings of 80 km and 100 km are considered over 18,000 km. Note that the sideband frequencies are less pronounced for the two amplifier case. This can be further

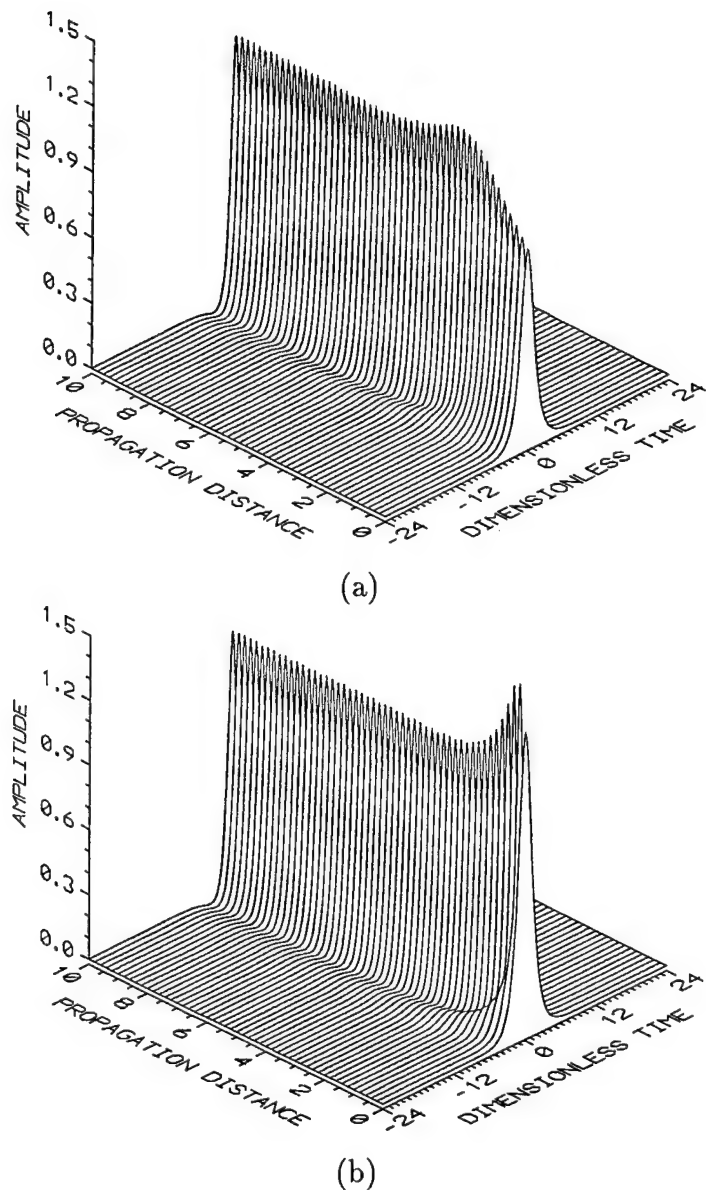


Figure 6.5: Numerical simulations of the averaged equation for two distinct amplifier spacings. As with the previous results of Chapter 4, note that the pulse asymptotically approaches the final steady-state as it propagates in $\bar{\xi}$. In (a) and (b) the initial conditions used were $U(0, \tau) = 0.9 \operatorname{sech} \tau$ and $U(0, \tau) = 1.4 \operatorname{sech} \tau$ respectively. Further, in both cases $\Delta\alpha = 0.1$, and the two amplifier lengths considered were 80 km and 100 km.

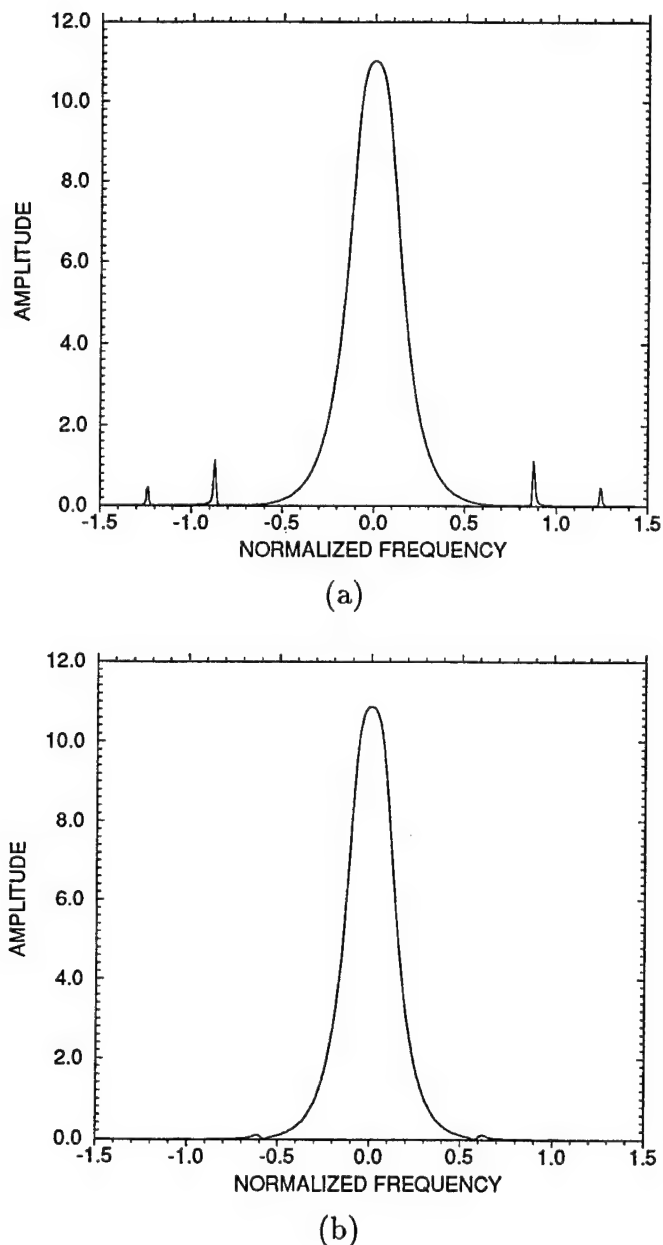


Figure 6.6: Spectral composition of a pulse after 18,000 km for a single amplifier spacing of 90 km (a) and the two amplifier spacing case with 80 km and 100 km (b). Note that the sharp sideband frequencies in (a) are reduced through the alternating spacings of (b).

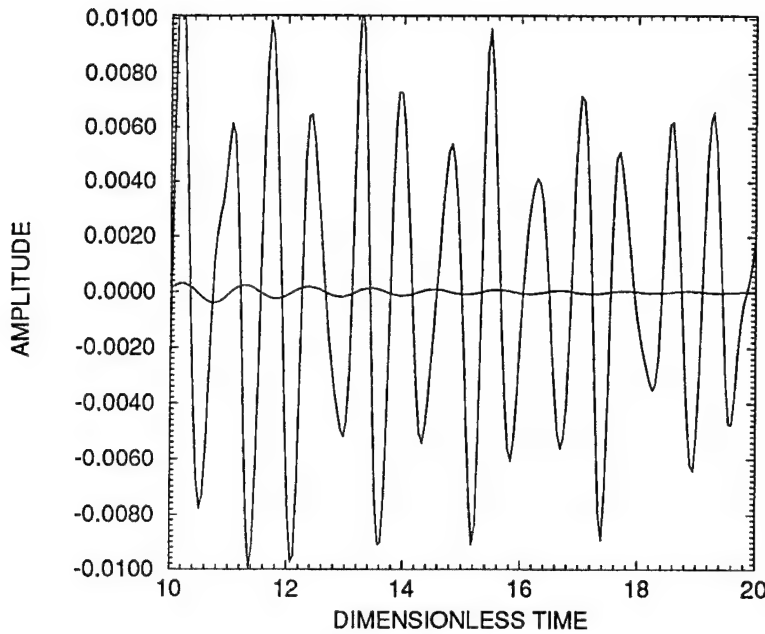


Figure 6.7: Comparison of the dispersive radiation field generated over 18,000 km using a single amplifier spacing of 90 km (large oscillations) versus the two amplifier spacing case for 80 km and 100 km (smaller oscillations). Note that the two amplifier case attenuates the radiation by nearly an order of magnitude.

demonstrated by comparing the dispersive radiation fields associated with each case. Fig 6.7 depicts the attenuation of the dispersive radiation field by nearly an order of magnitude when the two amplifiers are used in place of a single periodic amplifier. Once again, this phenomena can be understood in terms of the frequency windows which are transparent to the sideband frequencies. In particular, upon recalling the analysis carried out in Section 6.2, the effective eigenvalues can again be found for the two amplifier case. In this case however, the shift in the windows from one amplifier to the next will cause the sideband frequencies to experience a gain of less than unity. Therefore, the dispersive radiation is slowly attenuated.

As was mentioned earlier, AUTO can once again be used on Eq. (6.17) to detect and track steady-state branch solutions of the averaged equation. In particular,

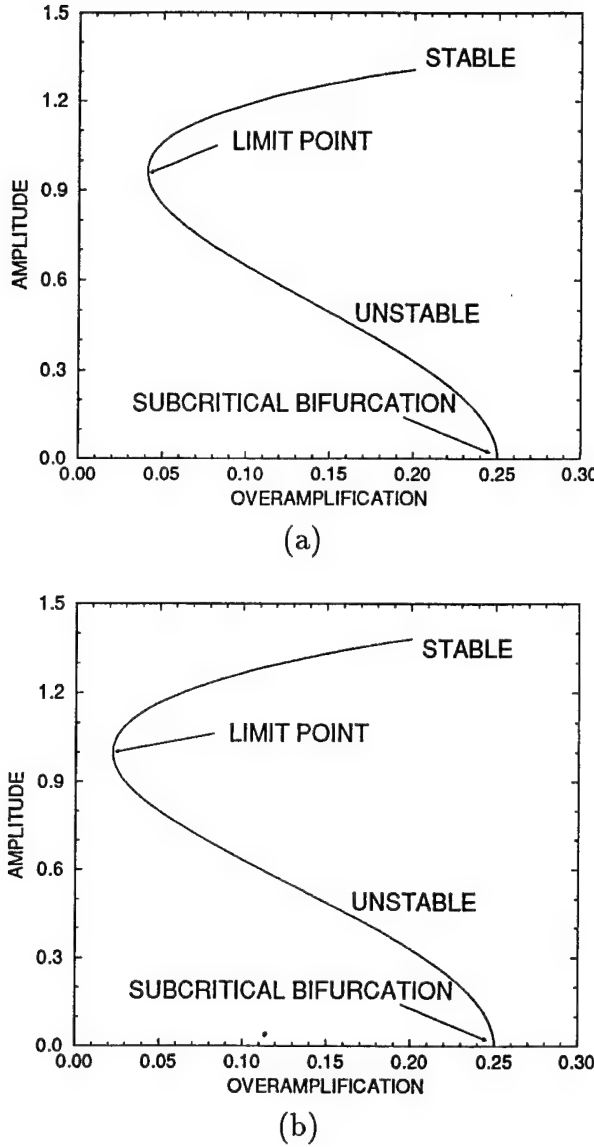


Figure 6.8: Bifurcation diagrams for the averaged evolution equation with two distinct amplifier spacings. In particular, (a) represents the bifurcation diagram when the amplifier spacings of 80 km and 100 km are used, i.e $\Gamma l_1 \sim 2.21$ and $\Gamma l_2 \sim 2.76$ respectively. In (b), the amplifier spacings of 36 km and 72 km (corresponding to $\Gamma l_1 = 1$ and $\Gamma l_2 = 2$) are considered. Note that these bifurcation diagrams are similar to those found in Chapter 5 and suggest the existence of a wide range of parameters which support stable pulse propagation.

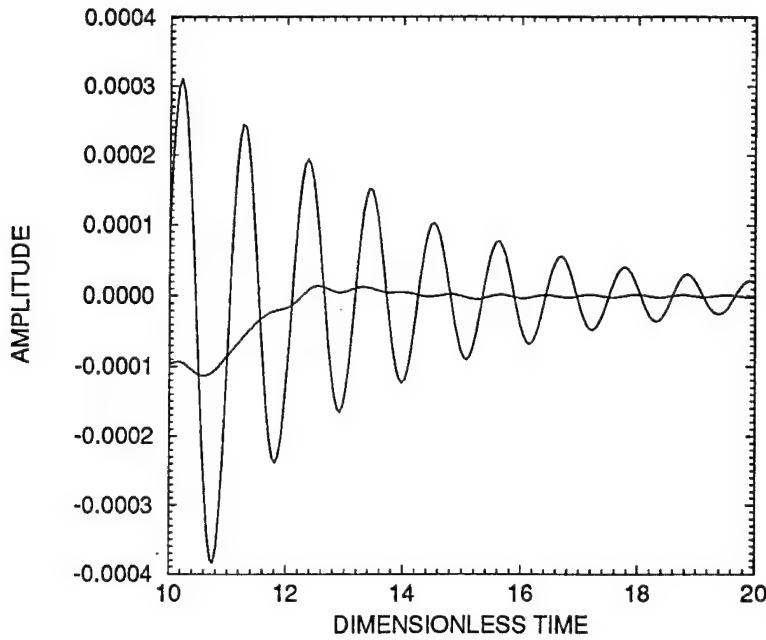


Figure 6.9: Comparison of the dispersive radiation field generated over 18,000 km using the two amplifier spacings of 70 - 110 km (smaller oscillations) and 80 - 100 km (larger oscillations) respectively. In this case the 70 - 110 km spacing is significantly smaller than the 80 - 100 km case which was nearly an order of magnitude smaller than its single amplifier counterpart.

Figs 6.8a and 6.8b depict two characteristic bifurcation curves for fixed values of the parameters Γl_1 and Γl_2 . Note the resemblance of these curves to those previously explored in Chapter 5. In fact, the qualitative structure of parameter space for the averaged two amplifier evolution is essentially identical to that of the single amplifier evolution as expected. Therefore, it can be understood that the averaged evolution will give rise to a wide range of parameters for which the two amplifier spacing case supports stable, soliton-like pulse propagation, i.e., the parameter space for which stable solutions exist can once again be represented qualitatively by Fig. 5.8.

As a final note, the case for which the amplifier spacings correspond to 70 km and 110 km is considered. Many of the qualitative features discussed in the

preceding paragraphs hold for this case. However, since the amplifier spacings are not close, it is expected that the dispersive radiation would be attenuated even more due to the large separation of the windows of transparencies. Figure 6.9 depicts the background radiation field for the case of the two amplifier spacings of 80 km and 100 km and the two amplifier spacings, 70 km and 110 km. Note that the 70-110 km case produces a much smaller radiation field than that of the single amplifier case. Further, the radiation field is also smaller than that produced with amplifier spacings of 80 km and 100 km which has the same average amplifier spacing. The next section will consider the case for which there are no distinct amplifier spacings, but rather, some distribution of the amplifier spacings about some mean.

6.4 Random Amplifier Spacing

In the last section, the averaging over the two distinct amplifier lengths led to the derivation of the averaged Eq. (6.17) which was similar to that obtained in the case of a single amplifier spacing. This was then shown to support stable pulse propagation much as before. In this section, randomly spaced amplifiers are considered. This essentially corresponds to the case in which the period of the amplifier spacings is infinite. The results of the last section suggest that stable pulse solutions might exist. However, the work done in obtaining the averaged evolution of the last section also suggests that the standard averaging approach becomes analytically intractable and one must resort to numerical computations.

Unlike the previous section, which assumed the averaging took place in such a way as to preserve a common average, this case assumes the average energy over a gain-loss segment to change from one amplifier to the next as it propagates. Therefore, the case for which the loss is balanced to $O(\epsilon^2)$ at each consecutive amplifier is considered. It will be assumed in the following numerical computations that the overamplification is of a fixed value, i.e., $\Delta\alpha = 0.1$. Future work will consider allowing the overamplification also to vary randomly from amplifier to amplifier. The aim will be to investigate the robustness of the pulse propagation when randomly spaced amplifiers are used and to further understand the generation of the sideband

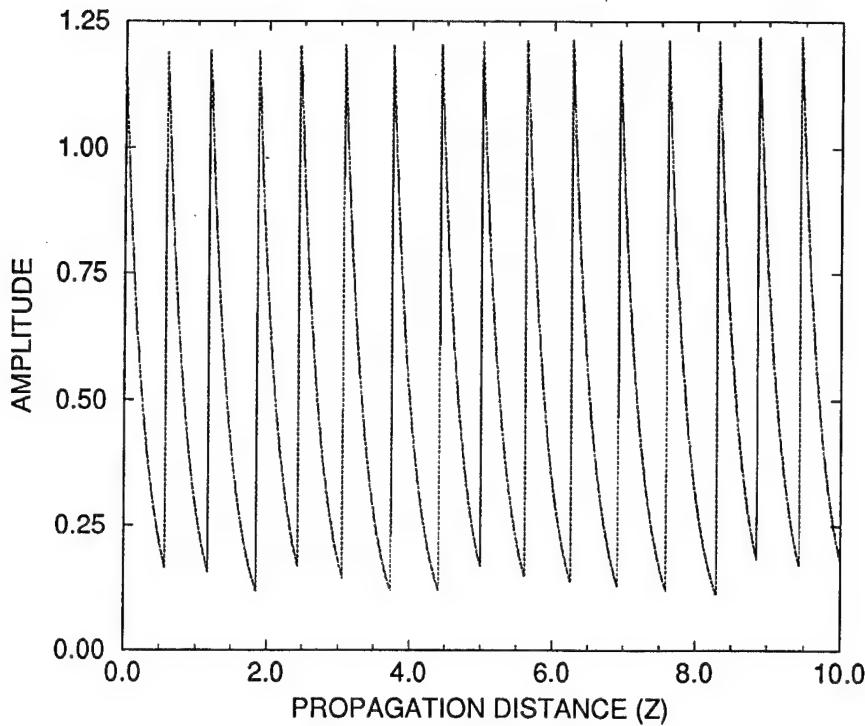


Figure 6.10: Behavior of the phase-locked quadrature amplitude which propagates through a chain of randomly spaced phase-sensitive amplifiers

frequencies. In what follows, a few examples will be carried out which are indicative of the qualitative and quantitative features of the random spacings.

To begin, Fig. 6.10 depicts the behavior of the maximum amplitude of the phase-locked quadrature. Note the random pattern of loss and gain. In this calculation, it has been assumed that the amplifiers are uniformly distributed between 70 km and 90 km. As was noted previously, one can further analyze the background radiation field generated from the random amplifier spacings. In particular, the spectral evolution of three distinct amplification methods are compared in Fig. 6.11; the single amplifier spacing of 80 km, a two amplifier spacing of 70 km and 90 km, and the uniformly distributed amplifier spacing between 70 km and 90 km. Each of these cases has a mean amplifier spacing of 80 km. The corresponding radiation fields are

depicted in Fig. 6.12. Note that both the two amplifier spacing case and the random amplifier spacing case reduce the radiation by a factor of ten from the single periodic spacing case. This suggest that randomly spaced amplifiers can be used to further attenuate linear dispersive radiation.

One might imagine that if the uniform distribution of the amplifiers was over a larger interval, the background radiation field might be further attenuated. Figs. 6.13 depict the spectral components of the pulse evolution for the uniform distribution of the amplifiers about 80 km. In particular the range of amplifier spacings are between 60-100 km, 70-90 km and 75-85 km. Note that as expected, the sideband spectral components of the 60-100 km case is much smaller than that of the 70-90 km or 75-85 km cases. The corresponding dispersive radiation fields are depicted in Figs. 6.14. This further suggests that the wider the uniform distribution, the less background radiation field will be allowed to propagate through the fiber-PSA system.

Although this section is solely numerical in nature, it may be possible to make use of stochastic and perturbation methods to derive some kind of averaged evolution. This approach will be considered in the near future and should provide further insight into the structure and stability of the pulse propagation. Regardless, the use of the PSAs in conjunction with the optical fibers seems to suggest remarkable stability properties of the averaged evolution.

6.5 Summary

The purpose of this chapter was to come to some kind of understanding of the effects of the periodic amplifier spacing upon the generated background radiation field. Further, the more physically realistic model of variable amplifier spacing needed to be considered along with its ability to support stable pulse propagation. These two phenomena were shown to be closely related. In fact, the generated background radiation field was a product of the gain-loss forcing and depended strongly upon the amplifier spacing. Section 6.2 explicitly found the relation between the sideband frequencies and the amplifier spacing and demonstrated that certain frequency windows existed for which the radiation experiences unity gain. Therefore, the periodic

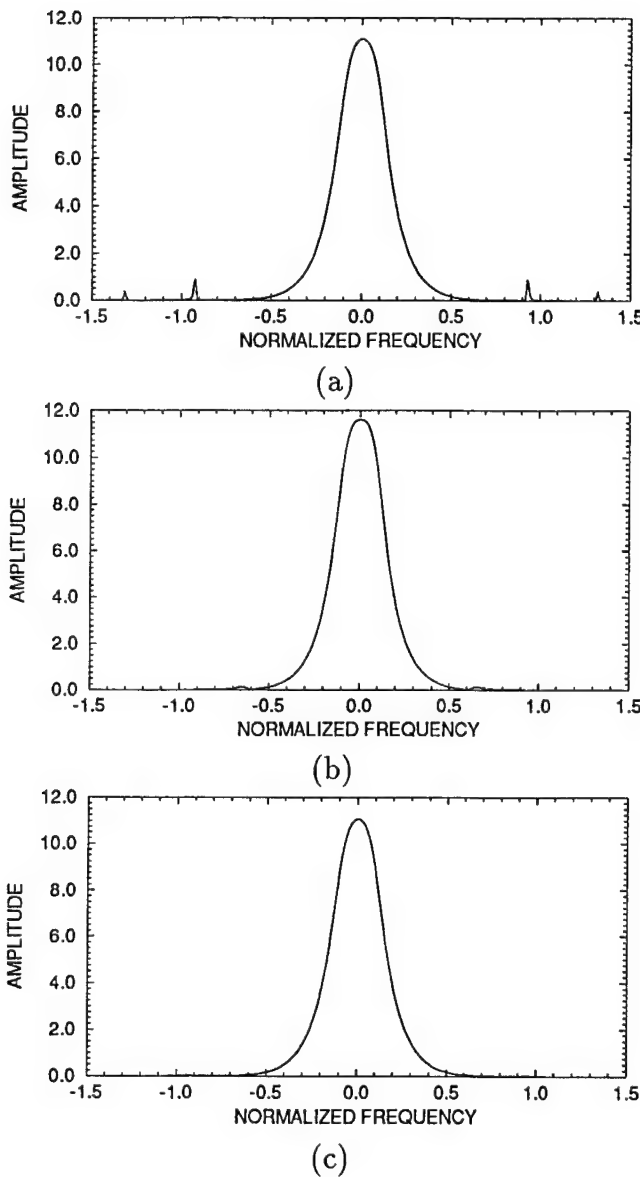


Figure 6.11: Comparison of the spectral components after 200 amplifiers of three distinct amplification schemes which utilize PSAs. In (a), periodically-spaced PSAs are considered with an amplifier spacing of 80 km. An alternating spacing of 70 km and 90 km is considered in (b) while uniformly distributed amplifiers between 70 and 90 km are considered in (c).

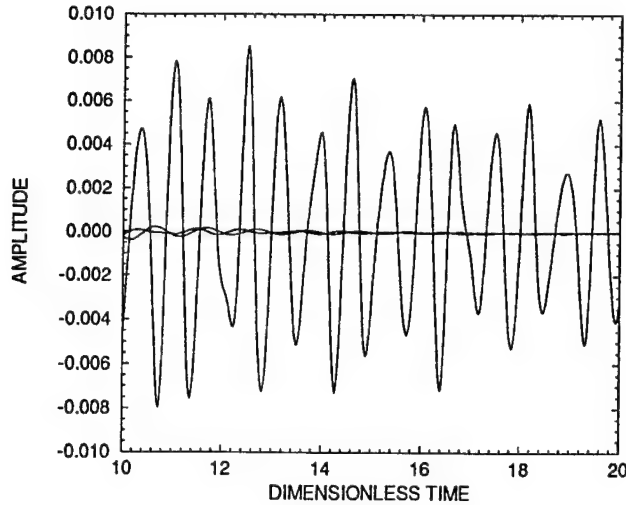


Figure 6.12: Dispersive radiation field generated from the sideband frequencies of the three amplification schemes considered in the previous figure. The two smaller dispersive fields correspond to the random and two amplifier spacings. The important thing to note is that the two amplifier spacing and the random spacing greatly reduce the amount of background radiation generated.

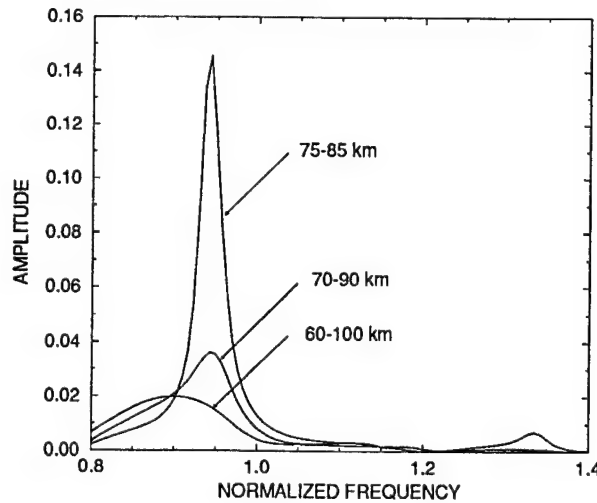


Figure 6.13: Comparison of the the primary sideband frequency for randomly spaced amplifiers for differing values of the distribution. In particular, the uniform distributions for amplifiers between 60-100 km, 70-90 km and 75-85 km are considered.

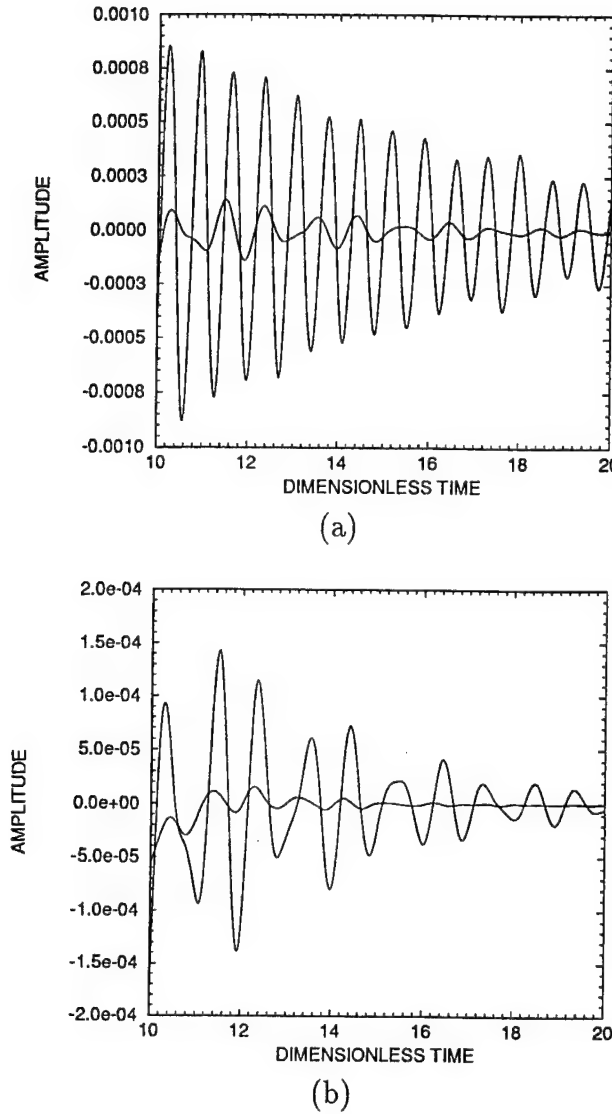


Figure 6.14: Investigation of the background radiation fields generated from the side-band frequencies of the previous figure. In (a), a comparison is made between the 75-85 km distribution (larger oscillations) and the 70-90 km distribution (smaller oscillations). This is followed in (b) by a comparison of the dispersive fields for the 70-90 km distribution (larger oscillations) and the 60-100 km distribution (smaller oscillations). Note that the dispersive radiation fields are approximately of $O(10^{-4})$, $O(10^{-5})$ and $O(10^{-6})$ for the uniform distributions between 75-85 km, 70-90 km and 60-100 km respectively.

spacing of the amplifiers produced sideband frequencies which experienced unity gain along a fiber-PSA chain. Upon considering variably spaced amplifiers, it was found that the window of transparencies were shifted from amplifier to amplifier causing the attenuation of the background radiation field.

In particular, Section 6.3 was concerned with the analytic theory of a fiber-PSA system which had two alternating and distinct amplifier spacings. Within this physical framework, it was still possible to average over the loss and gain across the two amplifier period to obtain an averaged evolution over an extended length scale. Numerical simulations of this system showed that the sideband frequency and its corresponding background radiation field was attenuated by an order of magnitude over its single, periodic amplifier spacing counterpart. This was the first evidence which suggested the possibility of using the variable amplifier spacing for reducing the dispersive field. Further, the analysis of Section 6.3 strongly suggests that one can average over N amplifiers in order to derive the same type of equation as Eq. (3.28) and Eq. (6.17) with the only differences arising in the coefficients of the nonlinear terms and the rescaling of the long length scale $\bar{\xi}$ and overamplification $\Delta\alpha$.

In Section 6.4, the idea of variable amplifier spacing was carried one step further. Specifically, the amplifier spacing was allowed to vary uniformly over a range of lengths. This random spacing of the amplifiers significantly reduced the background radiation field generated from the gain-loss forcing. Moreover, the random spacing of the amplifiers correspond to a physically realizable system for which the spacing of the amplifiers will depend on factors which are associated with the physical environment of the fiber-PSA line.

References

- [1] R. W. Boyd, *Nonlinear Optics*, (Academic Press, San Diego, 1992).
- [2] G. P. Agrawal, *Fiber-Optic Communication Systems*, (John Wiley & Sons, New York, 1992).
- [3] G. P. Agrawal, *Nonlinear Fiber Optics*, (Academic Press, New York, 1989).
- [4] A. Hasegawa, *Optical Solitons in Fibers*, 2nd Ed., (Springer, Berlin, 1990).
- [5] N. J. Zabusky and M. D. Kruskal, “Interactions of ‘solitons’ in a collisionless plasma and the recurrence of initial states”, Phys. Rev. Lett. **15**, 240-243 (1965)
- [6] C. S. Gardner, J. M. Greene, M. D. Kruskal, and R. M. Miura, “Method for solving the Korteweg-deVries equation”, Phys. Rev. Lett. **19**, 1095-1097 (1967)
- [7] A. Hasegawa and F. D. Tappert, “Transmission of stationary nonlinear optical pulses in dispersive dielectric fibers. I. Anomalous dispersion”, Appl. Phys. Lett. **23**, 142–144 (1973).
- [8] L. F. Mollenauer, R. H. Stolen and J. P. Gordon, “Experimental observation of picosecond pulse narrowing and solitons in optical fibers”, Phys. Rev. Lett. **45**, 1095 (1980)
- [9] V. E. Zakharov and A. B. Shabat, “Exact theory of two-dimensional self-focusing and one-dimensional self-modulation of waves in nonlinear media”, Sov. Phys. JETP **34**, 62-69 (1972)
- [10] M. J. Ablowitz, D. J. Kaup, A. C. Newell and H. Segur, “The inverse scattering transform - Fourier analysis for nonlinear problems”, Stud. Appl. Math. **53**, 249-315 (1974)

- [11] M. J. Ablowitz and H. Segur, *Solitons and the Inverse Scattering Transform*, (SIAM, Philadelphia, 1981); P. G. Drazin and R. S. Johnson, *Solitons: an introduction*, (Cambridge University Press, Cambridge, 1989)
- [12] D. J. Kaup, "A perturbation theory for the inverse scattering transforms", SIAM J. Appl. Math. **31**, 121-123 (1976)
- [13] J. P. Keener and D. W. McLaughlin, "Solitons under perturbations", Phys. Rev. A **16**, 777-790 (1977)
- [14] Y. Kodama and M. J. Ablowitz, "Perturbations of Solitons and Solitary Waves", Stud. Appl. Math. **64**, 225-245 (1981)
- [15] V. I. Karpman and V. V. Solovev, "A perturbational approach to the two-soliton systems", Physica **3D**, 475-502 (1981)
- [16] J. N. Elgin, "Perturbations of Optical Solitons", Phys. Rev. A **47**, 4331-4341 (1993)
- [17] N. S. Bergano *et al.*, "Bit error-rate measurements of 14,000 km 5 Gb/sec fiber-amplifier transmission system using circulation loop", Electron. Lett. **27**, 1889-1890 (1991).
- [18] A. Hasegawa and Y. Kodama, "Guiding-center soliton in optical fibers", Opt. Lett. **15**, 1443-1445 (1990); "Guiding-center soliton", Phys. Rev. Lett. **66**, 161-164 (1991). Y. Kodama and A. Hasegawa, "Theoretical foundations of optical-soliton concept in fibers", in *Progress in Optics XXX*, E. Wolf, ed., (Elsevier, Amsterdam, 1992).
- [19] L. F. Mollenauer, S. G. Evangelides and H. A. Haus, "Long-distance soliton propagation using lumped amplifiers and dispersion shifted fiber", J. Lightwave Tech. **9**, 194-197 (1991).
- [20] E. M. Dianov, A. V. Luchnikov, A. N. Pilipetskii, and A. N. Starodumov, "Electrostriction mechanism of soliton interaction in optical fibers", Opt. Lett. **15**,

- 314–316, (1990); “Long-range interaction of solitons in ultra-long communication systems”, Soviet Lightwave Comm. **1**, 235-246 (1991).
- [21] J. P. Gordon and H. A. Haus, “Random walk of coherently amplified solitons in optical fiber transmission”, Opt. Lett. **11**, 665–667 (1986).
 - [22] A. Mecozzi, J. D. Moores, H. A. Haus and Y. Lai, “Soliton transmission control”, Opt. Lett. **16**, 1841–1843 (1991); Y. Kodama and A. Hasegawa, “Generation of asymptotically stable optical solitons and suppression of the Gordon-Haus effect”, Opt. Lett. **17**, 31–33 (1992); L. F. Mollenauer, J. P. Gordon and S. G. Evangelides, “The sliding-frequency guiding filter: an improved form of soliton jitter control”, Opt. Lett. **17**, 1575–1577 (1992).
 - [23] H. Yuen, “Reduction of quantum fluctuation and suppression of the Gordon-Haus effect with phase-sensitive linear amplifiers”, Opt. Lett. **17**, 73–75 (1992).
 - [24] Sueng-Hee Lee, “Ultra-long distance optical communication using phase-sensitive linear amplifier chains”, Ph.D. Thesis, Northwestern University, December 1992.
 - [25] J. N. Kutz, W. L. Kath, R.-D. Li, and P. Kumar, “Long-distance pulse propagation in nonlinear optical fibers using periodically-spaced parametric amplifiers”, Opt. Lett. **18**, 802–804 (1993); J. N. Kutz, C. V. Hile, W. L. Kath, R.-D. Li, and P. Kumar, “Pulse propagation in nonlinear optical fiber lines that employ phase-sensitive parametric amplifiers”, J. Opt. Soc. Am. B, **11**, (1994).
 - [26] P. N. Butcher and D. Cotter, *The Elements of Nonlinear Optics*, (Cambridge University Press, Cambridge, 1990); Y. R. Shen *The principles of nonlinear optics*, (John Wiley & Sons, New York, 1984); A. C. Newell and J. V. Moloney, *Nonlinear Optics*, (Addison-Wesley, 1992)
 - [27] G. A. Bukauskas, V. I. Kabelka, A. S. Piskarskas, A. Yu. Stabinis, “Features of three-photon parametric interaction of ultrashort light packets in the nonlinear amplification regime”, Sov. J. Quant. Elec. **4**, 290-292 (1974)

- [28] R. Danelyus, G. Dikchyus, V. Kabelka, A. Piskarskas and A. Stabinis, "Parametric excitation of light in the picosecond range", Sov. J. Quant. Elec. **7**, 1360-1368 (1977)
- [29] V. G. Dmitriev, G. G. Gurzadyan and D. N. Nikogosyan, *Handbook of Nonlinear Optical Crystals*, (Springer-Verlag, New York, 1991)
- [30] D. J. Kaup, "A Method for Solving the Separable Initial-Value Problem of the Full Three-Dimensional Three-Wave Interaction", Stud. Appl. Math. **62**, 75-83 (1980)
- [31] M. Shirasaki and H. A. Haus, "Squeezing of pulses in a nonlinear interferometer", J. Opt. Soc. Am. B **7**, 30-34 (1990); M. E. Marhic and C.-H. Hsia, "Optical amplification in a nonlinear interferometer", Elec. Lett. **27**, 210 (1991)
- [32] R.-D. Li, P. Kumar and W. L. Kath, "Dispersion compensation with phase-sensitive amplifiers", J. of Lightwave Technology, **12** 541-549 (1994).
- [33] G. Bartolini, R.-D. Li, P. Kumar, W. Riha, and K. V. Reddy, "1.5 μm phase-sensitive amplifier for ultra-high speed communications", in *Optical Fiber Communication Conference*, Vol. 4 of 1994 OSA Technical Digest Series (Optical Society of America, Washington, D.C., 1994), pp. 202-203.
- [34] C. M. Bender and S. A. Orszag, *Advanced Mathematical Methods for Scientists and Engineers*, (McGraw-Hill, Inc. 1978), Chap. 11; J. Kevorkian and J. D. Cole, *Perturbation Methods in Applied Mathematics*, (Springer-Verlag, 1981), Chap. 3.
- [35] B. Friedman, *Principles and Techniques of Applied Mathematics*, (John Wiley & Sons, 1956).
- [36] M. Weinstein, "Modulational stability of ground states of nonlinear Schrödinger Equations", SIAM J. Math. Anal. **16**, 472-491 (1985).
- [37] A. Halanay and V. Rasvan, *Applications of Liapunov methods in Stability*, (Kluwer Academic Publishers, 1993); A. Halanay, *Differential Equations: Stability, Oscillations, Time Lags*, (Academic Press, 1966); N. Rouche, P. Habets

- and M. Laloy, *Stability Theory by Liapunov's Direct Method*, (Springer-Verlag, 1977).
- [38] T. Y. Hou, J. S. Lowengrub, and M. J. Shelley, "Removing the stiffness from interfacial flows with surface tension", submitted to *J. Comp. Phys.*, 1993.
 - [39] M. D. Feit and J. A. Fleck, "Light propagation in graded-index optical fibers", *Appl. Opt.* **17**, 3990–3998 (1978); P. E. Lagasse and R. Baets, "Application of propagating beam methods to electromagnetic and acoustic wave propagation problems: A review", *Radio Science* **22**, 1225–1233 (1987).
 - [40] T. R. Taha and M. J. Ablowitz, "Analytical and numerical aspects of certain nonlinear evolution equations. II. Numerical, nonlinear Schrödinger equation", *J. Comp. Phys.* **55**, 203–230 (1984).
 - [41] R.-D. Li, P. Kumar, W. L. Kath, J. N. Kutz, "Combating dispersion with parametric amplifiers", *IEEE Photonics Technology Letters* **5**, 669–672 (1993).
 - [42] J. P. Gordon, "Dispersive perturbations of solitons of the nonlinear Schrödinger equation", *J. Opt. Soc. Am. B* **9**, 91–97 (1992).
 - [43] H. Segur *et al.*, editors, *Asymptotics Beyond All Orders*, Plenum, New York, (1992).
 - [44] L. A. Segel, "Distant side-walls cause slow amplitude modulation of cellular convection", *J. Fluid Mech.* **38**, 203-224 (1969); A. C. Newell and J. A. Whitehead, "Finite bandwidth, finite amplitude convection", *J. Fluid Mech.* **38**, 279-303 (1969); M. C. Cross and P. C. Hohenberg, "Pattern formation outside of equilibrium", *Rev. Mod. Phys.* **65**, 851-1112 (1993)
 - [45] E. Doedel, *AUTO: Software for Continuation and Bifurcation Problems in Ordinary Differential Equations*; M. J. Friedman and E. Doedel, "Numerical computation and continuation of invariant manifolds connecting fixed points", *SIAM J. Numer. Anal.* **28**, 789–808 (1991)

thought of as a single ‘signal’ field. In the analysis that follows, the pump field has been assumed to be much larger in amplitude and much longer in duration than either the signal or idler fields. In particular, the pump can be assumed to be undepleted by the nonlinear interaction and can be then taken to be essentially constant. This will be made more clear from the characteristic scalings which will be introduced shortly.

Attention is now given to simplifications and approximations which are consistent with retaining the leading order behavior of the three wave interaction. In most cases of interest, i.e., materials for which parametric amplification is carried out, the quadratic nonlinearity dominates the cubic nonlinearity which allows the cubic term to be neglected in the analysis, i.e., $\chi^{(2)} \ll \chi^{(3)}$. Further, over the length scale of interest, the nonlinear medium can be considered essentially lossless. These assumptions, along with the assumption that the phase-mismatch Δk is identically zero, i.e., perfect phase-matching is achieved, simplifies significantly the equations governing the three wave interaction.

In order to clarify these statements made concerning the pump, signal and idler fields, it becomes necessary to nondimensionalize the Eqs. (19) on the characteristic scales of the problem. Therefore, define the following set of nondimensional variables

$$Z = \zeta/\zeta_0 \quad (21a)$$

$$\xi = \eta/\eta_0 \quad (21b)$$

$$S = \mathcal{E}_1/\mathcal{E}_s \quad (21c)$$

$$I = \mathcal{E}_2/\mathcal{E}_s \quad (21d)$$

$$P = \mathcal{E}_3/\mathcal{E}_p, \quad (21e)$$

where ζ_0 corresponds to the characteristic length of the nonlinear medium, η_0 defines a characteristic pulse width of the signal field, and \mathcal{E}_s and \mathcal{E}_p define the characteristic amplitudes of the signal and pump fields respectively. Recall it has been assumed that $\Delta k = 0, \delta = 0$ and $\chi^{(3)} = 0$. Further, since the PSA is degenerate, $\omega_1 = \omega_2$ and the sum of the signal and idler fields becomes the effective ‘signal’ field. Eqs. (19) then reduce to the following

$$\begin{aligned} \frac{\partial S}{\partial Z} &= -i \left(\frac{\zeta_0 g_1}{\eta_0^2} \right) \frac{\partial^2 S}{\partial \xi^2} + i(\sigma_1 \chi^{(2)} \mathcal{E}_p \zeta_0) I^* P \\ \frac{\partial I}{\partial Z} &= -i \left(\frac{\zeta_0 g_2}{\eta_0^2} \right) \frac{\partial^2 I}{\partial \xi^2} + i(\sigma_2 \chi^{(2)} \mathcal{E}_p \zeta_0) S^* P - \left(\frac{\nu_{21} \zeta_0}{\eta_0} \right) \frac{\partial I}{\partial \xi} \\ \frac{\partial P}{\partial Z} &= -i \left(\frac{\zeta_0 g_3}{\eta_0^2} \right) \frac{\partial^2 P}{\partial \xi^2} + i \left(\frac{\sigma_3 \chi^{(2)} \mathcal{E}_s^2 \zeta_0}{\mathcal{E}_p} \right) S^2 - \left(\frac{\nu_{31} \zeta_0}{\eta_0} \right) \end{aligned}$$

where use has been made of Eqs. (21) and (20).

It is convenient to establish the appropriate orders of magnitude of the various terms of Eq. (22). In what follows, the nonlinear medium will be assumed to be a KTP crystal (KTiOPO_4 , Potassium Titanyl Phosphate)⁷. In particular, the following characteristic measures are considered

$$\zeta_0 \sim 5 \text{ mm} \quad (23a)$$

$$\eta_0 \sim 50 \text{ ps} \quad (23b)$$

$$\mathcal{E}_p/\mathcal{E}_s \sim 20 \quad (23c)$$

$$\chi^{(2)} = 2d^{(2)} \sim 6 \times 10^{-12} \text{ m/V} \quad (23d)$$

$$\mathcal{E}_p \sim 48 \times 10^6 \text{ V/m.} \quad (23e)$$

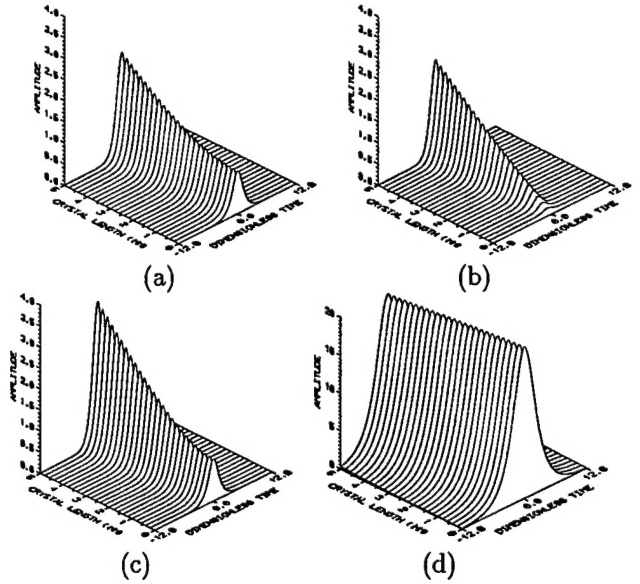


Fig. 2. Qualitative behavior of the signal, idler, and pump fields. In (a) and (b) the signal and idler fields are depicted. The initial signal field is a hyperbolic secant while the initial idler field was zero. In (c), the combined signal and idler fields are depicted. This represents the effective ‘signal’ field output of the PSAs. The pump field in (d) is shown to be essentially undepleted with a slight group-velocity drift.

The wavelength of interest, which corresponds to soliton based communications systems, is $\lambda = 1.55$ microns. Numerical simulations of the Eqs. (22) using Eqs. (23) are shown in Figs. 2. The initial signal and pump pulses are assumed to be hyperbolic secants while the idler field is initially zero. Note the amplification and gain associated with the signal and idler fields through a small section of KTP crystal. Moreover, note that the pump field remains largely unaffected through the interaction.